# The Asymmetry of the $^{12}C(\overrightarrow{\gamma},pn)$ reaction

Stefan Franczuk

Presented as a Thesis for the degree of Doctor of Philosophy

Department of Physics and Astronomy,

University of Glasgow,

1998.



ProQuest LLC.
789 East Eisenhower Parkway
P.O. Box 1346
Ann Arbor, MI 48106 – 1346

# Abstract

The work presented in this thesis describes the first experimental study of the $^{12}C(\vec{\gamma},pn)$ reaction using linearly polarised tagged photons in the energy range 150 MeV to 360 MeV. The experiment was carried out using the MAMI-B c.w. electron accelerator at the Institut für Kernphysik, Mainz, Germany.

Linearly polarised Bremsstrahlung photons were produced by a diamond radiator and are tagged by momentum analysing the recoiling electrons using the Glasgow tagging spectrometer. The tagger has an energy resolution of 2MeV and can tag photon fluxes of up to $\sim 10^8 s^{-1}$. The $^{12}C$ target was in the form of a 2mm thick graphite sheet, placed at an angle of 30° to the photon beam line. A plastic scintillator hodoscope PiP was used to detect the protons from the target, and covered polar angles from 51° to 129°, with a resolution of ~4.5° and azimuthal angles from -22.8° to +22.8°. The coincident neutrons were detected in 6 banks of plastic time-of-flight (TOF) scintillator detectors, each made up of 2 layers. These were positioned opposite PiP, covering polar angles from 10° to 175° with a resolution of ~2°, and azimuthal angles in the range 160° to 200°. The detector system has a missing energy resolution of ~7.5 MeV for allowing nucleon breakup from the (1p1p) shells and (1s1p) shells to be distinguished.

Direct knockout events were selected on the basis of angular correlation and missing energy. Photon asymmetries and parallel and perpendicular cross sections were measured in 12 photon energy bins, each of width 20 MeV. Within each bin asymmetries were measured for 3 missing energy regions, (20-40 MeV), (40-70 MeV) and (>70 MeV), corresponding to the ejection of nucleons from (1p1p), (1p1s) shells and multiparticle processes respectively.

Systematics of the asymmetries were studied by measuring those asymmetries as a function of recoil momentum for the 20-40 MeV and the 40-70 MeV missing

energy regions. Within the 20-40 MeV region photon asymmetries were also measured as a function of proton polar angle. Differential cross sections were also measured for both the parallel and perpendicular directions of polarisation, in the 20-40 MeV missing energy region. Comparisons have been made with results on lighter nuclei from previous experiments, which allow some clear trends to be identified. The data have been shown to be consistent with direct 2N knockout for missing energies up to 70 MeV. The data have also been compared to predictions of asymmetry from the theory developed by the Gent group, and good agreements have been found in the 20-40 MeV missing energy region, at photon energies above 200 MeV. Differences were found between data and theory in the 40-70 MeV missing energy region, and for the 20-40 MeV region below 200 MeV.

# Declaration

The data presented in this thesis were obtained by the Experimental Nuclear Physics group at the University of Glasgow in collaboration with colleagues from the Nuclear Physics groups at the Universities of Edinburgh, Tübingen and Mainz. The experiment was performed at the Institut für Kernphysik at the University of Mainz. I participated fully in the execution of the experiment. The analysis and interpretation of the experimental data is entirely my own work. This thesis was composed by myself.

**Stefan Franczuk**

# Acknowledgements

I would like to thank all the members of the Nuclear Physics Group at the University of Glasgow for all their help, advice and guidance over the last three and a half years. In particular I would like to thank Prof. Robert Owens who provided me with the opportunity to do this research. I hope he didn't mind too much putting up with a moaning thirtysomething and I thank him for his precise reading of this thesis. I would also like to thank my supervisor, Douglas MacGregor for pointing me in the right direction many times. I am also indebted to Cameron McGeorge for his patient advice, help and explanation on many numerous occasions. I would also like to thank John Annand and Ken Livingstone, without whom this experiment would never have proceeded, and equally I would also like to thank Ian Anthony and Andy Sibbald, without whose professional maintenance of the computer system, this experiment would never have been analysed.

As for my compatriates, I would like to say thanks to Dan Watts, Steve McAllister and Robin Watson, for there help, guidance and advise on many occasions, too numerous to mention. I am also indebted to my fellow analyser, Calum Powrie. I also take my hat of to him for his ability to manage a night shift on a belly full of beer and a kebab. As for my collaborators, I would like to thank Peter Grabmayr and Torsten Hehl for their technical support, and I am also indebted to Alex Natter for his help and for his valuable skiing lessons. I also take this opportunity to thank everyone else involved in this experiment.

On a personnel level, I will be forever thankful to my wife Annette, without whose support, belief and encouragement none of this would ever have been possible. I shall be eternally grateful. I would also like to say thanks to my children, Andrea and Christopher, just for being there. It is to my beloved family that I dedicate this work.

**The woods are lovely, dark and deep,**
**But I have promises to keep,**
**And miles to go before I sleep,**
**And miles to go before I sleep.**

Robert Frost.
'Stopping by woods on a snowy evening'.

# Contents

# List of Figures

# List of Tables

# Chapter 1

# Introduction

## 1.1 Introduction

The subject of this thesis is the study of the asymmetry of the $^{12}C(\overrightarrow{\gamma},pn)$ reaction, at photon energies around the Delta resonance region. In the general field of nuclear physics, polarisation variables and their phenomena have been found to be very helpful in differentiating between different nuclear reaction mechanisms. In photonuclear physics itself, recent advances in accelerator technologies have allowed great strides to be made in the study of complex reactions involving small cross sections. Most of these advances have come in the form of high duty factor electron beams of high quality, although improvements in detector performance, and the rapid increase in computing power has also contributed. The most recent development, which is the focus of this present work, is the production of linearly polarised photon beams. Alongside this, advances in the development of theoretical understanding and the construction of more complex theoretical models have allowed a greater understanding of the underlying processes at work. Recent models incorporating polarised photons have predicted strong, measurable asymmetries which are very dependent upon the competing reaction mechanisms.

This chapter describes the progress in the study of photonuclear reactions, from early developments in the field, through recent experiments using unpolarised photons, up to the present work, which incorporates polarised photons together with the latest techniques and models. These measurements provide important information and strong constraints on photonuclear reaction mechanisms and interactions.

### 1.1.1 Photoabsorption

Photons have been widely used as probes for nuclear physics experiments for many years now, for two main reasons. Firstly the electromagnetic interaction

between the photon probe and the nucleus is relatively weak. This allows he photon to probe the entire nuclear volume and is a major advantage over sone hadronic probes which interact strongly, predominantly with the nuclear surface. Secondly, the basic electromagnetic interaction is well understood and the photon views the nuclear medium as a collection of nuclear charges, currents and magnetisation densities, to which it can couple. This ensures that any measurements provide information on these constituents. This again is an advantage over strongly interacting hadronic probes. Some of these features are visible on a pot of total photoabsorption cross section per nucleon for a collection of different nuclei [1], shown in figure (1.1). As can be seen, there are distinct featuresat

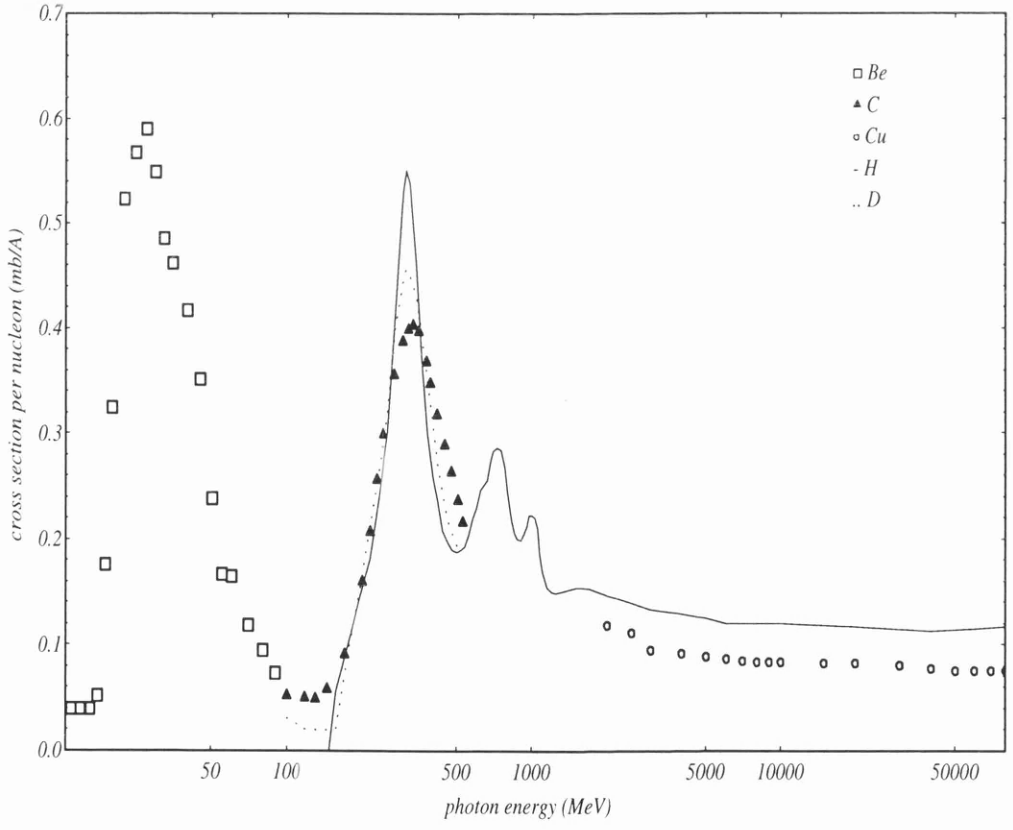


Figure 1.1: *Total Photon Absorption Cross Section per Nucleon*

different photon energies, and therefore different photon wavelengths. The large

resonance peak at ~30 MeV corresponds to collective excitations of the whole nucleus. Here the photon has a wavelength comparable to the size of a nucleus, and is absorbed mainly by electric dipole transitions. This causes an excitation of the whole nucleus, which then decays mainly by the emission of nucleons. This behaviour is described in terms of a collective model. The second peak at~300 MeV is known as the Delta resonance region. Here the photon has a wavelength comparable to the size of a single nucleon, so that a single nucleon can be excited to its first excited state, the $\Delta$ (1232) resonance, which rapidly decays via the production of a real or virtual pion. The width of the peak is in part due to the Fermi motion of the nucleons. In between these two peaks, at ~50-200 MeV, one can see the cross section is much reduced. In this intermediate region the photon has a wavelength in between the size of the nucleus and a nucleon. Photon absorption on single nucleons is greatly suppressed due to momentum conservation, leaving absorption by nucleon pairs (2N absorption) as the strongest process in the region. This picture of 2N absorption eventually led to the development of the quasideuteron model, (QD model) [2], which has since been greatly developed [3, 4, 5] and agrees well with a range of accurate measurements. The present work was conducted at photon energies between 150 and 360 MeV, spanning the top end of the intermediate region and most of the $\Delta$ resonance region, and thus covers a large region of interest.

### 1.1.2 The Quasideuteron, and Other Early Models

The QD Model, mentioned briefly above, was first developed by Levinger in 1951. In this phenomenological model the photon is absorbed by a *pn* pair, with the rest of the nucleus acting as a spectator. It was developed in response to the failure of earlier compound models which assumed a 2-step process in which the photon was absorbed, leading to an excited state, which decayed via

nucleon emission. The compound model was successful at low photon energies, but at higher photon energies it underestimated the number of emitted protons and failed to describe their angular distribution. More importantly the model failed to predict the observed cross sections for the production of protons with high momenta. Levinger speculated that photon absorption took place not on the whole nucleus, but rather on a *pn* pair within that nucleus. This *pn* pair provided an electric dipole moment to which the photon could couple. The model also allowed the proton to have high momentum in the initial state, which arose due to its close proximity and interaction with another nucleon. The model parameterises the observed QD cross section, $\sigma_{QD}$, in terms of the free deuteron cross section, $\sigma_{FD}$, thus:-

$$\sigma_{QD}(E_\gamma) \;=\; L\frac{NZ}{A}\sigma_{FD}(E_\gamma) \tag{1.1}$$

where $\frac{NZ}{A}$ represents the number of *pn* pairs in the nucleus, and L is the Levinger constant. This is effectively the relative probability that the *pn* pair are near each other in a nucleus and in a free deuteron. The original quoted value of L is 6.4 for photons of energies ~150 MeV. However the model fails to take into account factors such as final state interactions, (FSI) and Pauli blocking and so various values of L have been quoted by subsequent authors, whilst trying to make better fits to data for different nuclei. Levinger later proposed a modification [6], to include Pauli blocking.

A much more sophisticated treatment was developed by Gottfried [7]. He showed that, making some basic assumptions, the photoproduction cross section for *pn* pairs could be factorised as:-

$$d\sigma \;=\; \frac{1}{(2\pi)^4}F(P)S_{fi}d^3k_1d^3k_2 \tag{1.2}$$

where $k_1$ and $k_2$ represent the momenta of the *pn* pair. $F(P)$ is the probability of finding that *pn* pair with total momentum P , at zero separation, and can

be derived from the long range properties of the shell model wavefunction. The factor $S_{fi}$ is a transition probability matrix and includes the effects of short range interactions. When the *pn* pair are much closer than their average separation, the mean field wavefunctions are modified by the nucleon-nucleon repulsion described by the so called short range correlations (SRC). Making certain assumptions, one can replace this factor by the real deuteron photodisintegration transition probability and get back to the basic QD Model. These models were used for some considerable time until more recent work began to question the validity of the assumptions, which allowed the cross section to be factorised in this way. This has been discussed in detail by Ryckebusch *et al*, [8]. Their calculations showed that at low photon energies, below the $\Delta$ resonance region, the assumption that that the initial *pn* pair has 'zero' separation, i.e. small compared to the average nucleon separation, when the photon is absorbed by it was inaccurate. Also they found that absorption on $T = 1$ pairs is not negligible, as previously assumed. These lead to deviations from the factorised model. However, as the photon energy approaches the $\Delta$ resonance region, the *pn* pairs behave more like quasi-deuterons, and a factorised model is justifiable. This is helpful as unfactorised calculations are numerically very complicated. In their more recent calculations the effects of different meson exchange currents were examined, these effects not being included in the earlier models. The seagull, pion-in-flight and delta terms are now included, as well as some FSI. The effects of FSI are to reduce the magnitude of the calculated cross sections, whilst not affecting the shape of angular distributions. More recent developments include the addition of heavier meson exchange [9], as this work suggests that the angular distribution of the emitted *pn* pair is sensitive to the type of meson exchange current. This has been recently been confirmed experimentally [10].

We now turn our attention to experimental techniques.

### 1.1.3 Photon Tagging Experiments

Early photonuclear experiments using real photons were unable to reconstruct fully the kinematics of such reactions because they were unable to measure the energies of incident photons. Intense single energy (mono-energetic) photon beams were not available but various techniques have now been developed in order to measure the energy of individual photons, by so-called 'photon tagging'. There are three main photon tagging techniques used, and they are now discussed separately.

- Positron Annihilation:- $e^+ + e^- \rightarrow \gamma + \gamma$

  When an electron and a positron meet they can mutually annihilate, producing a pair of photons. Firstly, a weak beam of positrons is produced by passing a beam of electrons through a high Z radiator. These positrons are produced via the bremsstrahlung process and are then momentum analysed to determine their energy. The positron beam is then passed through a low Z radiator in which annihilation takes place with atomic electrons producing a pair of photons. These photons have equal energies in the centre of mass frame. However in the lab frame one photon generally has a higher energy than the other. The high energy photon is used to induce reactions in the experimental target and it is tagged by detecting the low energy photon in coincidence. The angle of the low energy photon is measured and from it, the energy of the high energy partner can be determined.

- Laser Backscattering:- $e^- + \gamma \rightarrow e^{-\prime} + \gamma'$

  Laser backscattering is also known as inverse Compton scattering. In this process a photon is scattered by a high energy electron, which gives energy to the photon. Experimentally a laser is used to produce low energy photons which are then collided with a beam of high energy electrons. The scattered

photons appear in a direction close to that of the electron beam. The detection of the recoil electron, in coincidence with a reaction product allows the photon energy to be determined.

- Bremsstrahlung:- $e^- \rightarrow e^{-\prime} + \gamma$

  In the bremsstrahlung process an electron is decelerated or 'braked', in the Coulomb field of an atom, producing a photon. As the nucleus is much more massive than both the photon and the electron, it receives virtually no energy in this process. This means that the photon energy will be simply the difference between the incident and residual energy of the electron. Experimentally a beam of high energy electrons is passed through a thin radiator producing an intense beam of photons, which are emitted in a forward peaked cone. The residual electrons are momentum analysed in order to determine their energy, and are detected in coincidence with reaction products. This allows the energy of the photon to be deduced.

The present experiment was carried out using the tagged bremsstrahlung technique at the Institut für Kernphysik, in the Johannes-Gutenberg Universität in Mainz, Germany. This is discussed in detail in Chapter 2.

### 1.1.4 Review of Previous ($\gamma$,2N) Experiments

Early ($\gamma$,2N) experiments [11, 12, 13, 14] used untagged bremsstrahlung techniques. This method did not provide an accurate determination of the photon energy and also had to make assumptions about excitations of the residual nucleus.

Another method, which was not used for $(\gamma, pn)$ experiments, was the bremsstrahlung difference technique which was used to obtain cross sections as a function of photon energy. The experiment was performed twice, at 2 slightly different electron

beam energies, and the results from the lower beam energy were subtracted from the results from the higher beam energy. Most of the resultant yield was due to photons between the two beam energies. However, the two bremsstrahlung spectra have slightly different shapes which can lead to a small tail of low energy photons being left over, producing large systematic errors.

However, bremsstrahlung difference techniques aside, the early untagged experiments strongly confirmed the emission of *pn* pairs. They also showed that the average opening angle of the *pn* pair in the centre of mass frame was similar to that for deuterons in elements such as $^{4}$He, $^{6}$Li, $^{12}$C and $^{16}$O. Also, the distribution of these opening angles was wider than that for the Deuteron, and this was attributed to the initial motion of the *pn* pair in the nucleus.

These experiments were limited in their nature, and it wasn't until photon tagging facilities were developed that more comprehensive experimental work could be undertaken. In parallel with these developments, large solid angle detectors were built, which allowed the ($\gamma$,2N) reactions to be studied in detail. The full determination of the reaction kinematics also allowed the excitation of the residual nucleus to be measured for the first time. The Glasgow group and its collaborators began to undertake ($\gamma$,2N) experiments [15, 16, 17], using a number of targets, $^{4}$He, $^{6}$Li, $^{12}$C and $^{16}$O. These experiments were made with photon energies between 80-157 MeV using a plastic scintillator hodoscope to detect charged particles, and an array of time-of-flight detectors to detect the associated nucleon. This system had a missing energy resolution of $\sim$7MeV, sufficient to resolve the shells from which the nucleons were emitted. The most extensive investigation into the ($\gamma$,*pn*) reaction was made on $^{12}$C. The results showed that much of the strength lay at low excitations of the residual nucleus, i.e. missing energies $\sim$20-40 MeV, where both nucleons were knocked out of the 1*p* shell. At slightly higher missing energies, $\sim$40-70 MeV, the data also supported the QD like model, with,

in this case, one nucleon coming from the $1p$ shell and the other from the $1s$ shell. The data [17] showed some small tails on their distributions, and this was attributed to the effects of FSI.

In the middle of the 1980's the MAMI facility at Mainz was upgraded [18] to provide an electron beam of energies up to 855 MeV. This and the construction of a new generation of detector systems allowed ($\gamma$,2N) experiments to be conducted at photon energies up to and through the $\Delta$ resonance region. Again the Glasgow-Edinburgh-Tübingen-Mainz collaboration conducted a series of experiments in this region [3, 4, 5]. Over the extended photon range 100-400 MeV, the results from the low missing energy region again confirmed the 2N knockout model with emission from the $1p$ shell. At medium missing energies the results showed knockout of $1p1s$ pairs, with some contribution from FSI. However, at missing energies between 20-40 MeV, one complementary study [19], estimated the transmission of neutrons in $^{12}$C and found an average transmission of $\sim$0.8$\pm$0.08. This was interpreted as an indication that FSI have a small effect. In the higher missing energy region, 70 MeV+, studies [20] showed that emission takes place via more complicated steps including contributions from three-nucleon absorption processes, initial quasi-free pion (QF $\pi$) processes and final state scattering. A study of the angular distribution of the ($\gamma$,$pn$) reactions [10], showed that at low missing energies and photon energies around 140 MeV, the ($\gamma$,$pn$) distribution is strongly peaked around 80$^o$. This was interpreted as evidence of heavy meson exchange between the $pn$ pair.

### 1.1.5 Introduction to Linearly Polarised Photons

As previously stated, in the general field of nuclear physics, polarisation variables and their phenomena have been found to be very helpful in differentiating between different reaction mechanisms. In the last few years theoretical groups have

started to turn their attentions towards polarised photons. Theoretical calculations showed that such experiments may provide important information on the form of the short range correlations between the *pn* pair and should be relatively insensitive to the effects of FSI.

The development of coherent bremsstrahlung and polarised laser backscattering sources has allowed high degrees of linear polarisations to be achieved. Recently a number of experiments [21, 22, 23, 24, 25], were conducted using polarised photons on light nuclei, ($^2$H, $^3$H, $^4$He and $^6$Li). These showed strong azimuthal asymmetries in the reaction cross sections, and are reviewed in more detail in section 1.3.2.

Theoretical calculations [26, 27], showed a strong sensitivity of the asymmetry of the $^{16}$O($\vec{\gamma}$,pn) reaction to the type of correlation function between the emitted *pn* pair. At Mainz, development work [28], led to the installation of an accurate and reproducible polarised photon source. In the light of these advances it was decided to conduct an experiment to measure the asymmetry of the $^{12}$C($\vec{\gamma}$,pn) reaction. The $^{12}$C($\gamma$,pn) reaction is now reasonably well understood but previous experiments using polarised photon sources had only been conducted on lighter nuclei. It is to the field of polarised photon experiments that we now turn our attention.

## 1.2 Production of Linearly Polarised Photons

### 1.2.1 Early Work

Interference effects seen in high energy bremsstrahlung, produced by crystals, were first noted in the 1930's, [29]. However it took almost 20 years before work by Ferretti [30] produced a formula which predicted intensity as a function of photon energy, as well as predicting maxima and minima in that intensity, as a

function of crystal orientation. The first approach to calculate intensity changes in a modified Bethe-Heitler (BH) spectrum due to interference effects, was made in the Born approximation, and was published by Überall in 1955 [31]. He presented a formula which allowed the calculation of intensity changes in BH spectra due to interference effects, but this had a smooth energy dependence and is shown in figure (1.2). Here the primary electron energy is 1 GeV. His later work [32, 33] showed that a photon beam from a crystal has a strong linear polarisation for certain directions. Experimental work by Bologna *et.al.* [34] showed spectra with a number of sharp peaks which they explained as arising from the discrete structure of the reciprocal lattice in the crystal. A plot of one such spectrum is shown in figure (1.3). Here an electron beam of 2 GeV energy is producing interference effects in a diamond crystal. The solid line represents their theoretical prediction. Further experimental studies [35, 36, 37], produced spectra from silicon and diamond crystals, and also showed that collimation of the photon beam results in a much reduced incoherent (unpolarised) background, with no appreciable effect on the intensity of the coherent (polarised) part, thereby increasing the degree of linear polarisation. More recently, the development of modern accelerator technology and photon tagging techniques has at last allowed experiments fully exploiting the polarised properties of coherent bremsstrahlung to advance.

### 1.2.2 Features of Coherent Bremsstrahlung

An authoritative treatment of coherent bremsstrahlung was published by Timm in 1969 [38], in which he listed the following properties of interference radiation:-

1 Interference in bremsstrahlung is only produced for high primary electron beam energies.

2 The radiation is directed strongly forward, in a narrow cone.

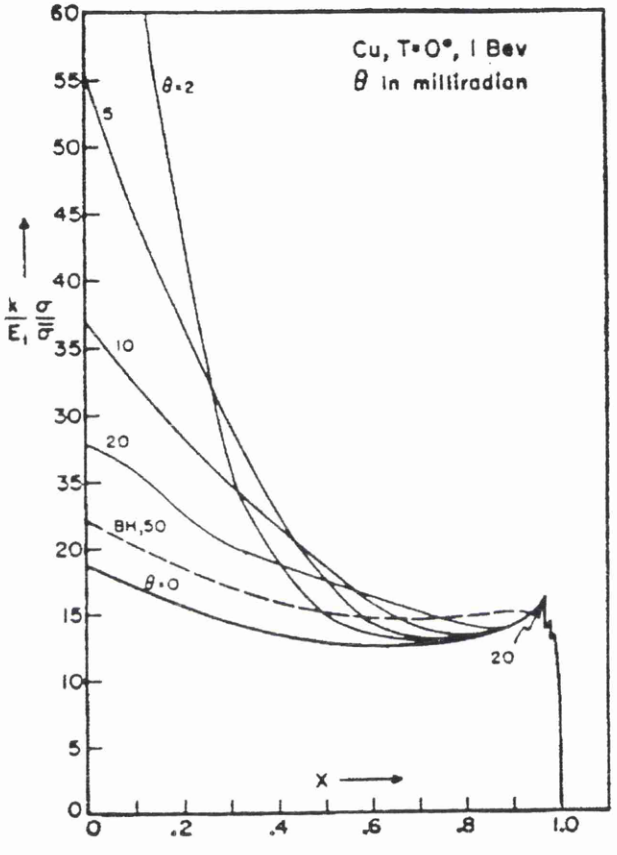


Figure 1.2: *Calculated BH Intensity Spectrum from a Cu Crystal at 1 GeV Electron Energy. Compared to the BH spectrum, the intensity is strongly enhanced, particularly for small orientation angles* $\Theta$. *Taken from reference [31].*

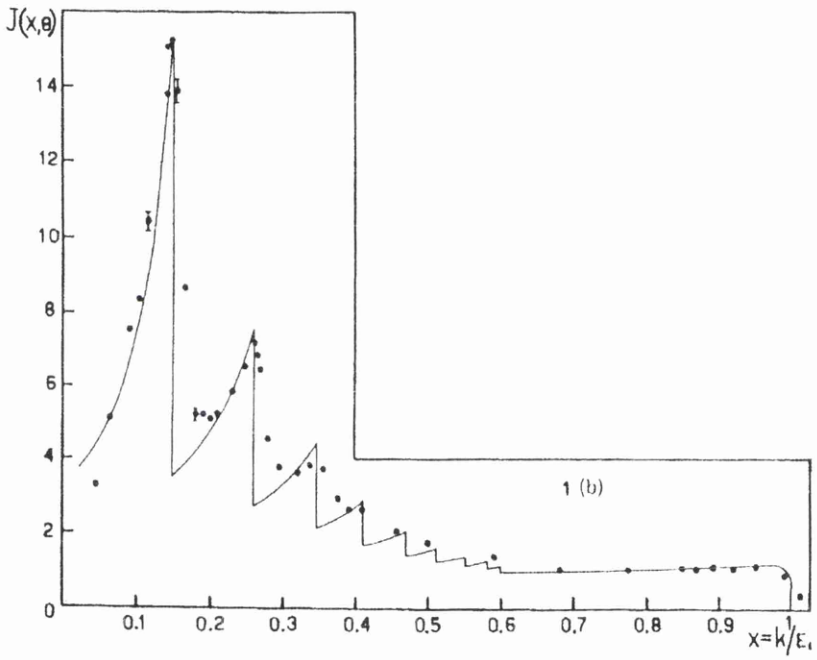


Figure 1.3: *Experimental and Theoretical Photon Spectrum from a Diamond Crystal*

3 The radiation is composed of 2 parts, a coherent part and a incoherent part. The incoherent background is due to lattice vibrations. The coherent part is an enhancement over the incoherent background, which increases strongly with electron energy.

4 This enhancement shows strong peaks and reflects the crystal lattice structure of the radiator.

5 The radiation in the intensity peaks has a high linear polarisation, which depends on the orientation of the crystal with respect to the electron beam.

6 The coherent fraction of the spectrum can be increased by applying tight collimation.

Interference effects arise from diffractive processes. In these processes, if the energy of the incident particle is high, then they are characterised by a small longitudinal momentum transfer $q_l$, to a third body, which may be a nucleus or a crystal. If the energy is high enough then $q_l$ may be small compared to $\frac{1}{a}$, where $a$ is the average atomic spacing in the crystal i.e.

$$q_l \ a \ll 1 \tag{1.3}$$

Here, the natural system of units are used, ($\hbar = c = m = 1$). So, according to the uncertainty relation, this implies that the effective dimension of the region involved in the diffractive process, $a_{eff}$ become very large:-

$$a_{eff} = \frac{1}{q_l} \gg a \tag{1.4}$$

so that it comprises an effective number of atoms, $N_{eff}$:-

$$N_{eff} = \frac{1}{q_l a} \tag{1.5}$$

and therefore diffractive processes become a significant effect.

### 1.2.3 Kinematics of Bremsstrahlung

The process of bremsstrahlung is described by the following relations:-

$$e + N \rightarrow e^{'} + N + \gamma \tag{1.6}$$

$$\mathbf{p_o} = \mathbf{q} + \mathbf{p} + \mathbf{k} \tag{1.7}$$

$$E_0 = E + k \tag{1.8}$$

where $e$, $e^{'}$ and $\gamma$ denote the initial electron, the final electron and the photon whose momenta and energies are given by $\mathbf{p_o}$, $\mathbf{p}$, $k$, and $E_0$, $E$, and $k$ respectively. Now, as well as equation (1.3), there are two further conditions for constructive interference. Firstly there is the periodicity of the crystal lattice and secondly there is the condition that the crystal lattice is properly orientated to the primary electron momentum, $\mathbf{p_o}$. The orientation of $\mathbf{p_o}$ is defined by the polar angle $\Theta$ and azimuthal angle $\alpha$ with respect to the system of crystal lattice axes $e_k$. Diamond is used as the crystal in the present experiment and has a cubic structure. So the lattice axes are [100], [010] and [001]. With $\Theta = 0$ we have a rotational symmetry around axis $e_1$. This rotational symmetry makes it natural to split the recoil nucleus momentum $\mathbf{q}$, into its longtitudinal and transverse components, [38], $q_l$ and $q_t$, where

$$q_l = p_o - p \ cos\Theta_e - k \ cos\Theta_k \tag{1.9}$$

and

$$q_t^2 = p^2\Theta_e^2 + k^2\Theta_k^2 + 2pk\Theta_e\Theta_k \ cos\Psi \tag{1.10}$$

Where $\Theta_e$, $\Theta_k$, and $\Psi$ are defined in figure (1.4). A minimum value of $q_t$ is obtained for a forward emission of both electron and proton, i.e. when $\Theta_e = \Theta_k = q_t = 0$.

$$q_l^{min} = p_o - p - k = \delta \tag{1.11}$$

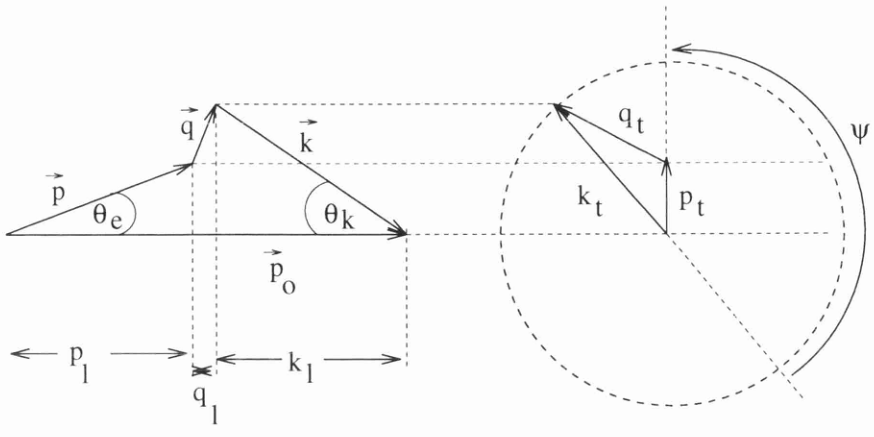


Figure 1.4: *Momentum Relations for Bremsstrahlung*

If we introduce the relative photon energy, $x$, such that

$$x = \frac{k}{E_o} \tag{1.12}$$

then it can be shown, [38], again for the natural system of units, that the recoil momentum **q** transferred to the nucleus, lies in a thin region of q-space and is given by:-

$$\delta \leq q_l <\approx 2\delta \tag{1.13}$$

$$0 \leq q_t <\approx 2x \tag{1.14}$$

where $\delta$ is the minimum longtitudinal recoil momentum and can be shown [38] to be given by:-

$$\delta = \frac{1}{2E_o} \frac{x}{1-x} \tag{1.15}$$

equations 1.13 and 1.14 now define the so-called 'pancake' condition, where $q_l$ is small and lies in a restricted region whereas $q_t$ is much larger. This was first noted by Überall, [31], who named it the 'pancake' condition after its thin disc shaped

form. This pancake is almost perpendicular to the momentum of the incident electron.

### 1.2.4 Polarised Photon Production

If a diamond crystal is used as a radiator then the direction of the momentum transfer can be non-isotropic due to the structure of the crystal. This results in polarised photons. For maximum polarisation only one set of crystal planes (represented by one reciprocal lattice vector), should contribute. This can be arranged by orientating the crystal so that only one reciprocal lattice vector lies in the 'pancake region'. For the present experiment this was arranged, [28], for the $[02\bar{2}]$ reciprocal lattice vector. Figure (1.5) demonstrates the setup for $E_\gamma$ = 340 MeV. The top 3 diagrams illustrate how the pancake moves as the photon energy increases from just before, through, and just past the discontinuity, $k_d$, of the $[02\bar{2}]$ reciprocal lattice vector. One can follow the arrows down through the diagram to the middle 2 plots showing calculations of the relative intensity and polarisation. The arrows then progress to the bottom 3 plots showing calculated 2-dimensional intensity distributions as a function of photon energy. As the pancake approaches from the left its unsharp edge begins to encroach upon the $[02\bar{2}]$ reciprocal lattice vector. The beam now gradually becomes more and more polarised. This gradual increase in polarisation is due to the fact that the upper value of $q$ is not sharp. As a point where $k = k_d$ the value of polarisation, $P$, reaches a maximum. Above $k = k_d$ there is a sudden fall in the intensity and the value of $P$. This is because the lower value of $q$, unlike the upper value, is sharply defined. In practice this fall is not completely sharp due to the finite divergence of the incident electron beam and multiple scattering of electrons in the crystal.

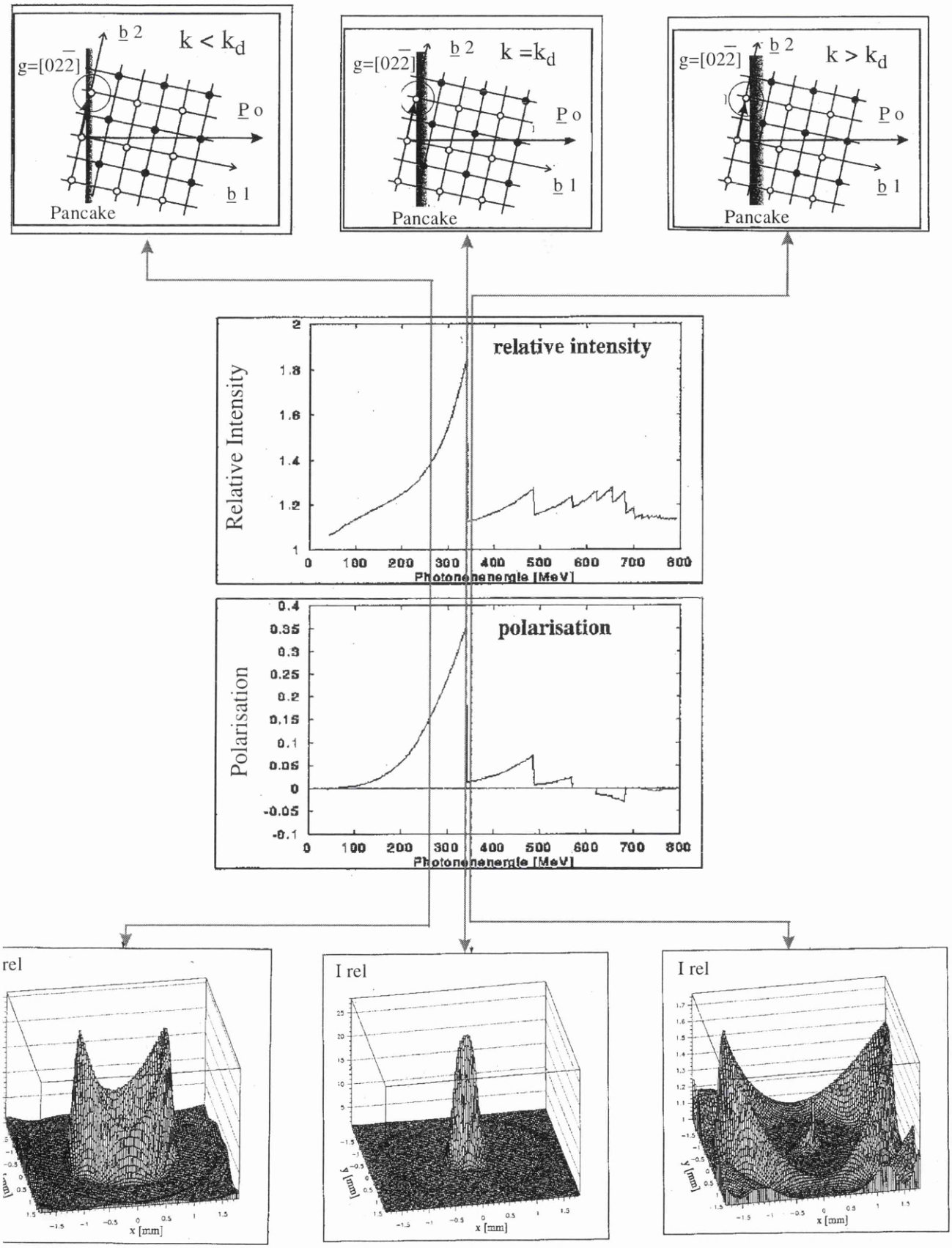


*Figure 1.5 Polarised Photon Production*

### 1.2.5 Crystal Alignment

In order to produce linearly polarised photons the diamond crystal must be carefully aligned so that the reciprocal lattice vector favourable for the production of linearly polarised photons at a chosen photon energy is selected. Figure (1.6) shows how the crystal angles are defined. $\theta$ and $\alpha$ are the polar and azimuthal

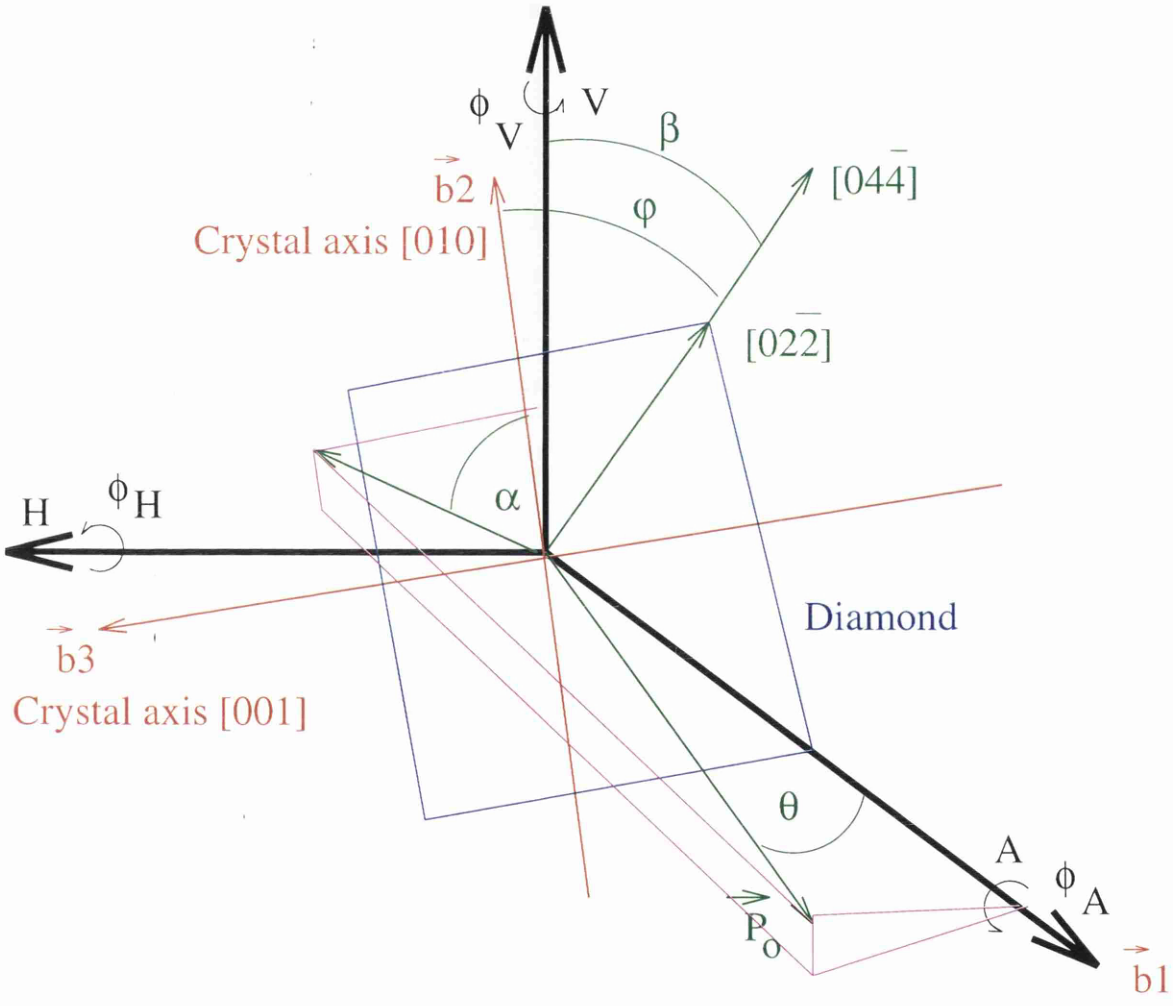


Figure 1.6: *Goniometer Angles*

angles of the primary electron momentum $\mathbf{p_o}$, in the $b_1 = [100]$, $b_2 = [010]$ and $b_3 = [001]$ reference frame. $\varphi$ is the azimuth of the reciprocal lattice vectors, g = $[02\bar{2}]$ and $[04\bar{4}]$, responsible for the production of coherent bremsstrahlung in the

same reference frame. $\beta$ is the angle between the plane of maximum polarisation and the vertical direction $V$. When $\beta$ = zero we define the plane of polarisation to be in the perpendicular (Perp) direction, when $\beta = \pi/2$ we define the plane of polarisation to be in the parallel (Para) direction. Previous studies [28], have shown that the high degrees of linear polarisation due to the $[02\bar{2}]$ reciprocal lattice vector can be produced from diamond crystals. Contributions due to higher order reciprocal lattice vectors are also produced but their degree of polarisation is much reduced relative to the $[02\bar{2}]$ vector. This is shown in figure (1.7) which shows a relative intensity spectrum, calculated using a code developed in Göttingen [39], using a diamond radiator. Relative intensity is defined thus:-

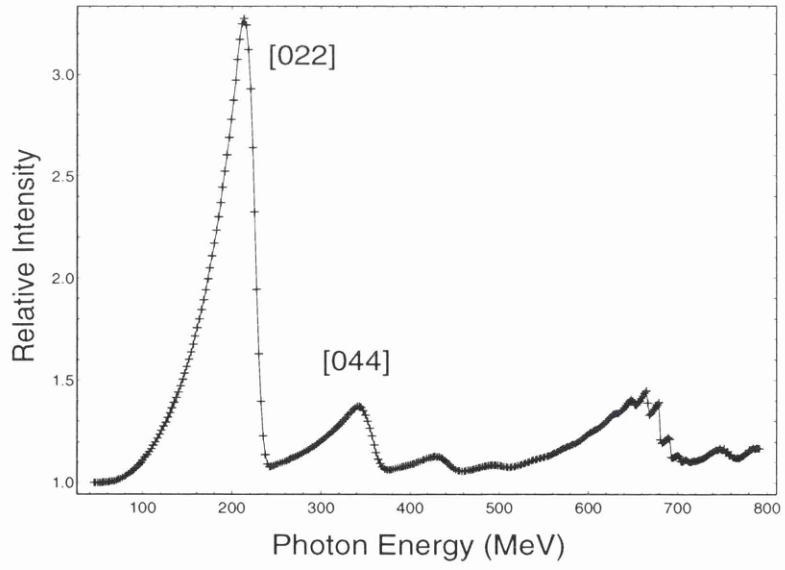


Figure 1.7: *Calculated Intensity Spectrum from a Diamond Crystal. The peaks due to the $[02\bar{2}]$ and $[04\bar{4}]$ Reciprocal lattice vectors are shown.*

$$I_{rel} = \frac{(I_{coh} + I_{incoh})}{I_{incoh}} \tag{1.16}$$

where $I_{coh}$ is the intensity due to the coherent contributions and $I_{incoh}$ is the intensity due to the incoherent contributions. The main peak at ~220 MeV is mainly due to the $[02\bar{2}]$ reciprocal lattice vector, while the next peak at ~350 MeV is mainly due to the $[04\bar{4}]$ reciprocal lattice vector. Changing the direction of the polarisation by rotating the crystal allows us to measure the reaction cross sections for polarisations, parallel and perpendicular to the reaction plane, [28]. In the present experiment the diamond crystal was mounted in an accurately controlled goniometer which allows careful alignment. This apparatus is described fully in the next Chapter, and the method of alignment is discussed in Chapter 3.

## 1.3 Polarised Photon Theory and Experiments

### 1.3.1 Review of Photon Asymmetry Theory

The purpose of the present experiment is to measure the asymmetry of the $^{12}C(\overrightarrow{\gamma},pn)$ reaction. The azimuthal variation of cross section for polarised photon reactions is given by:-

$$\sigma = \sigma_o(1 + P\Sigma cos2\phi) \tag{1.17}$$

where $\sigma_o$ is the unpolarised cross-section, P is the fractional polarisation of the photon beam, $\Sigma$ is the reaction asymmetry and $\phi$ is the azimuthal angle. Now, if $\sigma_{||}$ ($\sigma_{\perp}$) denote the reaction cross section when the plane of maximum photon polarisation is parallel (perpendicular) to the reaction plane, and if we assume the value of polarisation in each direction is the same. (i.e. $P_{||} = P_{\perp}$). Then:-

$$\sigma_{||} = \sigma_o(1 + P\,\Sigma) \tag{1.18}$$

and

$$\sigma_{\perp} = \sigma_o(1 - P\,\Sigma) \tag{1.19}$$

This then gives us a method of extracting the asymmetry, $\Sigma$:-

$$\Sigma = \frac{1}{P}\,(\frac{\sigma_{\parallel} - \sigma_{\perp}}{\sigma_{\parallel} + \sigma_{\perp}}) \tag{1.20}$$

Therefore, to measure the reaction asymmetry, we need to measure the reaction cross-sections for both directions of polarisation. It also follows that $\sigma_o$, the unpolarised cross section is given by:-

$$\sigma_o = \frac{1}{2}\,(\sigma_{\parallel} + \sigma_{\perp}) \tag{1.21}$$

### 1.3.2 Previous Experiments with Polarised Photons

Most previous measurements of photon asymmetry have been made on very light nuclei. Measurements of the $^2$H($\vec{\gamma}$,p)n and $^3$He($\vec{\gamma}$,pn) reactions were carried out by the LEGS collaboration, [24, 21]. The $^2$H($\vec{\gamma}$,p)n experiment was conducted at photon energies of 191 and 222 MeV and measured the photon asymmetry as a function of proton angle. Figure (1.8) shows the result at $E_\gamma = 222$ MeV. The asymmetry is strongly negative, reaching $-0.275$ at a proton angle of $\sim 105^o$ in the centre of mass frame, falling towards zero at extreme angles.

The $^3$He($\vec{\gamma}$,pn) measurement was carried out between 235 and 305 MeV. It again showed strong negative asymmetries and was consistent with that of the deuteron photodisintegration they measured. The data were well described by a calculation based on a 2N absorption mechanism on a *pn* pair.

Measurements of the $^2$H($\vec{\gamma}$,pn), $^4$He($\vec{\gamma}$,pn) and $^6$Li($\vec{\gamma}$,pn) reactions were made at the Yerevan Physics Institute [25, 23]. These were carried out at photon energies between 300 MeV and 1 GeV. Unfortunately these measurements were made with a restricted kinematical range and also a very poor energy resolution of $\frac{\Delta E_\gamma}{E_\gamma}$. More importantly all missing energies were included which makes

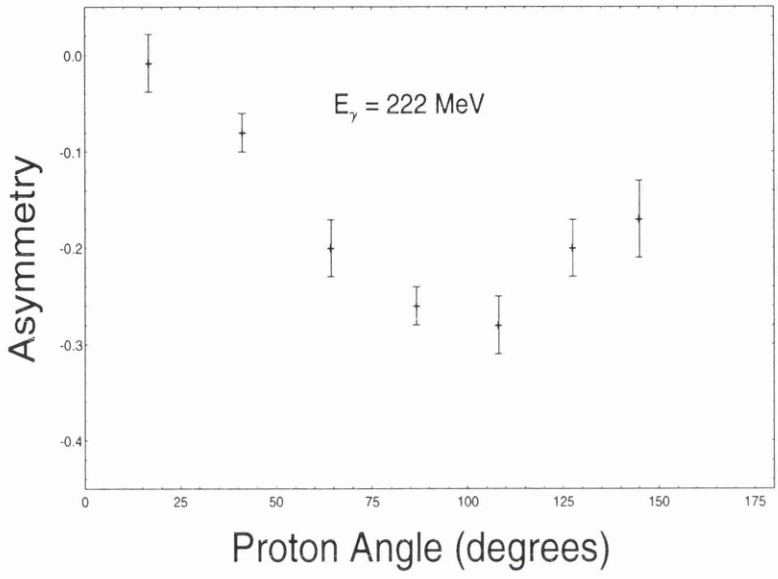


Figure 1.8: *Deuterium Angular Asymmetry as Measured by LEGS*

interpretation difficult because many processes contribute. These are shown in figure (1.9). As can be seen all of these data show the same distinct characteristic shape. Starting at ~300 MeV the measured asymmetries fall to a maximum negative value, then rise, crossing zero between 500 and 600 MeV. They then reach a maximum positive value at ~750 MeV, after which they fall very slightly. The similarity of the shape of the distributions may indicate some similarity between the mechanisms of real deuteron and quasideuteron photodisintegration. However, the magnitudes of the asymmetry appear to change for heavier nuclei. Also the energy at which the asymmetries cross zero is lower for heavier nuclei. The $^4$He data are clearly 'shifted upwards' compared to $^2$H data, and the $^6$Li also

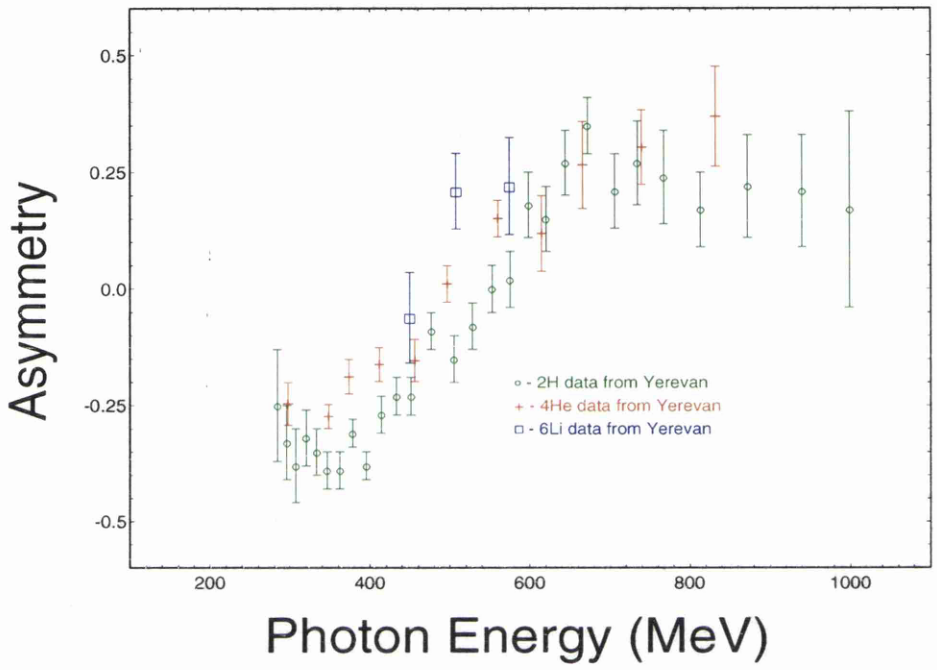


Figure 1.9: *Asymmetries for Light Nuclei Measured at Yerevan*

appears to be shifted up as well, although there are few data points in this set.

Because of the poor energy resolution in the Yerevan measurements, no attempt was made to measure the asymmetry in different missing energy regions. Therefore the data for $^4$He and $^6$Li will include 2-step processes which occur at relatively high missing energies, in addition to direct 2N knockout processes.

### 1.3.3 Theory with Polarised Photons

Calculations of photon asymmetry were made by Boffi and Giusti, [40, 27] on the $^{16}$O($\overrightarrow{\gamma}$,pn) reaction. These calculations investigated the sensitivity of the asymmetry to different correlation functions of the *pn* pair. The calculations were

made in the unfactorised approach and involved two trial Jastrow correlation functions, OMY and RSC. The OMY correlation function is based on hard-core NN interactions while the RSC correlation function is in the framework of calculations on nuclear matter with a Reid soft core potential [27]. The OMY correlation function has a strong hard repulsive core which results in large effects at short range. The RSC correlation function has a larger effect at medium range. These two correlation functions predict asymmetries of different signs as shown in figure (1.10), which gives the asymmetry as a function of the angle of the emitted proton, for events in symmetric coplanar kinematics. This is where the two nucleons are emitted on opposite sides with respect to the photon beam, with equal energy and angle. These differences are due to the effects of one and two body nuclear currents. In the calculations both the two-body seagull and delta isobar currents have been included [40]. The left-hand frames, (a), are calculated using the OMY correlation function and the right-hand frames, (b), are RSC calculations. The dot-dashed line is a result of the one-body current, the dashed line includes the seagull term and the solid line shows the result from a full calculation including the $\Delta$ term. As can be seen the angular dependence is essentially flat. The conclusion was that there is a weak dependence on the initial momentum of the *pn* pair. Therefore a measurement of photon asymmetry would be an important test of the nucleon-nucleon correlation functions. Figure (1.11) shows a plot of photon asymmetry as a function of photon energy. Again this calculation was made in co-planar symmetric kinematics. As can be seen, the two correlation functions predict similar asymmetries at $\sim$80 MeV, where the asymmetry for both calculations is driven by the seagull term. However, as $E_\gamma$ increases the two results diverge, with the asymmetry for the OMY correlation remaining positive whilst the calculation based on the RSC function goes negative. This shows that a measurement would be a firm test of the reaction mechanism. The calculations

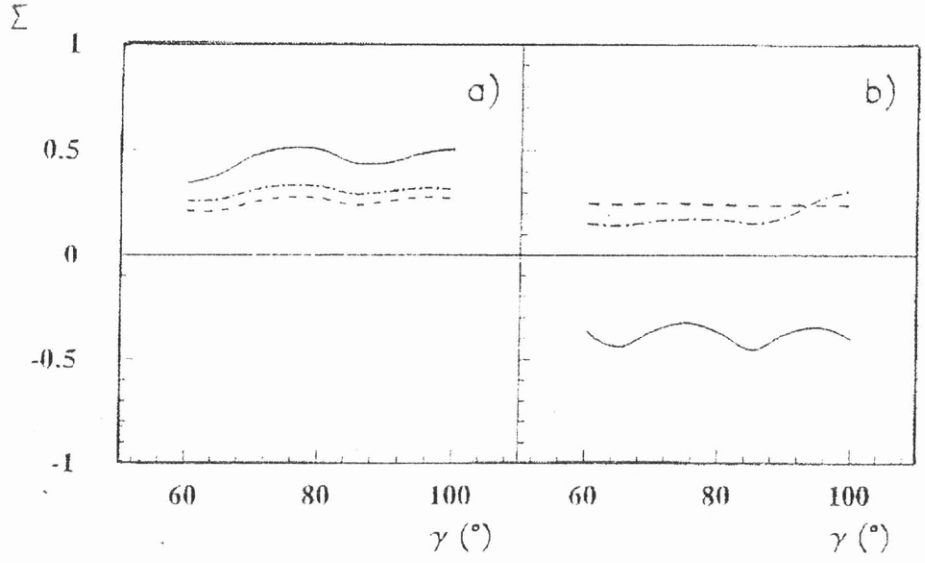


Figure 1.10: *Calculated Angular Dependence of Asymmetry for the* $^{16}O(\gamma,pn)$ *reaction. Photon asymmetry* $\Sigma$ *is shown versus the angle,* $\gamma$*, of the emitted proton. The photon energy is 250 MeV. The dot-dashed line shows the contribution from the one body current, the dashed line includes the seagull term and the solid line is the full calculation.*

[40], also show that FSI have only a small effect on the angles of the outgoing nucleons and should have a relatively small effect on the reaction asymmetry. Again an experimental measurement would test this prediction.

### 1.3.4 Recent Theoretical Developments

The most recent theoretical advances have been made by the Gent group [41]. The models discussed in the last section are limited by the number of reaction mechanisms they include. They include only 2-body photoabsorption mechanisms and do not include the pion photoproduction channels, [41]. The Gent code

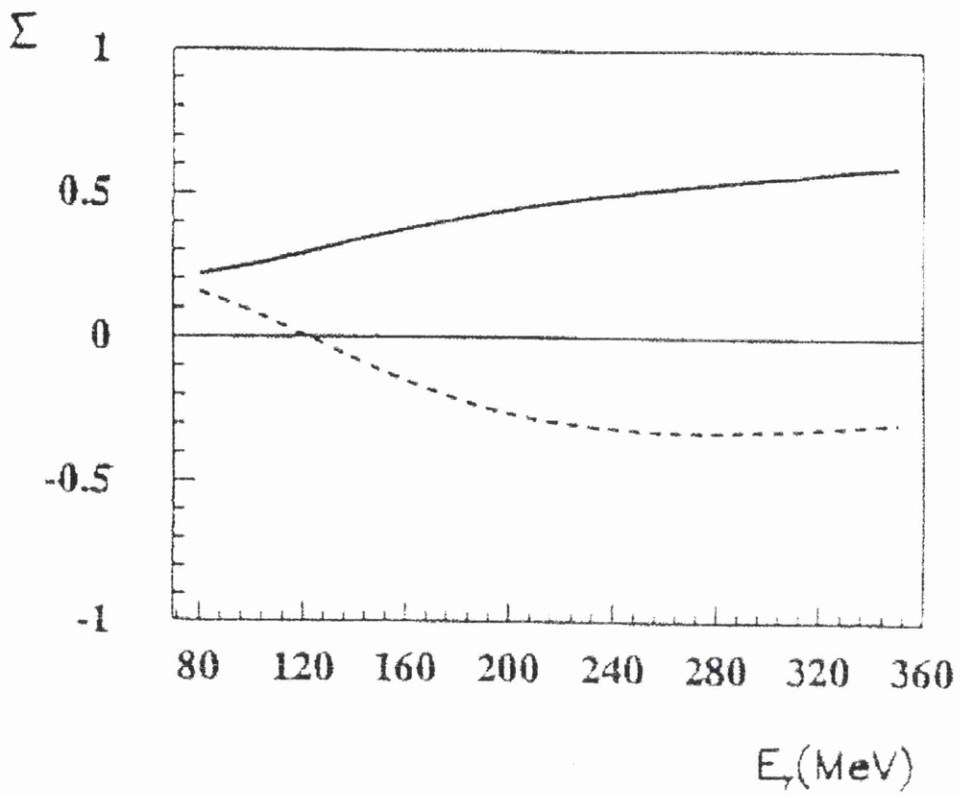


Figure 1.11: *Calculated Photon Dependence of Asymmetry for the* $^{16}O(\gamma,pn)$ *Reaction. The solid (dashed) line is obtained with the OMY (RSC) correlation.*

is unfactorised and includes a more complete treatment of the pion exchange currents. This model therefore represents the best currently available theory. The Gent group allowed use of their code for the present work.

The code allows various parameters to be selected and adjusted. Firstly the model accounts for the outgoing nucleon waves. Either distorted outgoing nucleon waves or a plane wave approximation can be selected. Next the orbit from which each nucleon escapes may be chosen. This can be either $1s_{1/2}$, $1p_{3/2}$ or $1p_{1/2}$. Figure (1.12) shows a plot of calculated asymmetry as a function of proton angle at 220 MeV. The calculation is summed over all proton energies and averaged over all neutron directions and energies. It shows the various contributions to

asymmetry for the possible combinations of p-shell nucleons. The final choices

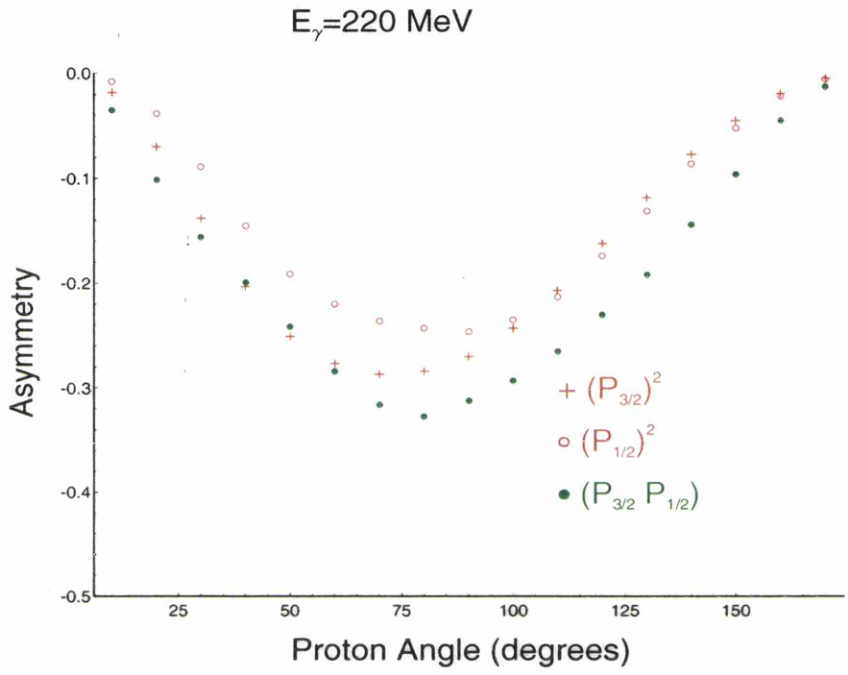


Figure 1.12: *P-shell Contributions to Asymmetry*

allow the type of pion exchange current, the type of $\Delta$ term and the short range correlation function to be selected. Figure (1.13) shows the effect of changing some of these parameters, at $E_\gamma = 220$ MeV for the $(1p_{3/2})^{-2}$ case. The green line shows the calculated asymmetry in a full distorted wave treatment, when including only the seagull pion exchange current. As can be seen this predicts a positive asymmetry. Next the magenta line shows the effect of including a pion-in-flight term (PIF), which is to change the sign of the asymmetry and also to change its magnitude considerably. The red line is a full distorted wave calculation including both pion exchange terms and a $\Delta$ term which reduces the magnitude of the predicted asymmetry. Finally the blue line is a calculation in

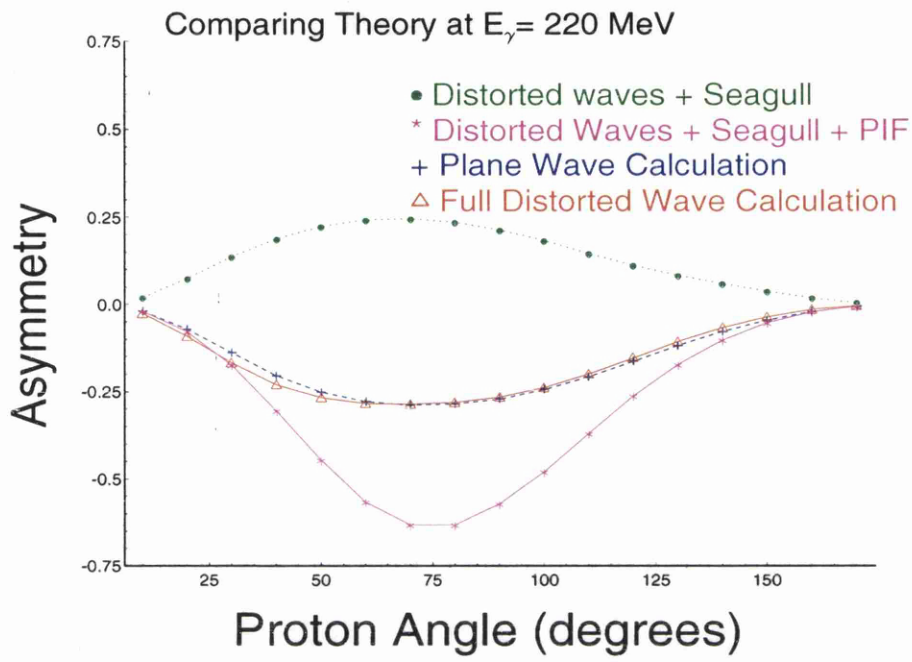


Figure 1.13: *Different Theoretical Contributions*

the plane wave approximation. Comparing the full distorted wave calculation with the plane wave approximation one can see that the asymmetry is hardly affected by the outgoing nucleon distortions.

This model was the one selected to compare with the measured experimental results, and its use is discussed in Chapter 5.

## 1.4 Scope and Aims of Present Work

The work presented in this thesis is the study of the asymmetry of the $^{12}C(\overrightarrow{\gamma},pn)$ reaction, at photon energies in the $\Delta$ resonance region. The data collected have sufficient statistics to allow divisions into a number of photon energy bins. For

each photon energy bin the dependence of the asymmetry on a range of kinematic variables including missing energy, recoil momentum and proton polar angles is investigated.

Comparisons are made between the measured results and the predictions of the Gent code. This allows some conclusions to be made regarding the competing microscopic reaction mechanisms, and the role of FSI. The results are also compared with previous data measured on lighter nuclei, which may reveal important trends, such as how asymmetry changes with mass number.

The next Chapter describes the experimental apparatus used to conduct this experiment and Chapter 3 describes the process of calibrating the various parts of the experimental system. Details of the methods used in analysing the data are described in the Chapter 4, and Chapter 5 discusses the results and their interpretations. Chapter 6 is a short conclusion.

# Chapter 2

# Experimental Apparatus

# Introduction

This chapter describes the apparatus used in this experiment. The experiment described here was carried out at the Institut für Kernphysik at the Johannes-Gutenberg Universität in Mainz, Germany using the Glasgow photon tagging spectrometer and the PiP/TOF particle detector systems.

The electron beam generated by the Mainz microtron MAMI-B is used to produce linearly polarised photons. The electron beam strikes a diamond radiator mounted in a accurately oriented goniometer. The energies of the photons are then calculated by momentum analysis of their associated recoiling electrons in the tagging spectrometer. The photon beam is then collimated before it strikes a nuclear target. The reaction products are then detected by the PiP/TOF detector systems placed on opposite sides of the photon beam. PiP is a segmented scintillation detector used to detect charged particles such as protons and charged pions, and TOF is an array of plastic scintillators used to detect the associated particles and measure their energies by time-of-flight analysis. Particle selection separates charged and uncharged particles and also separates particles such as pions, dueterons and tritons. Particle selection is possible in TOF by using two half rings of thin scintillator detectors surrounding the target. The other half of the $\Delta$E ring on the PiP side is used to make a start signal for the reaction. When useful events have been identified by the trigger electronics the on-line data aquisition system collects and stores the timing and charge information from the QDC's and TDC's connected to the detectors.

## 2.1 The Mainz Microtron (MAMI-B)

The Mainz microtron, MAMI-B, was developed [18] to satisfy the needs of research groups working at Mainz for a continuous wave (c.w.) electron accelerator

| Microtron No. | I | II | III |
|---|---|---|---|
| Input Energy MeV | 3.5 | 14.4 | 179.8 |
| Output Energy MeV | 14.4 | 179.8 | 855 |
| No. of recirculations | 18 | 51 | 90 |
| Energy gain MeV | 0.6 | 3.24 | 7.5 |

Table 2.1: Some parameters of MAMI-B

with energies up to 1 GeV. A duty cycle of almost 100% and a maximum beam intensity of 100$\mu$A has been achieved although the maximum beam energy is only 855 MeV.

The system itself consists of an electron injector followed by a cascade of three race track microtrons, each boosting the energy of the beam up to a maximum output energy for that stage, as given in Table 2.1. The injector itself is a 100 keV electron gun and a short LINAC which raises the energy to 3.5 MeV and feeds the first microtron (stage I). Race track microtrons themselves, see figure (2.1), consist of a linear accelerating section (linac), with klystrons providing radio frequency power to the accelerating cavities via wave guides. Bending magnets then recirculate the beam through separate return pipes which is possible due to the increasing radial trajectory of the beam. Each circuit corresponds to an integer number of wavelengths of the accelerating field, thus allowing the electrons to rejoin the linac in phase with the field. This process then continues many times with only a slight increase in energy in each turn thus reducing the relative power requirements required at each stage. After the maximum energy has been reached the beam is extracted and although it still has a radio frequency microstructure, the modulation frequency of 2.5 GHz is too high to be seen by the particle detectors and the beam can be considered to be continuous. A

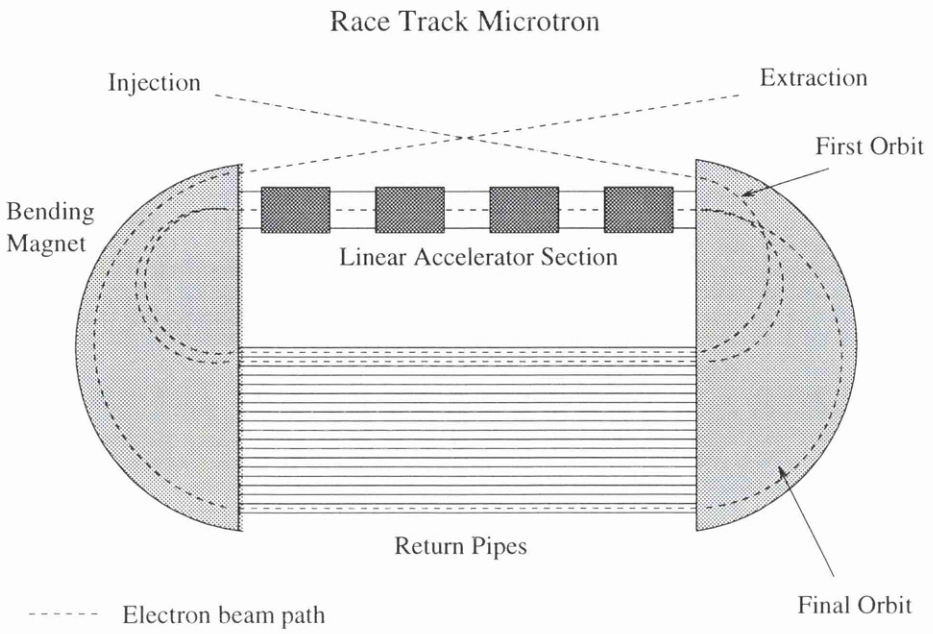


Figure 2.1: *A racetrack microtron*

continuous beam has the advantage of allowing a much higher rate of real to random coincidences than is possible using pulsed beams for the same average current.

Each stage then increases the beam energy up to 855 MeV, table (2.1). The extracted beam is then steered by dipoles and focussed by quadrupoles along tunnels into the experimental halls, figure (2.2), where it arrives with an emittance of $\leq$0.04 mm.mrad. Low emittances are required for coherent photon beam production and the Mainz Microtron provides one of the lowest currently available.

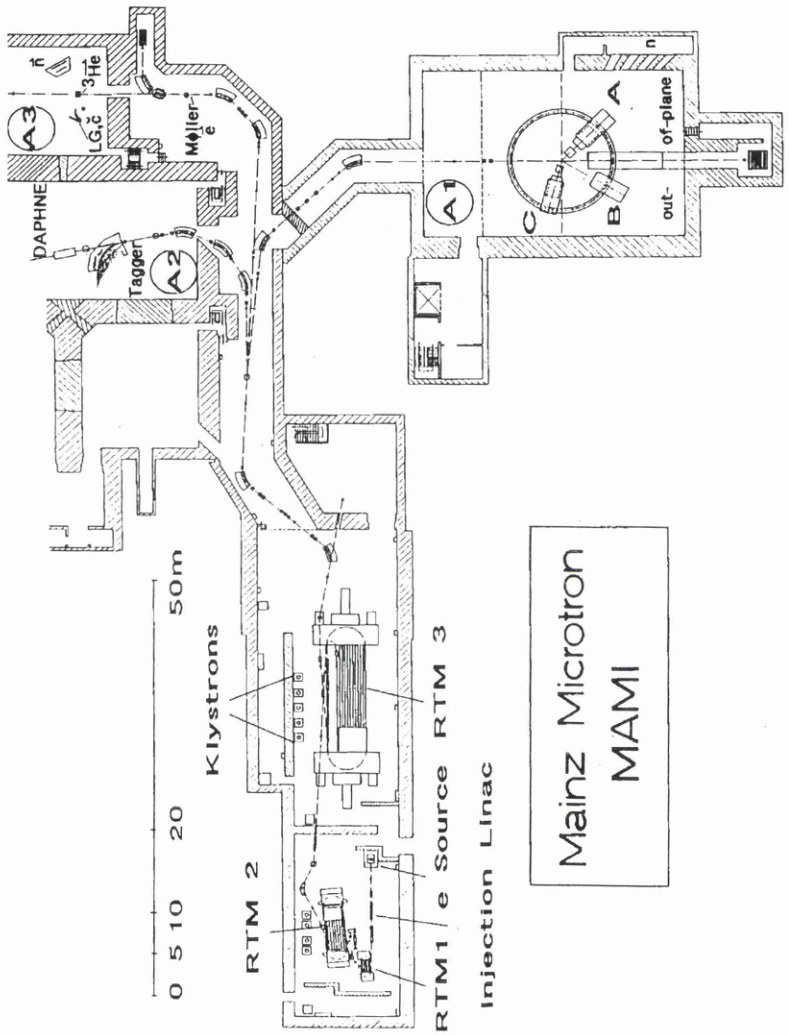


Figure 2.2: *Schematic diagram showing the Mainz Microtron*

## 2.2 Photon Production and Tagging

### 2.2.1 The Goniometer

The electron beam provided by MAMI hits the diamond radiator, which is mounted inside a high resolution goniometer. This goniometer, figure (2.3) is equipped with three step motor drives which allow rotations about the horizontal H, vertical V and azimuthal A axes [28]. In addition two displacements ZT and XT are possible allowing the Goniometer to be accurately positioned in directions perpendicular to the beam line.

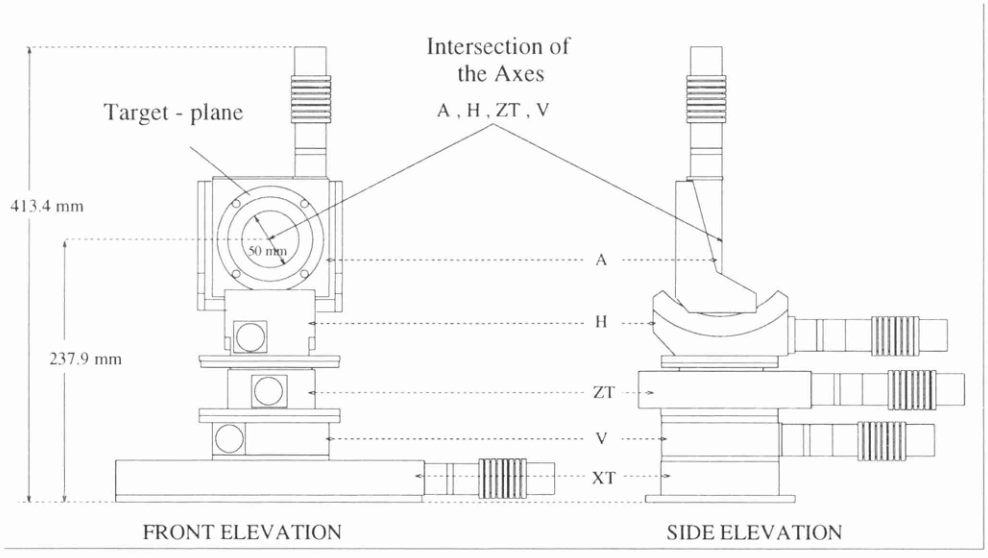


Figure 2.3: *The Goniometer*

**A** The Azimuthal axis. This axis lies approximately in a horizontal plane. It is exactly horizontal to the H-axis when its rotation is in its zero position. Rotation here is around an axis which is parallel to the electron beam when both the H and V axis rotations are in their zero positions.

**H** The Horizontal axis. Rotation here is around a horizontal axis perpendicular to the vertical axis. H is also perpendicular to the electron beam when the

vertical axis rotation is in its zero position.

**V** The Vertical axis. Rotation here is around a vertical axis fixed in space and therefore perpendicular to the electron beam direction.

**ZT** This allows linear vertical displacement of the entire apparatus, perpendicular to the electron beam.

**XT** This allows linear horizontal displacement of the entire apparatus, perpendicular to the electron beam.

**Electron beam** For the side elevation, this is incident from the right.

The definition of the Goniometer angles is given in section 1.2.5 and is shown in figure (1.6). The radiators are mounted inside a ring, figure (2.4), which rotates and moves them into position. The two types of radiator used in this experiment were Nickel, which produces incoherent bremsstrahlung and diamond, which produces coherent bremsstrahlung. The nickel radiator is 4 microns thick and the diamond 100 microns. The diamond crystal is in its zero position when the crystal axes [010], [001] and [100] coincide with the goniometer axes V, H and A being in their respective zero positions.

The choice of radiator required can be controlled from the experimental room and the ring can rotate along the A axis and can move along the XT axis, allowing the chosen radiator to be moved into position. These two operations allow any one of the five radiators to be placed in the electron beam, but only the central diamond radiator can have its spatial orientation finely adjusted. The degree and intensity of the linearly polarised photons produced depends on the three crystal angles $\alpha$, $\theta$ and $\phi$ as discussed in Section 1.2. Before starting the experiment the crystal must be orientated such that the reciprocal lattice vectors most favourable to the production of linearly polarized photons are aligned with respect to the

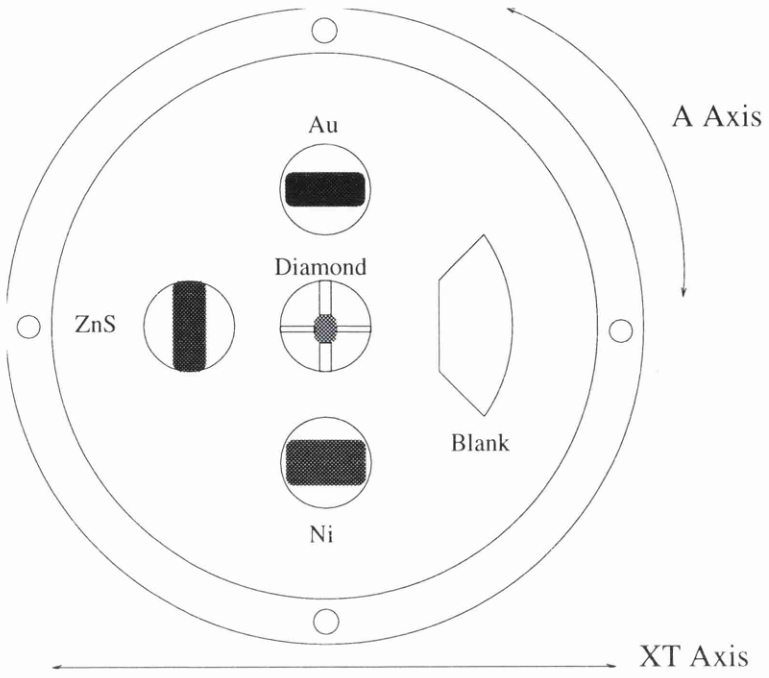


Figure 2.4: *The Radiator Ring*

electron beam line. This is done by moving the goniometer into position through known angles and is conducted from the experimental room. This process is discussed in the next chapter.

### 2.2.2 The Photon Tagging Spectrometer

The photon tagging spectrometer is used to momentum analyse the recoiling electrons which have produced bremsstrahlung photons in the radiator and therefore allows us to determine the energy of those photons. The energy of the injected electron beam is known to be 855MeV and therefore the photon energy is simply that energy less the energy of the recoiling electron. The tagging spectrometer, figure (2.5) was designed with the following considerations [42]. Firstly it has a large momentum acceptance, the ratio of $P_{max}$ to $P_{min}$ is approximately 16 to 1 allowing it to tag photons in the energy range 40-790 MeV. Low photon energy sections of the tagger ladder may be switched off allowing it to run at a higher

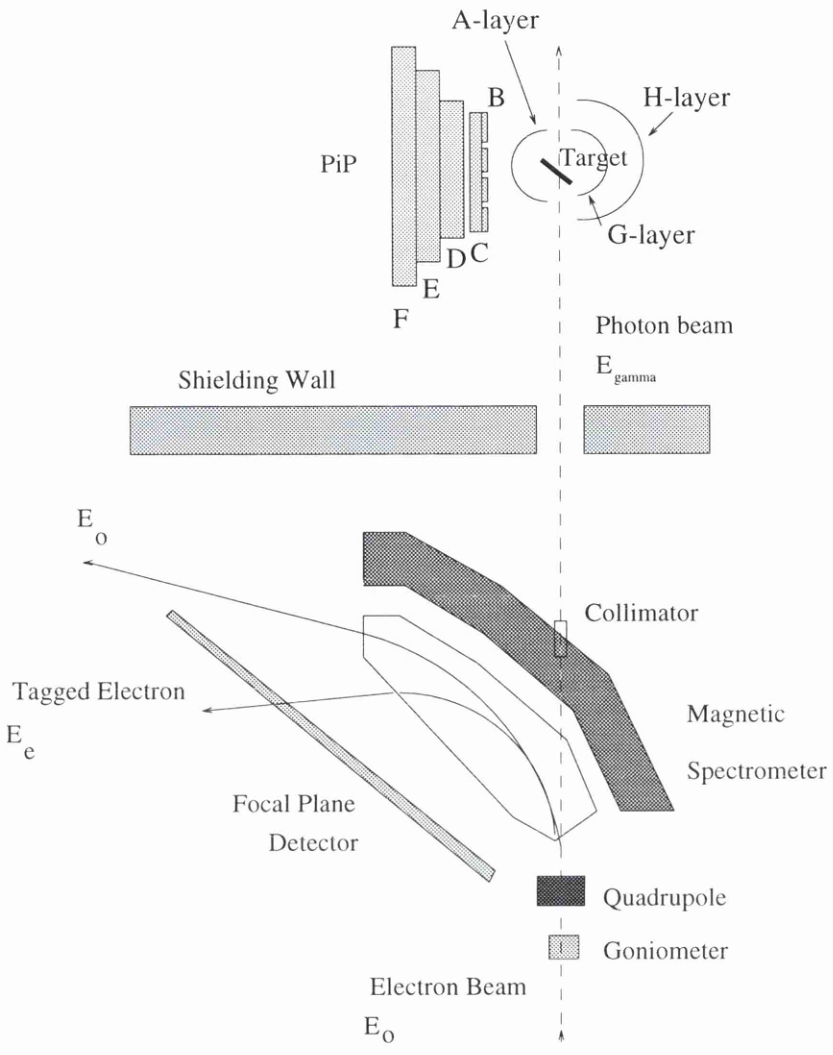


Figure 2.5: *The Photon Tagging Spectrometer*

overall counting rate as there are proportionally more lower energy photons. A single magnetic field setting is used to cover the entire momentum range and a nearly straight focal plane and good vertical focusing allow a simple overall design with a small pole gap. The residual electron acceptance is high, allowing $> 95\%$ percent of the radiated photons to be tagged. The magnetic field itself has a high homogeneity, $< 0.5\%$, and this contributes to a good overall intrinsic energy resolution of $\sim$ 120 keV.

### 2.2.3 The Focal Plane Detector

The design of the focal plane detector called for a system which could both run at a high rate and also measure the energy and timing information of each photon accurately enough for the purposes of experiments such as this one. The design chosen was an array of 353 overlapping plastic scintillators covering the whole length of the focal plane [43]. Each of the scintillators has its own photomultiplier tube (PMT), connected to a discriminator and a coincidence logic unit. The overlapping of these units allows us to define an event as a coincidence between two neighbouring channels, thus reducing the number of background events.

All of these focal plane counts or 'hits' are recorded by scalers. The scalers count every photon and therefore allow the total photon flux to be known. These scalers are disabled while any event is being read out, and are switched on again once the system is ready for the next event. TDCs allow timing information between focal plane hits and the PiP/TOF detectors to be used to determine possible coincidences.

### 2.2.4 Photon Collimation

Since the distance between the goniometer and the target is 7.5m collimators must be used in order to ensure a small beam spot at the target. Two sets of collimators are used. The first consists of a removable set of lead collimators on the outside of the magnetic spectrometer, 250cm downstream from the radiator. The diameter of these collimators may be changed but for most of this experiment collimators of 3mm diameter were used. A second set of lead collimators was placed just before the experimental target and these were used to stop charged particles produced by the first set from reaching the $\Delta$E detectors near to the beam. At the target the beam spot is estimated to be $\sim$ 10mm in diameter,

which results in an uncertainty of less than one degree in the trajectory of the emitted particles.

### 2.2.5 Tagging Efficiency

The collimators used help determine the beam size and improve the degree of polarisation but they also remove some photons whose corresponding electrons have already been tagged and counted by the scalers at the focal plane. Therefore a measure of this proportion, or tagging efficiency $\epsilon_t$, must be made. This is done during separate tagging efficiency runs using a lead glass detector placed directly in the photon beam to count the coincidences between photons passing through the collimators and electrons detected in the focal plane detector. The lead glass detector has a length of 30 radiation lengths and therefore detects almost 100 % of the photons entering it. The tagging efficiency is thus defined as:

$$\varepsilon_t = \frac{\text{lead glass} - \text{ladder coincidences}}{\text{ladder counts}} \tag{2.1}$$

Tagging efficiency measurements were made periodically during the whole experiment, both for polarised and unpolarised photons. These measurements were made at a very low electron beam current to allow the lead glass detector to count every photon. At these low count rates there were almost no random coincidences.

During normal experimental running a scintillator screen viewed by a high sensitivity TV camera is placed at the end of the photon beam line. This allows operators in the control room to view an image of the profile and position of the beam and therefore monitor any change in these parameters.

## 2.3 The Experimental Targets

Two types of target were used during this experiment, graphite sheets and deuterated polythene ($CD_2$). Both targets are 10cm square sheets, 2mm thick and were mounted at an angle of $\sim 30^o$ to the photon beam line. $CD_2$ is used in order to allow the detectors to be calibrated. The kinematics of the deuterium breakup reaction are overdetermined allowing an energy calibration to be made.

The targets were mounted in a holder which in turn was mounted on a remotely controlled target table. This enabled the targets to be moved up and down, into and out of the beam. The angle between the target and the beam could also be varied. This target angle is chosen so that the target can intercept all the photons. Previous measurements [10] have shown that a target angle of $30^o$ gives a compromise between the extremes of large charged particle energy losses resulting in a large uncertainty in proton energy at $90^o$, and a loss of proton angular resolution from a large spot size at $0^o$. Energy losses in the target make a significant contribution to the overall resolution; a 50 MeV proton travelling through 2mm of carbon will suffer an energy loss of about 4 MeV.

## 2.4 The Particle Detector Systems

The PiP and TOF detector systems were originally designed to study ($\gamma$,NN) and ($\gamma$,$\pi$N) reactions. With this in mind a number of requirements were needed. Firstly they had to have good particle discrimination, allowing various reaction products such as protons, neutrons, pions, deuterons and electrons to be identified and clearly separated from each other. Secondly they had to have sufficient energy resolution to allow different nuclear shells to be distinguished. Thirdly a wide angular range and reasonable angular resolution were required. Finally the electronics should have a fast response allowing time of flight techniques and a

high photon flux to be used. These requirements have been met and the various parts of the system are outlined in detail below.

The overall layout of the detector systems in the experimental hall is shown in plan form in figure (2.6). Figure (2.7) shows a 3D view of the same diagram. The beamline through the tagger can be seen and PiP is on the left of the beam line while the TOF stands can be seen to the right.

### 2.4.1 The Delta Detectors

The delta detectors consist of four separate detector systems surrounding the target, are shown in figure (2.8). These systems are separate on the PiP and TOF side of the experiment and provide two separate functions. The A and I-layers are on the PiP side of the experiment and the G and H layers are on the TOF side. The A-layer is known as the start detector. It consists of a half ring of seven thin plastic scintillators covering an angular range of 165 degrees. Its distance from the centre of the target is around 110mm and being that close, any coincidence of its signal with PiP should imply a charged particle coming from in or near the target. Such coincidences are used in a first level trigger for the experiment. The timing of signals in the start detectors determines the trigger timing and provides the start signal for all the TDCs, hence the name.

The G layer on the TOF side consists of a ring of eight thin plastic scintillators covering an angular range of 190 degrees. These scintillators are used as a veto detector for the purposes of neutral particle identification. During the experimental runs these veto detectors were not in the triggers, but during off-line analysis the veto is employed. If a particle makes a signal in the G layer it is classed as a charged particle. If a particle makes no signal in both the G and H layers then it is classed as a neutral. This process is fully explained in Chapter 4. The I layer on the PiP side is used as a possible veto for the one TOF stand

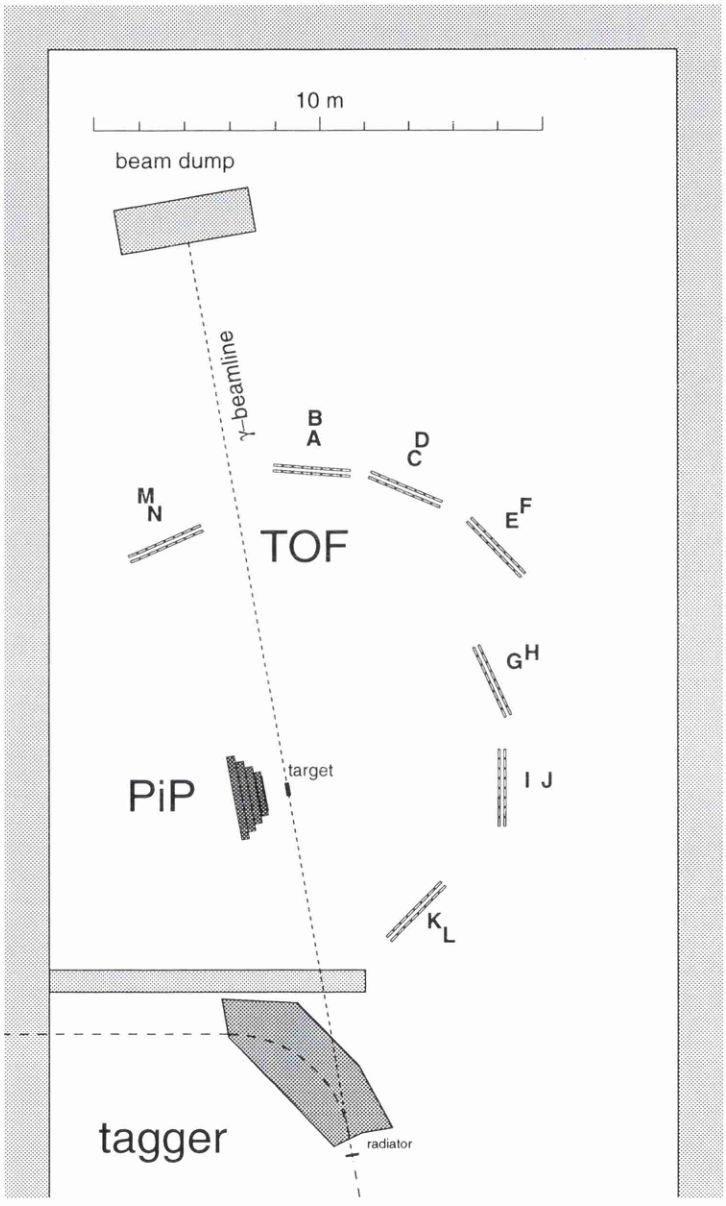


Figure 2.6: *The Experimental Layout*

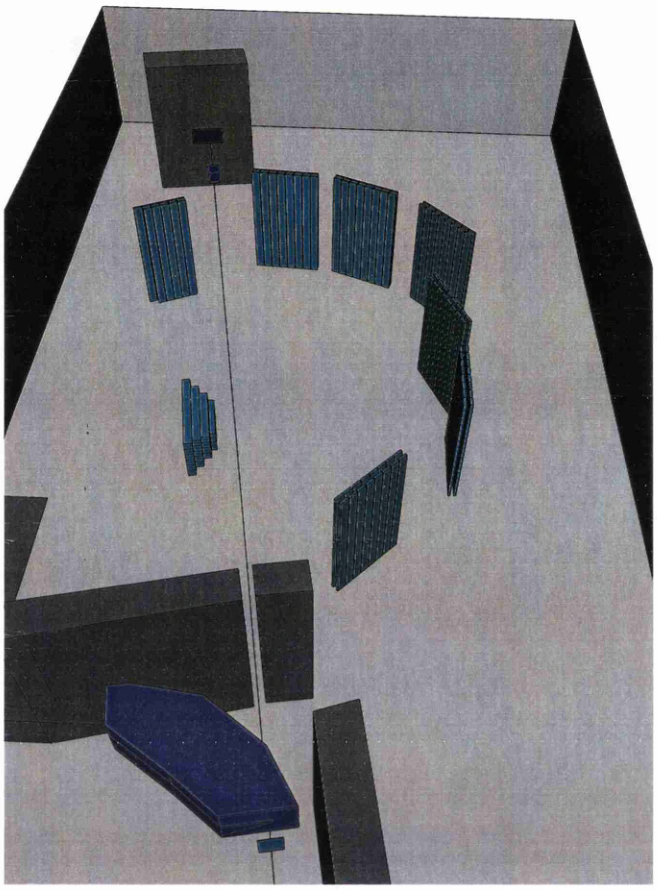

Figure 2.7: *3D View of the Experimental Layout*

placed on the PiP side of the experiment.

### 2.4.2 PiP

PiP is a large segmented charged particle detector [44] It consists of five separate scintillator layers laid side-on to each other, figure (2.9). These separate layers consist of firstly a $\Delta$E layer, (B-layer), which consists of four vertical elements; then four E layers (the C, D, E and F-layers), each larger than the previous one. These consist of a series of horizontal elements, the dimensions of which are shown in table (2.2).

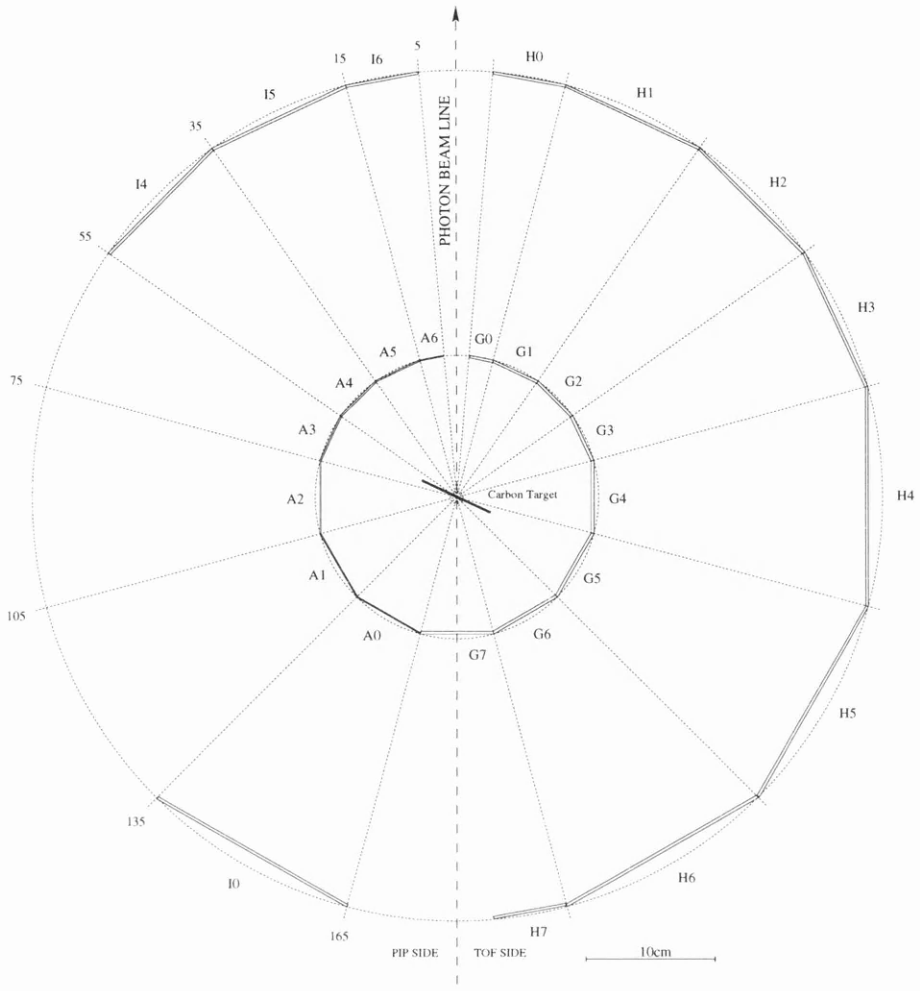


Figure 2.8: *The Delta detector rings*

Each of the elements is made from the plastic scintillator NE110. Each element has a light guide and a photomultiplier tube attached with silicone rubber to each end, allowing ease of replacement. Each of these elements is highly polished in order to maximize light transmission and then wrapped in black card and tape to ensure they are light tight. The wrappings were made as thin as possible to minimize particle energy losses. Each of the elements in a block is then mounted in a stand and each stand is then mounted inside the frame of PiP, which keeps the whole structure rigid. The frame is surrounded in steel plates to provide shielding from background atomic electrons, a stable heat environment

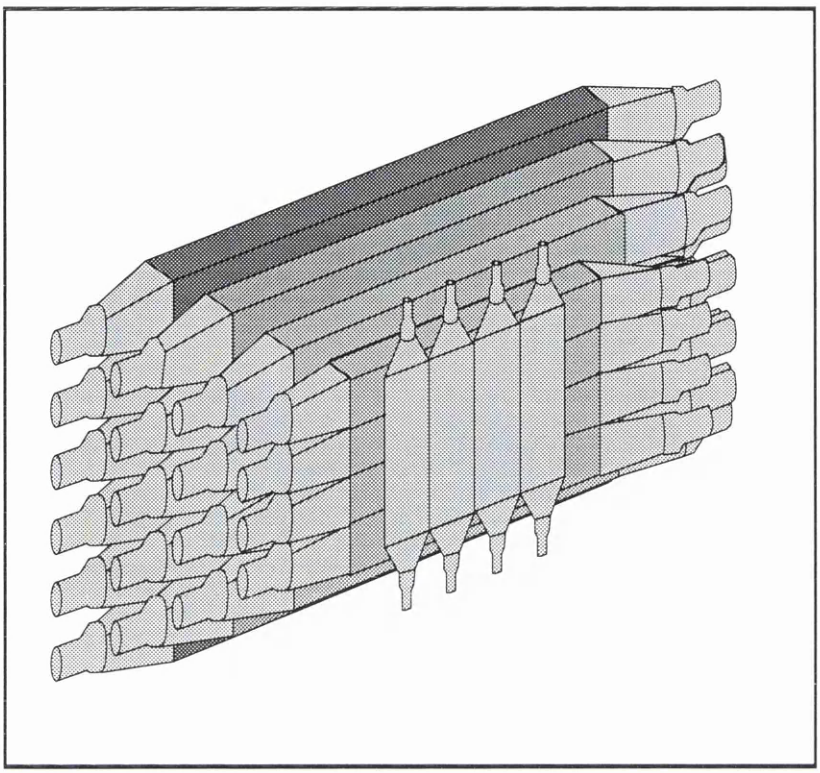

Figure 2.9: *A schematic view of PiP*

and additional strength. PiP itself also contains a secondary structure at the back containing all of its electronics.

### 2.4.3 TOF

TOF consists of an array of 108 separate time of flight detectors [45]. Each bar is a 3m long plastic scintillator made from NE110 and is 20cm wide and 5cm thick. Each bar has a light guide and a photomultiplier tube attached to each end. The bars are each wrapped in aluminium foil and rubber in order to prevent light leaks. Eight bars are arranged on a stand, figure (2.10), and stands were mounted two together in order to increase the detection efficiency of neutrons. This arrangement makes it possible to position the stands where

| Layer | no of elements | Size LxDxH (cm) |
|---|---|---|
| B | 4 | 200x0.2x42 |
| C | 4 | 100x11x13.5 |
| D | 4 | 130x17.5x17.5 |
| E | 5 | 160x17.5x17.5 |
| F | 6 | 190x17.5x17.5 |

Table 2.2: Dimensions of the PiP layer elements

required. The primary purpose of these detectors is to detect neutrons. These uncharged particles are detected by secondary processes such as proton knockout. This process is facilitated by the fact that plastic scintillator contains a high density of hydrogen atoms. The recoiled proton is then detected from the light produced as it slows down in the scintillator. The pulse height produced by the proton generally only gives a lower limit to the energy of the incident neutron and therefore that energy is found by time of flight measurement. For this reason long flight paths and thin bars are required for good energy resolution. We are able to discriminate between charged and uncharged particles by using the G and H-Layer veto detectors mounted close to the target, as previously described in Section 2.4.1

### 2.4.4 Gain Monitor System

Each of the scintillators used in PiP and TOF are equipped with a gain monitoring system consisting of light flashers. These are ultra bright light emitting diodes (LEDs), whose light output is monitored by temperature stable PIN-diodes. The LEDs are of type Hewlett Packard HLMP-8104. Each LED feeds sixteen photomultiplier tubes simultaneously via plastic lightfibres connected directly onto

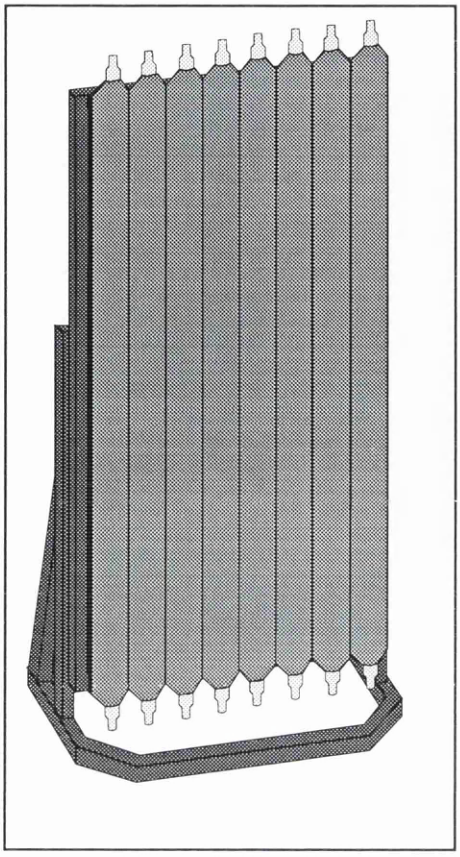

Figure 2.10: *A schematic view of a TOF stand*

the lightguide at the end of a scintillator bar. In addition to monitoring gain stability this system was also used to calibrate the rise times of the leading edge discriminators used. This is discussed fully in the next chapter.

## 2.5 Electronics and Data Acquisition

The on-line data acquisition system serves two purposes. Firstly it has to accept the required raw signals from the photomultiplier tubes, which contain both timing and energy information, whilst rejecting information from events that are not

required. This is achieved by way of trigger logic. Secondly it has to take the selected data and store it on disk or tape for later off-line analysis.

### 2.5.1 Detector Electronics

The electronics attached to each detector [46] have to convert the raw signals from the photomultiplier tubes into digital information. For this purpose every PMT in PiP and TOF is provided with a QDC and a TDC. The energy information is contained in the form of charge which is digitised by charge-to-digital converters (QDCs). They do this by integrating over the pulse within a region which is set (or 'gated') by the triggers. The types of QDCs used in this experiment were Phillips 10c2 units which are high density and contain 32 channels each. The timing information is processed by time-to-digital converters (TDCs). The raw signals are first passed through a leading edge discriminator which gives a logic pulse once that signal rises above a preset threshold. However the timing information is all relative to the start time and this is provided by the start detectors. Once the first level trigger issues a start logic pulse all the TDCs are started and then a signal anywhere else in the detector system will cause the relevant TDC to give a stop pulse thus providing the timing information required. A diagram of one of the PiP sub-circuits is shown in figure (2.11). Note this is for the PiP C-layer but all the other layers in PiP and to some extent TOF all follow this same basic pattern.

### 2.5.2 Trigger Logic

The trigger logic is employed in order to make decisions about which events to keep and which to disregard and under what conditions to apply these decisions. The trigger system is controlled by two Lecroy 4508 programmable logic units

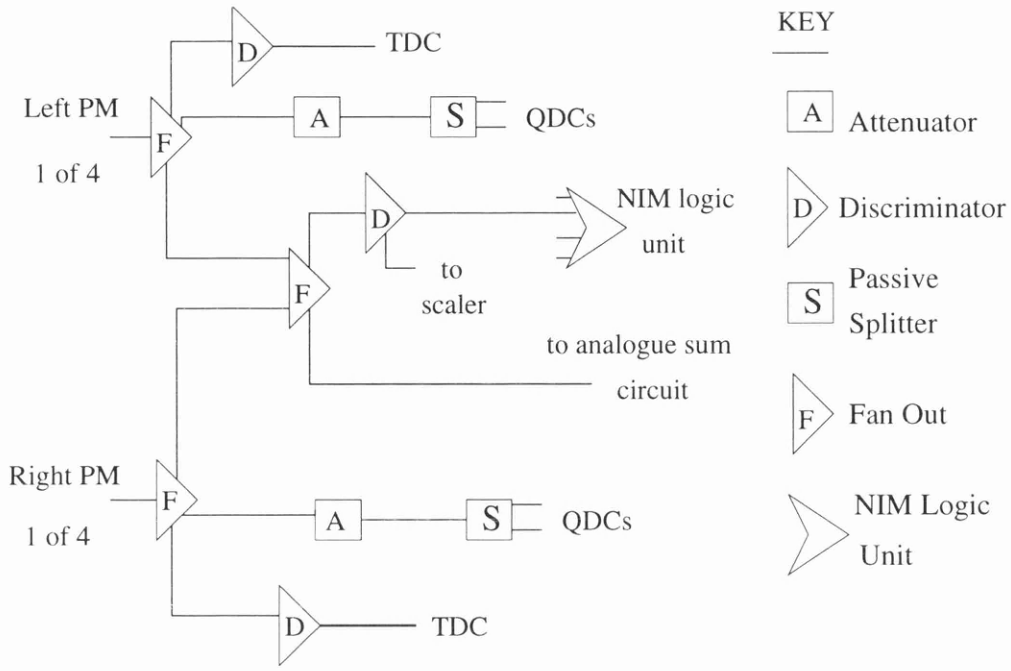


Figure 2.11: *The PiP C-layer sub-circuit*

(PLU's) which provide the trigger decoder. Each PLU can be supplied with up to eight logic inputs and can be programmed so that any combination of inputs will produce any combinations of desired outputs. These input and output combinations can be changed at any time.

These 'hardware triggers' consist of three levels. A first level trigger using signals from PiP makes fast decisions, and rejects a large number of random events. This first level trigger also employs cosmic and flasher inputs as sub-triggers for keeping calibration events. The second level trigger employs a circuit to reject background electrons and pions in PiP. Finally the third level trigger is then employed to make a final decision as whether to keep or reject events that have been so far selected. In addition to these hardware triggers a number of software options are employed which make use of combinations of the hardware triggers. These software options are varied according to the type of run being made.

### First level trigger

The first level trigger is employed to make a quick decision as whether to reject the event or whether to postpone that decision pending consideration of more detailed information. Listed below in table (2.3) are the inputs to and outputs from the PLU.

| Input | Output |
|---|---|
| PiP particle | PiP particle |
| TOF particle | TOF particle |
| PiP Cosmics | PiP start |
| PiP Flasher | TOF start |
| TOF Flasher | Tagger start |
| Reference | To 2nd level |
| Tagg Efficiency | Interrupt |
| Empty | Reset |

Table 2.3: *First level trigger Options*

It identifies particles in PiP, TOF, cosmic rays in PiP and flasher events in both PiP and TOF and also recognizes tagging efficiency events. Once trigger inputs have been accepted the PLU is then disabled to prevent any other events from being accepted. The output results are shown on the right. For events the relevant QDCs are gated, but if more than one trigger is present at the same time then that event will be rejected. Cosmic ray events are identified in the D, E and F layers of PiP by a coincidence between the top and bottom blocks at the same time resulting from a cosmic ray particle passing vertically through PiP.

### Second level trigger

This trigger is employed in order to reject the large background of electrons generated by atomic processes at the target and within PiP. These events, which contribute the largest background component in PiP, can be rejected by making hardware cuts on summed analogue signals from A + C, B + C and C + D layers. These are equivalent to 'diagonal cuts' on two-dimensional plots of A layer vs C layer, B layer vs C layer and C layer vs D layer amplitudes. The slope of such a cut can be altered by changing the attenuation of the linear signals summed in the circuit and by the magnitude of the cut by the discriminator threshold. The effect can be seen across the bottom left hand corner of figure (2.12). Electrons

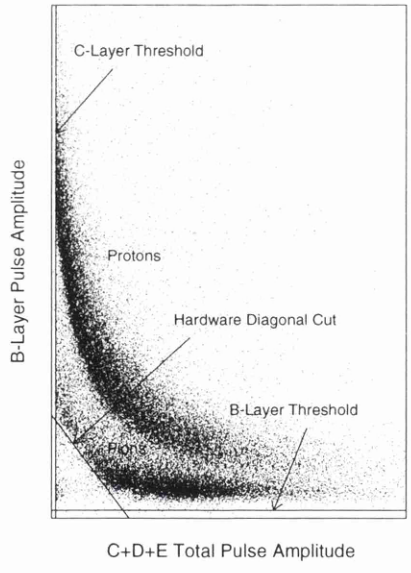


Figure 2.12: *Electron Rejection*

are found in this region due to the fact that they are easily stopped in PiP and in turn deposit relatively little energy in both the B and the C, D and E-Layers.

### Third Level Trigger

The Third level trigger is the final trigger and its role is to apply conditions which are firmer than the previous ones. Again below is listed its inputs and outputs in table (2.4).

| Input | Output |
|---|---|
| PiP from level 1 | Interupt and store |
| TOF from level 1 | Fast clear |
| From level 2 | |
| Pion | |
| TOF OR | |
| Tagger OR | |
| PiP alone | |
| Empty | |

Table 2.4: *Third level trigger Options*

This level is essentially a trigger for each of the 3 particles from the tagger, PiP and TOF. The electron reject has now been made. The TOF OR has a requirement of a coincident hit in TOF and so reduces experimental dead time. The tagger OR requires at least one electron in the tagger. The pion trigger was not used in this present experiment. If the conditions are met then the event is stored and the system reset for the next event. If any condition is not met then the event is rejected and the whole system is 'fast cleared' and reset. PiP alone does not require a hit in TOF, and may be used for certain requirements.

**Software Options**

During this present experiment a total of 22 software option triggers were used. These are divided into types according to the requirement of the run being made and are loaded into the software before that run commences. Examples of the most commonly used triggers are listed below.

Trigger A. This Trigger was used for $^{12}C$ and empty target runs. It is an EXCLUSIVE OR of the following:-
(PiP level 1) AND (PiP level 2) AND ((TOF OR) OR (PiP alone)) AND (Tagger).

Trigger B. This trigger was used for the CD2 runs used for calibrating the detectors. It is an EXCLUSIVE OR of:-
(PiP level 1) AND (PiP level 2) AND (Tagger).

Trigger C. This trigger was used for tagging efficiency runs and consists of:-
(Lead glass detector) AND (Tagger).

Trigger H3. This trigger is called a combined trigger because it combines two types of reactions. Here we were looking for for ($\gamma$,NN) events and the trigger consisted of the following:-
(PiP level 1) AND (PiP level 2) AND (TOF OR) AND (Tagger).

During the experiment many more of these triggers were used for purposes such as cosmic ray runs, pedestal runs which calibrate the QDCs, runs for calibrating discriminator thresholds and runs for pion selection only.

### 2.5.3 The Data Acquisition System

The data acquisition system, known as ACQU [47] controlled all the hardware used. It consists of an Eltec E7 computer equipped with a Motorola 68040 chip

mounted on a single board. The operating software used was OS9. The trigger electronics were controlled by a VME bus system and the data were transferred via TCP/IP ethernet connections. During experimental runs data acquisition was controlled from the experiment room outside the experimental hall using workstations. These ran the UNIX operating system and were linked to the E7 via an ethernet. Initial data storage was made on a 4Gbyte hard disk and later transferred to 8mm data cartridges. The on-line version of ACQU, written in 'C' allowed the display of many types of spectra. This enabled the on-line monitoring and control of the detector and other systems.

# Chapter 3

# Detector Calibrations

# Introduction

Information on events from the $^{12}C(\vec{\gamma},pn)$ reaction channel comes from the detector QDC's and TDC's as channel numbers and contents. Detector calibrations are required in order that this raw data can be converted into physical quantities such as energies and angles. Some of these calibrations can be done from data taken using the experimental $^{12}C$ target, whilst most of the calibrations are made using data taken during specific calibration runs. The techniques used in the calibrations of each of the detector systems are outlined in this chapter.

## 3.1 The Goniometer

Before data taking could begin on this experiment it was necessary to calibrate the goniometer so that linearly polarised photons were produced at the required energies. The goniometer is unique in the experimental apparatus as it is the only system which requires calibrating completely before the experiment can begin.

As discussed previously the goniometer is equipped with three step motors that enable rotations around the horizontal H, vertical V and azimuthal A axes. Rotations around these axes are defined as rotations through three angles $\phi_H$, $\phi_V$ and $\phi_A$. This is shown in figure (1.6). Previous work [28] provided recommended orientations for the production of linearly polarised photons of a given energy. In order to select a required photon energy, the angles $\alpha$, $\phi_V$ and $\phi_H$ are selected from tables. Calibrations are then made by firstly aligning the goniometer axes to a setting which is close to the required values. This approximate setting is found from look-up tables. This approximate setting is then adjusted by measuring the photon spectrum shape, using the measured count rate of residual electrons in the tagger detector channels. This method is known as scanning. This is measured as a function of one of the goniometer angles. Figure 3.1 shows such a scan for

the angle $\phi_H$. The main peak in the spectrum at low photon energies (around tagger channel 300), is due to the [0 2 $\bar{2}$] reciprocal lattice vector. A scan is also done for the other goniometer angle $\phi_V$. Higher order reciprocal lattice vectors may also be seen. From these scans the zero of both angle scales is established and the the exact angles required to position the cut-off in the coherent spectrum are determined for each required photon energy. During the data taking runs the

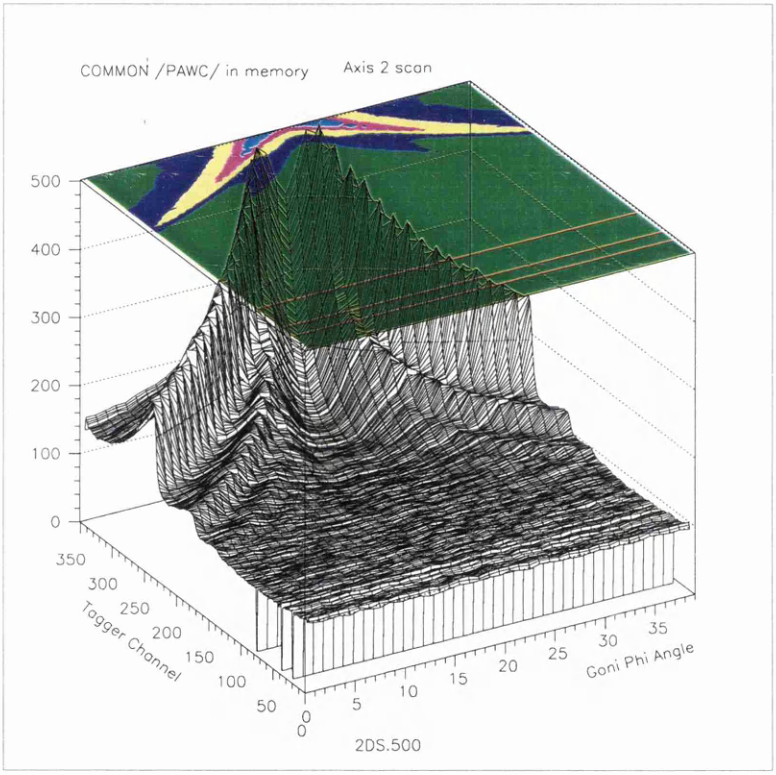


Figure 3.1: *A Goniometer Scan*

position of the peak in tagger channel space is carefully monitored for any drift.

## 3.2 Pedestals and Thresholds

### 3.2.1 Pedestal Subtraction

QDC's are used to convert detected charge into a number which is proportional to the amount of light deposited by an ionizing particle. QDC's integrate charge over the set time of the gate but a problem arises due to the fact that even when there is no signal, there is still a constant DC current in the QDC. As the QDC integrates over the gated time it will register that current and give a small output. In order to correct for this calibration runs are made for both the PiP and TOF detectors during which these signals, or 'pedestals', are read and recorded. This then allows the pedestal signal to be subtracted from all the QDC's. For pulses which are detected, the true charge $Q_t$ is just the charge recorded, $Q_r$ less the pedestal value P:

$$Q_t = Q_r - P \tag{3.1}$$

### 3.2.2 Discriminator Thresholds

The leading edge discriminators used in the PiP/TOF detector system define the limits of that system's energy acceptance. Thresholds are set on these discriminators in order to stop electronic noise and any low energy background present from being accepted. These hardware thresholds must also be set low enough so as to accept events of interest. The thresholds values can be obtained from spectra of QDC's collected with the condition that their associated TDC returns a value other than zero. A typical plot is shown in figure (3.2). Note this shows both the pedestal and the threshold values. These threshold values are also required in order to make discriminator walk corrections.

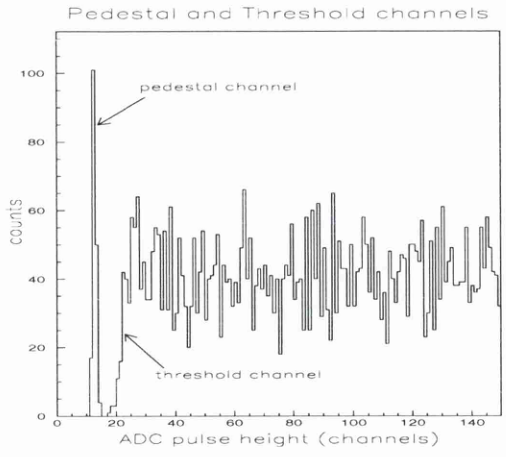


Figure 3.2: *Pedestal channel and discriminator threshold.*

## 3.3 Replacement QDC's

Some events in PiP, particularly events occurring near one end of a scintillator block, can produce such large pulse heights that they overflow the QDC at that end. Normally these events would be lost, but it is possible to recover them by making an estimation of their pulse height and 'replacing' the lost value [48]. This is achieved by using the fact that the ratio of charge in the QDC's at the two ends of a block has a linear dependence on position. Therefore parameters can be calculated which allow the missing charge information to be estimated knowing the position of a hit and the charge at the other end of the block.

## 3.4 Walk Corrections

In both the PiP and TOF detector systems leading edge discriminators are used rather than constant fraction units. These have the advantages of both a cheaper price and also of having a higher channel density, but unfortunately they also exhibit a small pulse height dependence in the timing of the output pulse. However this 'walk' can be corrected for. This effect is shown in figure (3.3). In these

discriminators the timing depends on when the pulse reaches a preset level. As can be seen large pulses will reach that level before small ones even though they both arrived at the same time. To correct for this we use the following formula [49].

$$t' = t + r\left(1 - \sqrt{\frac{a_0}{a}}\right) \tag{3.2}$$

Where $a_o$ is the discriminator threshold, a is the pulse height amplitude, r is the time taken for for a pulse to go from 10% to 90% of its height, t is the measured output time and $t'$ is the corrected time. Different methods were employed to find the rise times for various parts of the detector systems and they are outlined in the following sections.

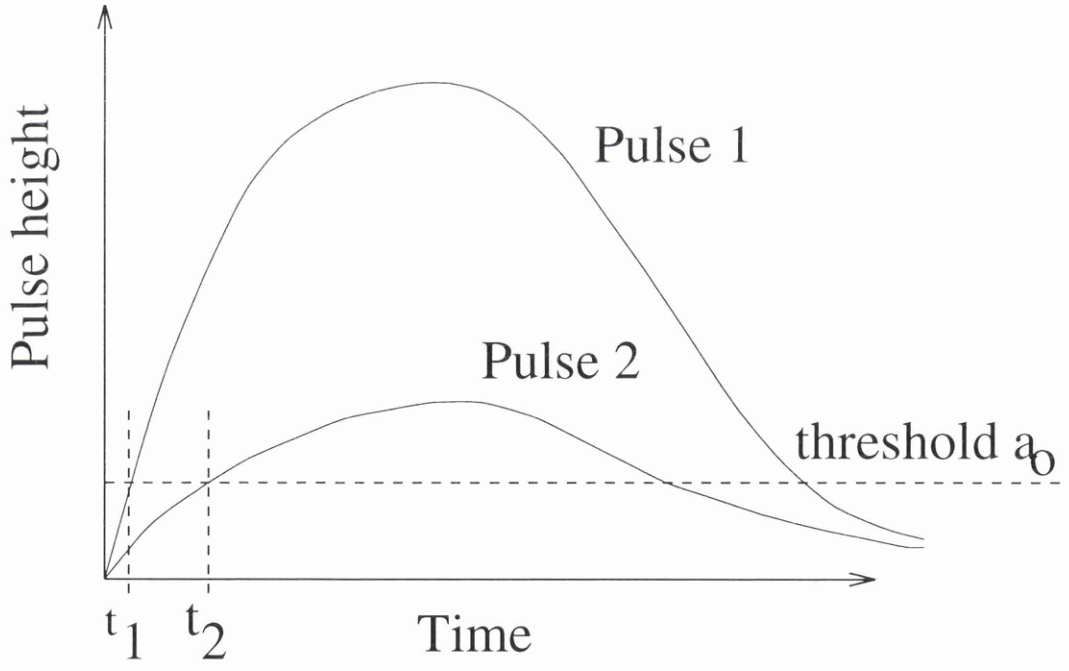


Figure 3.3: *Discriminator walk*

## 3.5 The Start Detector

The start detector (A-layer), is a half ring of seven thin plastic scintillators placed close to the target on the PiP side. The main purpose of the start detector is to provide a timing signal at a fixed time relative to the reaction in the target. The timing of the A-layer signal however depends upon discriminator walk in the start detector, the flight time of a particle from the target and the alignment of the various sections of the A-layer. These are all included in the following corrections to the start time, $\Delta t_{start}$:

$$\Delta t_{start} = \Delta t_{walk} + \Delta t_{flight} + \Delta t_{align} \tag{3.3}$$

this then allows the reaction time, $t_{reaction}$, to be calculated:

$$t_{reaction} = t_{start} - \Delta t_{start} \tag{3.4}$$

The walk in the start detector can be corrected for by calculating the rise time for each element in the experimental trigger. This is done by making use of the tagger, which uses dual threshold discriminators. These types of discriminators have negligible walk. Having made a first order energy calibration (see Section 3.7.5), protons are then selected in PiP and then a scatter plot is made of their pulse height vs one of the tagger TDC's, which are all started by the A-layer detector. The TDC channel value depends upon the transit time of the photon from the radiator to the target and also on the time the residual electron takes to travel to the focal plane of the Tagger. These times can be assumed to be constant since those particles are relativistic. The term $\Delta t_{flight}$ calculated using a first order energy calibration for protons, is included. The term $\Delta t_{align}$ takes account of any misalignment in the timing of each A-layer element. To find these values one plots a single Tagger TDC for each element under the condition that it is the only element giving a signal. This allows all the offsets to be calculated.

In order to estimate the walk in each A-layer element, the rise times are adjusted until the plots show a ridge that is as straight as possible. Figure (3.4) shows the result before and after the start corrections have been made.

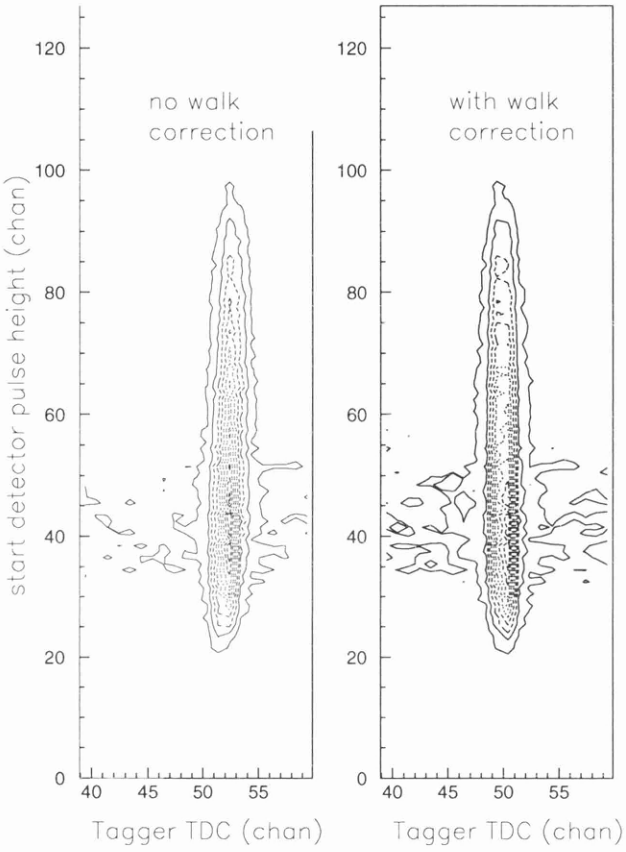


Figure 3.4: *A-Layer rise time corrections*

## 3.6 The Tagger

The purpose of the tagger is to measure the energy and timing of the residual electrons produced in the bremsstrahlung process. The energy of this residual electron is calculated from its hit position along the focal plane of the spectrometer. The trajectory of the electron is determined by the magnetic field inside the tagger and this was mapped with great accuracy using an NMR probe [42].

Knowing the initial beam energy, $E_0$ and measuring the energy of the residual electron $E_e$, allows the energy of the resultant photon $E_\gamma$ to be calculated. It is simply $E_0$ - $E_e$. Figure (3.5) shows a tagger timing spectra. The sharp peak is due to a coincidence between an event in PiP and a residual electron in the focal plane of the tagger. The flat background is due to non-coincident electrons. This coincidence peak is made sharper by applying the walk corrections to the A-layer as previously described.

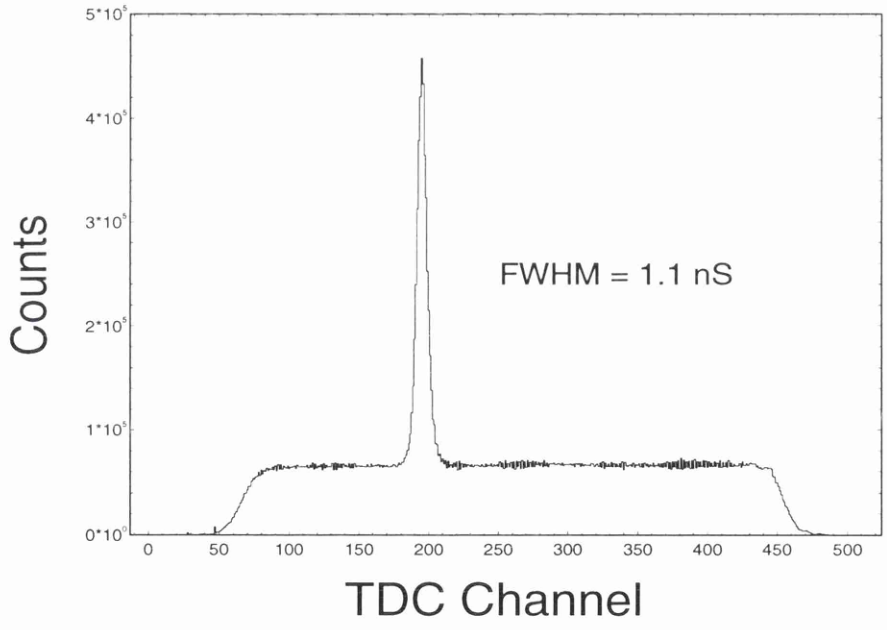


Figure 3.5: *Tagger timing spectrum*

## 3.7 PiP

In the present experiment PiP is used to detect protons. The techniques used to calibrate this detector are outlined below in the following sub-sections.

### 3.7.1 Position Calibration

As described earlier, PiP is a large segmented hodoscope. Being constructed from long scintillator blocks it is therefore possible to derive position information from the time difference between signals from either end of a block. If the position is $x$ then the time difference of the 2 TDC signals from a block is:

$$TDC_1 \; - \; TDC_2 \; = \; \frac{2x - l}{v} \; + \; k \tag{3.5}$$

Where l is the length of the block, v is the velocity of light along the block and $k$ is a sum of constant terms which represent the difference between the light propagation time, particle flight times and cable delays. So,

$$x \; = \; m(TDC_1 - TDC_2) \; - \; C \tag{3.6}$$

With $m$ and $C$ being calibration parameters.

In order to calibrate the position of each block in a layer one makes use of time difference spectra. Time difference spectra are accumulated for each layer (C-E) with the condition of a coinciding hit in the particular segment of B-layer. The individual spectra of the four B-layer segments are then superimposed together allowing the vertical joins in B-layer to be seen. These positions were accurately measured. Three calibration points are then obtained and these are then used to fit a line, the slope of which is the calibration parameter $m$ from above. Figure (3.6) shows a plot of time difference spectra for one of the blocks in C layer and figure (3.7) shows their intersection points plotted as a function of position. For

B-layer the inverse of the above procedure is applied. The time difference spectra in this case show the joins in the C-layer blocks.

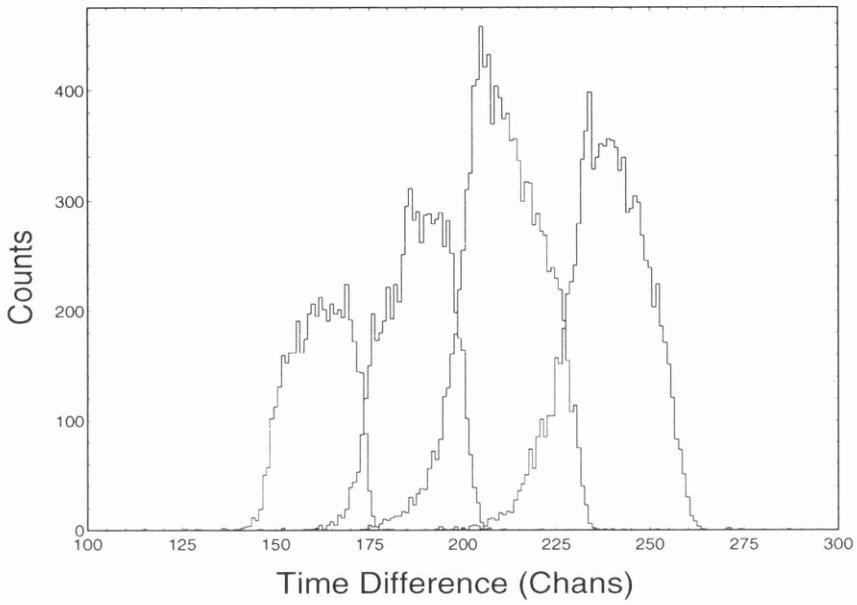


Figure 3.6: *Position calibration*

### 3.7.2 Gain Matching and Monitoring

In order to use PiP effectively each of the blocks in the individual layers should be matched so that their pulse height responses are the same. Each photomultiplier must also be checked to ensure that its gain does not change over time and if it does it must be corrected for. In order to do this the properties of both cosmic ray muons and the LED flashers were used[50].

Firstly the gains are matched. For each block within the individual layers this is done using cosmic muons. Calibration runs were made collecting cosmic data

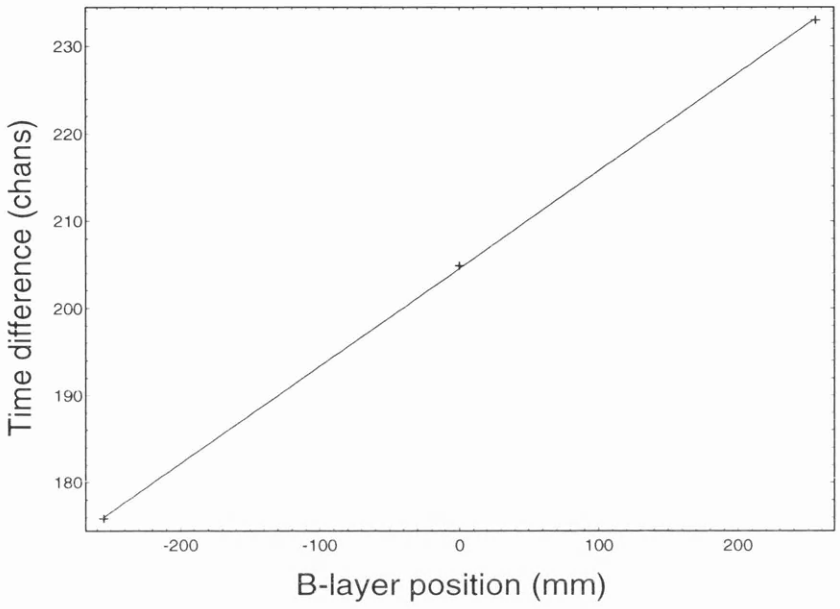


Figure 3.7: *Position calibration*

and these are used here. Cosmic muons are all travelling ultra-relativistically and they deposit a constant average amount of energy per unit thickness of plastic scintillator. This provides a ready source of stable calibration data. PiP is equipped with a cosmic trigger which demands both a hit in the top and bottom blocks of each layer. These events were selected and the following further requirements were also made to ensure the cosmics selected were travelling almost vertically. Using the time difference information a central region 20cm wide was defined in each layer vertically through all the blocks. Corrections were then made for the remaining variation in path lengths within that region and then spectra of the geometric mean of pulse heights was collected. Their spectra show a Landau distribution and fitting routines were then used to match the gains of

the blocks both within each layer and between the C, D and E-layers.

Once the gains were matched their stability over time was monitored using the LED flashers. Ultra bright LED's of 4 candela intensity are connected via plastic fibres to the two lightguides at the end of each scintillator. The light output of these LED's is checked by temperature stable PIN Diodes. The stability of the flashers has been well proven and therefore provides a stable source with which to monitor the gains of the Photomultiplier tubes. The data for this experiment were collected over a period of three weeks and so that time base was divided into a number of periods. Data taken over the periods were checked to see if there was any gain drift over time in the C, D and E layers. Overall it was found that all but two of the gains drifted by less than 2% with those two drifting by less than 4%. It was therefore decided that this gain drift was acceptable and no corrections were made.

### 3.7.3 Rise Times

The properties of the LED flashers can also be used to calculate the rise times of the leading edge discriminators used in PiP. The calibration parameters described previously were extracted [51], by making use of the fact that LED pulses are of a well defined shape and height.

### 3.7.4 Droop Alignment

As light attenuates along a scintillator bar that attenuation is, to first order, exponential and defined thus:

$$Charge \propto L\, exp^{-\left(\frac{x}{c}\right)} \tag{3.7}$$

where $L$ is the light deposited, $x$ is the position along the bar and $c$ is the attenuation length. However there is a residual droop in the geometric mean

of pulse heights from the two ends of a bar and this may be calculated and corrected for by fitting a parabolic function. In order to measure the droop one can again make use of the segmented design of PiP. Within each layer the top and bottom blocks were divided into ten equal regions using the time difference signals. Each region was then subdivided in half. Cosmic rays passing through the same region in the top and bottom blocks in each layer were selected, again correcting for any angular deviation from the vertical. Pulse height spectra from cosmics for these 10 regions was then collected. Figure (3.8) shows a plot of mean pulse height vs position for a typical C-layer block to which a parabolic function is fitted. For B-layer a different technique was employed as cosmics could not be

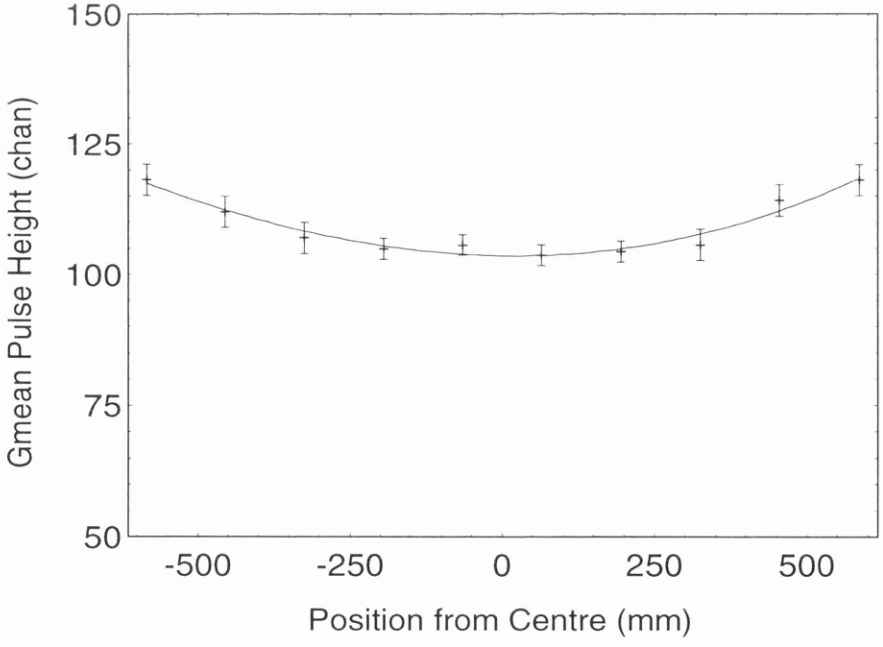


Figure 3.8: *Droop Corrections*

used. Again ten different positions along the bars were selected from the time

difference information, but here protons of a fixed energy (40-50 MeV) coming from the target were used. These were selected using pulse height signals in the following C-layer. Here a correction had to be made due to the effects of the different path lengths of particles NOT stopping in B-layer. Again a parabolic function was fitted to obtain the droop parameters.

### 3.7.5 Energy Calibrations

The energy calibration in PiP was done using the two-body breakup of deuterium, d($\vec{\gamma}$,pn), using data collected with a $CD_2$ target. The photon energy is measured in the tagger, the proton angle can be measured using the position calibration of PiP and there is no recoil nucleus. Hence the proton energy for each event can be calculated using the two body kinematics for the $\gamma$d $\rightarrow$ pn reaction. The purpose of the energy calibration is to obtain the conversion factor between the PMT output signals from PiP and particle energy. In the present experiment protons emerge from the target and travel through the air towards PiP. They then enter the scintillators, first passing through the wrappings surrounding them. All this time they are losing energy and these energy losses must be accounted for. For any medium through which a particle passes the range, $R$, of that particle is given by [53]:-

$$R = aE^k \tag{3.8}$$

where $a$ and $k$ are parameters which depend on that medium. The energy lost by a proton passing through a medium is equal to the difference between its initial energy $E_1$ and its final energy $E_2$. Higher energy protons will have a greater range than low energy ones, so $E_2$ is related to $E_1$ by:-

$$E_2 = \left[E_1^k - \frac{\Delta R}{a}\right]^{\frac{1}{k}} \tag{3.9}$$

where $\Delta R$ is the thickness of material which produces an energy reduction from $E_1$ to $E_2$. These energy losses through various materials are tabulated in range tables and are calculated by the data analysis software. Once protons reach C-layer in PiP their calculated energy was plotted against their measured energy signal for all the protons which stop in that layer. This was repeated for protons which stop in the two layers behind, (D and E). This measured energy signal has been position matched, gain matched and droop corrected as described above. For the D and E layers, energy losses in the layers before them have also been accounted for. For each of these layers the plots give the necessary calibration parameters and within each layer the gains of individual blocks may be fine tuned if required. Figure (3.9) is a plot of measured proton energy signal vs calculated proton energy for the C-layer. The ridge visible is due to protons from the two body breakup of deuterium and the background is due to carbon in the $CD_2$ target.

## 3.8 TOF

In the present experiment TOF is used to detect neutrons. The techniques used to calibrate this detector are outlined below in the following sub-sections.

### 3.8.1 Position Calibration

The actual physical positions of each of the TOF bars was measured using an ultrasonic measuring device and those details were recorded in a calibration file. This allows the polar and azimuthal angular range of each bar to be determined. For the TOF bars themselves, the vertical position of a hit allows the azimuthal angle to be determined. This vertical position calibration is determined from spectra which record the time difference of a hit as measured by the two ends of

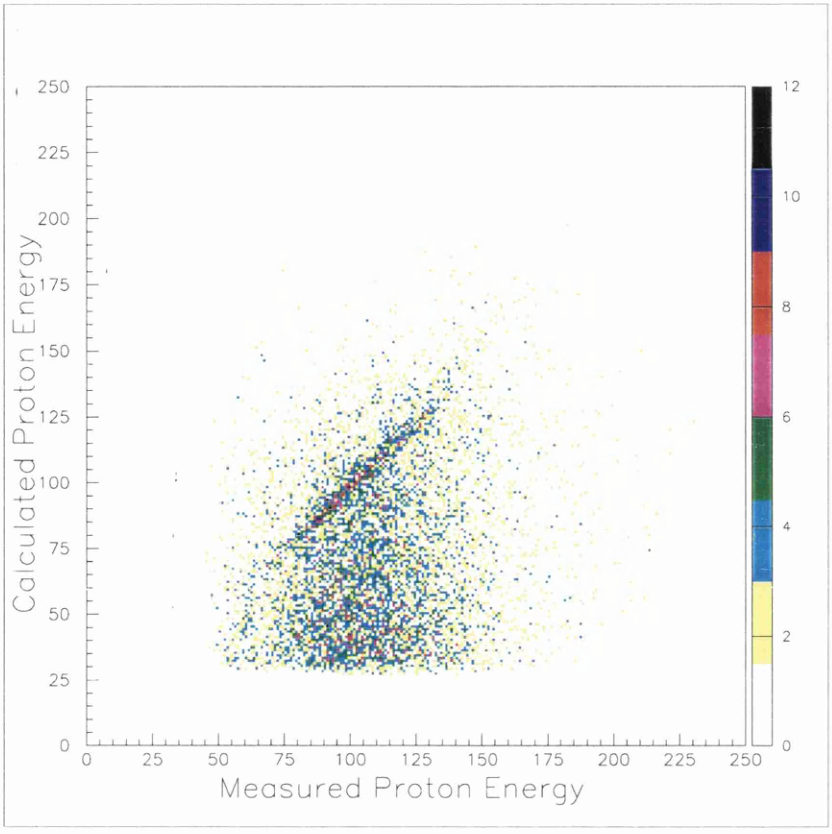


Figure 3.9: *Calculated vs Measured proton Energy*

a bar. Figure (3.10) is such a plot for one of the TOF stands. The width of the distribution represents the length of a TOF bar.

### 3.8.2 Gain Monitoring

The gains of the TOF bars were monitored in the same way as in PiP, that is by using the LED flashers. Here eight time periods were selected and the peak channel from the flasher was recorded for each bar. Over the total period it was found that all but two bars drifted by less than 3%. Of those two one drifted by 4% and the other by 6%. As in PiP it was decided that no corrections for gain drift would be applied. The LED flashers were also used to obtain the rise times in TOF, using the same method as for PiP.

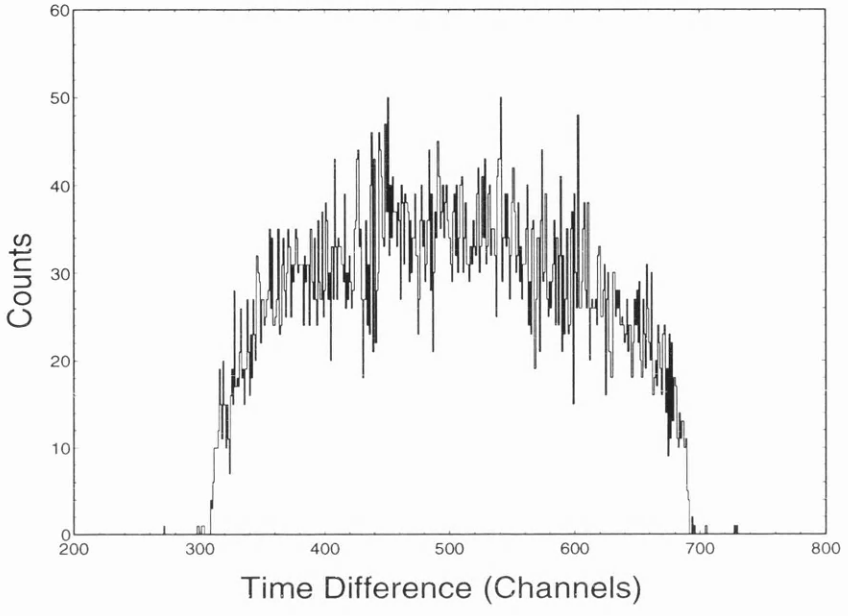


Figure 3.10: *TOF Position Calibration*

### 3.8.3 Pulse Height Calibrations

The energy information from TOF is taken from time of flight measurements but a pulse height calibration is necessary in order to determine the detection efficiency. It also serves to match the gains. Two calibration points were obtained for each bar, one using an AmBe source and the other from protons coming from the target in the experimental data. The decay of AmBe includes alpha absorption which produces $^{12}C$ in an excited state. This then decays to the ground state emitting a 4.4 MeV photon. The bars which make up the TOF stands are 5cm thick, which is the range of a 78 MeV proton. The energy loss of protons travelling perpendicular to a bar will rise to a maximum for 78 MeV protons and then fall

off for higher energy protons which no longer stop in the bar. Spectra which show a geometric mean pulse height vs time of flight for each bar [52] were examined and the peak pulse height for protons was noted. These two data points are extrapolated in order to provide the necessary calibration values.

### 3.8.4 Time of Flight Calibration

In TOF the energy of the detected neutrons is determined from time-of-flight measurements. These times are obtained from the mean time recorded by the TOF TDC's less the start time and a constant:

$$Time\ of\ Flight\ =\ t_{mean}\ -\ (t_{start}\ +\ constant) \tag{3.10}$$

where the $t_{start}$ is defined in Section 3.5. The constant is the time accounted for by cable delays. If we could define a time which accounts for the start time and the constants this would give us give us the correct time-of-flight and this we do by calling this the time zero.

$$t_{zero}\ =\ t_{start}\ +\ constant \tag{3.11}$$

this is the mean TDC time that would be recorded if the TOF stands were placed at the target. In order to measure $t_{zero}$ we use the many relativistic particles which are produced by atomic events in the target. These relativistic photons and electrons produce a so called 'gamma flash' and this is seen in mean TDC spectra. An example is shown in figure (3.11). For each TOF bar the channel corresponding to the gamma flash is recorded and this time is then subtracted to give a true time-of-flight, once corrections have been made for the finite flight time of the relativistic particles. This then allows the kinetic energy, $T$, of the

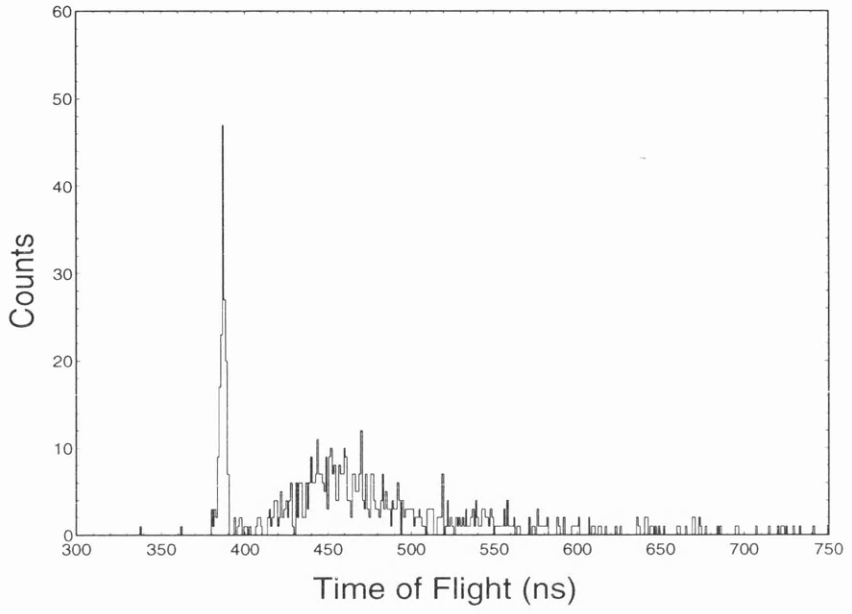


Figure 3.11: *TOF time-of-flight spectra*

detected particles to be obtained from the relativistic equation:

$$T = m\left(\frac{1}{\sqrt{1 - \frac{v^2}{c^2}}} - 1\right) \tag{3.12}$$

where $m$ is the rest mass of the particle detected and $v$ is just the distance flown divided by the time-of-flight.

## 3.9 Detector Performance

Having completed the calibrations the next step is to compare the performance of the detector systems with estimates and previous measurements. As stated previously the two body breakup of deuterium was used as the overdetermined

kinematics of that reaction allow a direct comparison between calculation and measurement.

### 3.9.1 Missing Energy

For photonuclear reactions such as this present one an important parameter is 'missing energy'. This is defined as:

$$E_m = E_\gamma - T_p - T_n - T_{recoil} \tag{3.13}$$

Where $E_\gamma$ is the energy of the incident photon, $T_p$ is the kinetic energy of the emitted proton, $T_n$ the kinetic energy of the neutron and $T_{recoil}$ is the kinetic energy of the recoiling (A–2) nucleus. For Deuterium there is no residual nucleus and therefore:

$$E_m = E_\gamma - T_p - T_n = -(M_d - M_p - M_n) = -Q \tag{3.14}$$

Where $M$ is the masses of the residual particles and $Q$ is the Q-value for the reaction and is equal to –2.2 MeV. Figure (3.12) shows a plot of missing energy for $CD_2$. The plots are for the two different orientations of polarisation and a difference is clearly visible. The sharp peak is at the expected missing energy of 2.2 MeV for deuterium events and is on a background of carbon and random events.

### 3.9.2 PiP Energy and Angular Resolution

From missing energy spectra one can make software cuts on the deuterium events. This much reduces the carbon background in the calculated vs measured energy plot for PiP, an example of this is shown in figure (3.13). This should be compared

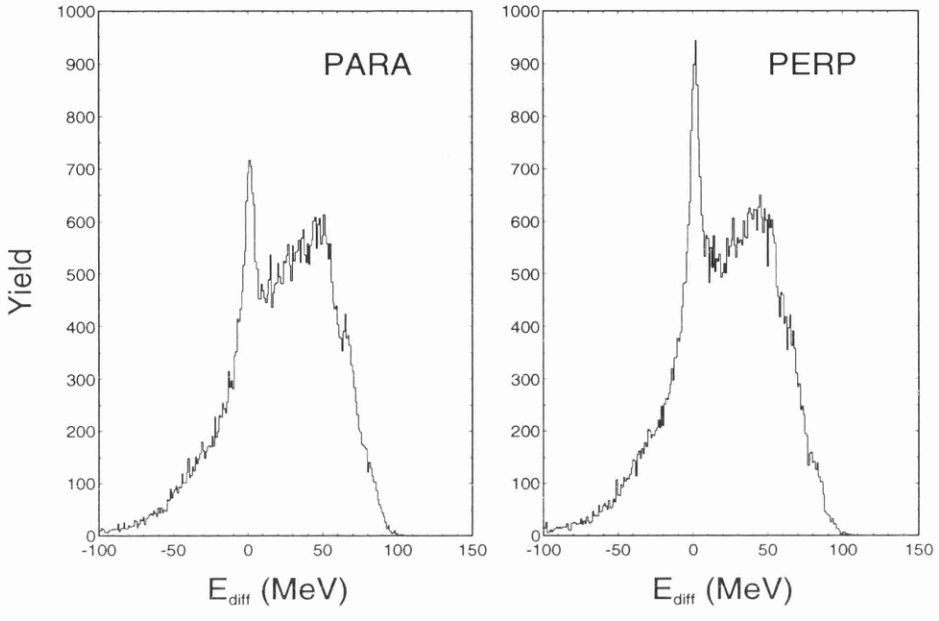


Figure 3.12: *$CD_2$ Missing Energy Spectra*

with figure (3.9) in which no selection of deuterium events was made. These plots can also be used to calculate energy resolution by making the software cuts around them. This again selects the energy difference and from this the energy resolution can be measured. In the experiment the photon energy is measured by the tagger with a resolution of $\sim$ 2 MeV and the neutron polar angle is measured in TOF with a resolution less than $3^o$. Thus the proton energy and angular resolution can be calculated. This method is used because it gives a better resolution in the selection of $T_p$ than by using $\Theta_p$. Figure (3.14) is a plot of the difference between measured and calculated energy for PiP. From this it is possible to measure the PiP energy resolution. The proton polar angle resolution $\Theta_p$ is calculated by using a measurement of the neutron polar angle $\Theta_n$, which is known to the

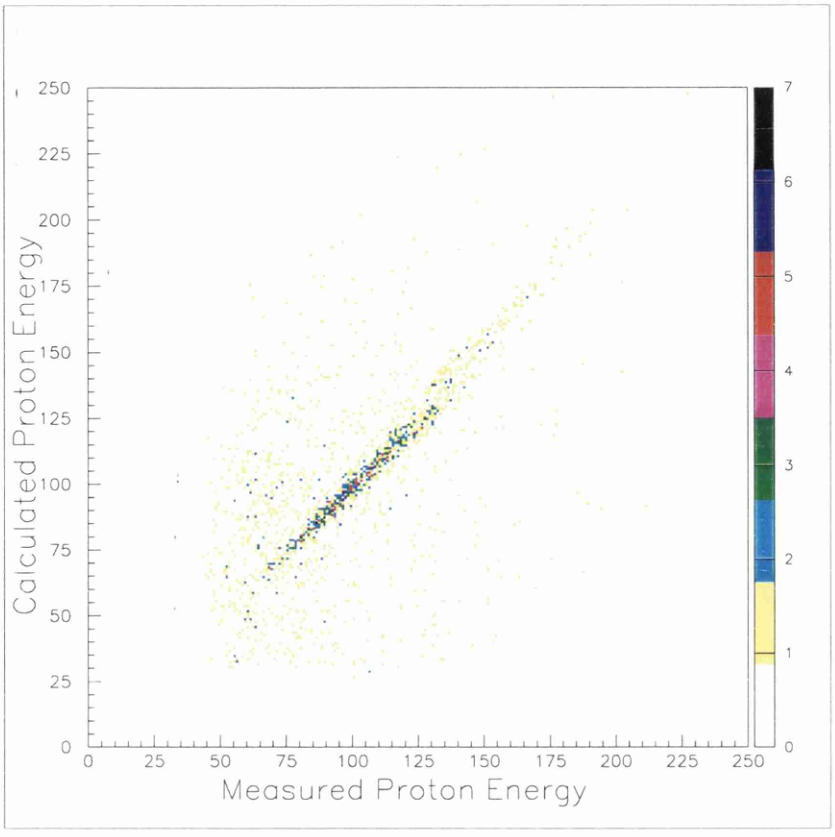


Figure 3.13: *Calculated vs Measured Proton Energy*

greatest accuracy and the photon energy. These calculations were made over a photon energy range of 40-400 MeV and the polar angular resolution was found to be 4°. This can also be checked by an estimate of the position resolution of C-layer and was found to be the same. The proton azimuthal angular resolution was calculated from the vertical position resolution in B-layer and was estimated to be $\sim 4.5°$.

### 3.9.3 TOF Energy and Angular Resolution

The energy resolution in TOF was obtained in a similar way to that for PiP by using the knowledge of neutron angle for each event to calculate the neutron energy. The energy difference between the measured and calculated neutron

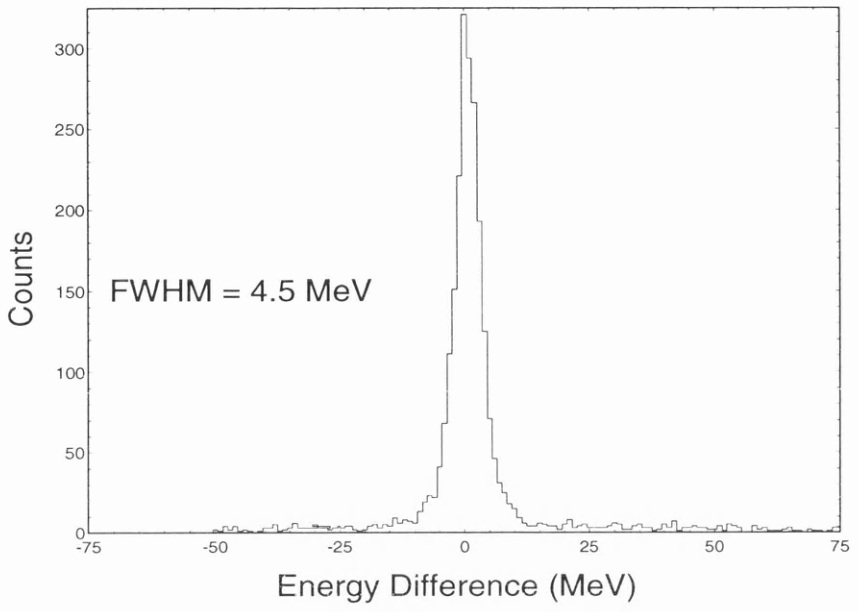


Figure 3.14: *PiP energy resolution*

energies was plotted and an example is shown in figure (3.15). Again this was over the photon energy range 40-400 MeV. The polar angular resolution is determined by the size of the TOF bars. These individual bars are 20cm wide and are placed between 4m and 7m from the target. This gives a polar angular resolution of between $1.6^o$ and $2.8^o$. The azimuthal angular resolution was estimated from the vertical position resolution of the bars and was estimated to be $\sim 1^o$.

### 3.9.4 Overall Performance

The calculated energy and angular resolutions above are not independent and are therefore do not give the intrinsic resolutions for the detector systems. For example in the deuterium breakup reaction the most accurately measured val-

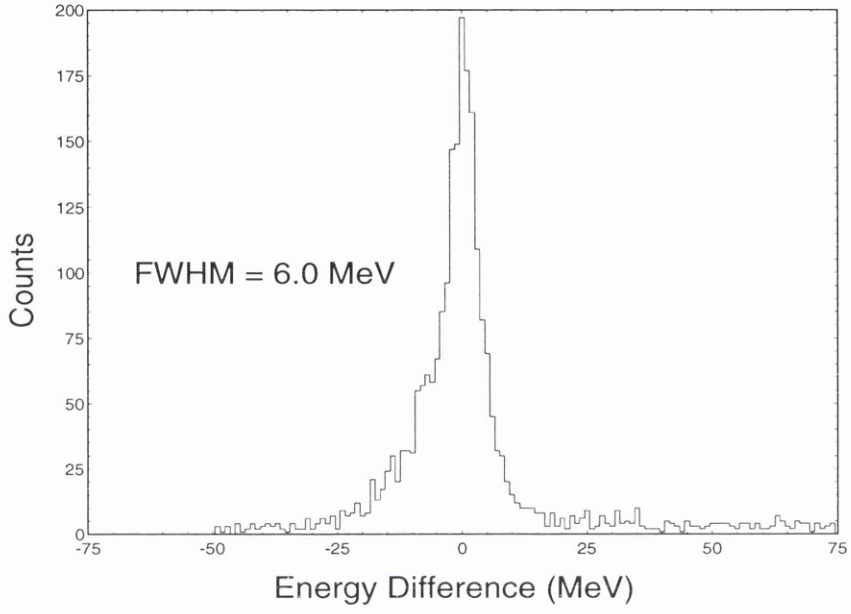


Figure 3.15: *TOF energy resolution*

ues are the neutron angle and photon energy and these values are then used to determine the kinematics for each event. These variables themselves include an associated uncertainty and therefore the angular and energy resolutions obtained are not the intrinsic values for the detectors. The effects of these uncertainties must therefore be unfolded in order to obtain the intrinsic resolutions. Table (3.1) is a summary of the performance of the detector systems and includes their intrinsic resolutions.

| Detector | Particle | Quantity | Acceptance | Resolution(FWHM) |
|---|---|---|---|---|
| Tagger | $\gamma$ | $E_\gamma$ | 40MeV→400MeV | 2MeV |
| PIP | proton | $E_p$ | 26MeV→300MeV | 4.5MeV |
| | | $\theta_p$ | $51° \rightarrow 129°$ | 4.0° |
| | | $\phi_p$ | $+23° \rightarrow -23°$ | 4.5° |
| TOF | neutron | $E_n$ | $\geq$ 17MeV | 5.8MeV |
| | | $\theta_n$ | $10° \rightarrow 175°$ | ~2.0° |
| | | $\phi_n$ | $160 - 172° \rightarrow 192 - 200°$ | ~1° |
| Combined | | $E_{miss}$ | - | 7.5MeV |

Table 3.1: *Summary of detector performance (intrinsic values)*

# Chapter 4

# Data Analysis

# Introduction

This chapter outlines the techniques used in analysing the asymmetry of the $^{12}C(\overrightarrow{\gamma},pn)$ reaction. Firstly the particles required were selected. Next the detector and tagging efficiencies were determined. Random and background events were subtracted and then the required kinematical selections were made. Once this was done it was possible to select on the appropriate regions of missing energy in the data. Next it is necessary to determine the beam polarisation and finally it was possible to determine the reaction cross sections and asymmetries. This chapter concludes with a discussion of the experimental uncertainties in this experiment.

## 4.1 PiP Proton Selection

In the present experiment PiP is used to select protons. The simplest method of selecting protons is to plot graphs of $\Delta E$ vs E. In these plots protons lie in a curved locus, an example of which is shown in figure (4.1). Proton selection requires a complicated and subjective cut, which could still include some particles which had suffered inelastic hadronic losses. The corrections for this effect were complicated and so a new method of selecting protons [54] was applied. This method involves determining the energy of protons and pions using two different techniques and the comparing the results. Firstly, assuming the particle is a proton, its energy is determined by examining the signal from the last detector layer in which the particle stops. The energy loss back to the target, including the previous PiP layers and the dead layers is then calculated using range tables. This gives an energy estimate value known as $E_{calc}$. Secondly the light output for all the PiP layers through which the particle passed is converted into energy and added up. Corrections are again made for the dead layers. This gives the

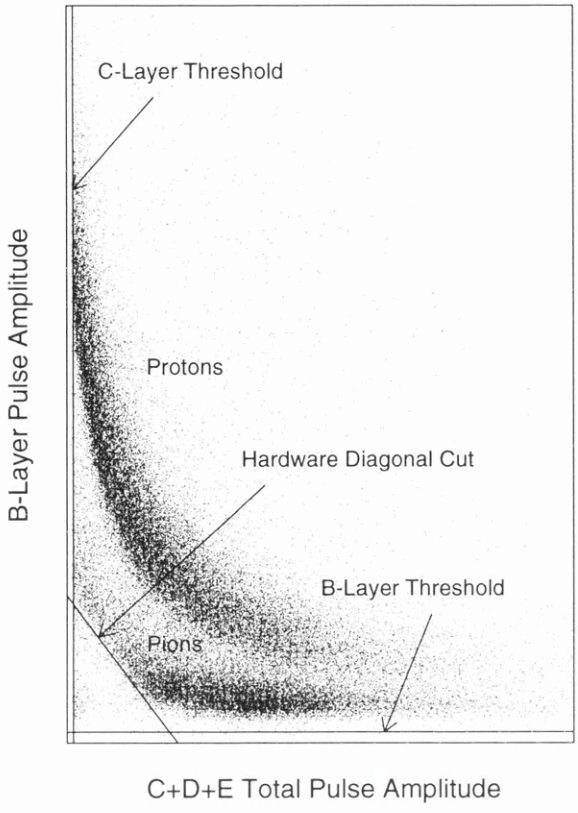


Figure 4.1: *Proton identification and Selection 1.*

second energy estimate known as $E_{meas}$. The process is then repeated assuming the particle was a pion. Now, particle identification is made by comparing the difference between these two quantities, $E_{diff}$, for each particle type and defined thus:

$$E_{diff.proton} = E_{calc.proton} - E_{meas.proton} \tag{4.1}$$

and

$$E_{diff.pion} = E_{calc.pion} - E_{meas.pion} \tag{4.2}$$

for protons, $E_{diff.proton}$ will be close to zero but $E_{diff.pion}$ will be greater than zero. If the particle is a pion then $E_{diff.pion}$ will be close to zero while $E_{diff.proton}$ will then be greater than zero. For the case of particles which have undergone inelastic

reactions then both of the quantities $E_{diff.proton}$ and $E_{diff.pion}$ are not close to zero. $E_{diff}$, is calculated for each particle type and plots are made of $-E_{diff}$ for a proton vs $E_{diff}$ for a pion. Such a plot is shown in figure (4.2) for particles stopping in the C-layer of PiP. As can be seen there are three distinct regions visible. Protons

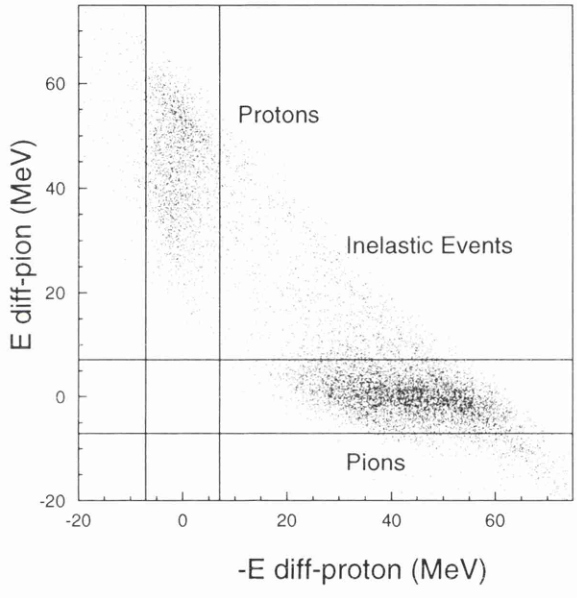


Figure 4.2: *Proton identification and Selection 2.*

are centered around a region where where $E_{diff}^{prot} \sim 0$ and pions where $E_{diff}^{pion} \sim 0$. The third region contains events which have undergone inelastic reactions in the scintillators. This then allows the unambiguous selection of protons for this present experiment. This method is precise and easily reproducible. As can be seen from figure (4.2) the size of the cuts may be varied but for this present work $E_{diff.proton}$ was $\sim 0 \pm 7$ MeV.

## 4.2 TOF Neutron Selection

Neutrons are selected in TOF by using the properties of the G and H-layer delta detectors, which can be used to 'veto' particle types. These detectors are very thin in nature and so uncharged particles should pass through without making a signal in either layer. Particles are classed as uncharged if they make no signal in either the G or H layer while events are classed as charged if they produce at least one signal. Events which produce two or more particles in TOF may be selected, but were rejected in this present analysis.

Neutrons are further selected by making software cuts on TOF time-of-flight spectra as shown in figure (4.3). The 'gamma flash' due to photons produced in

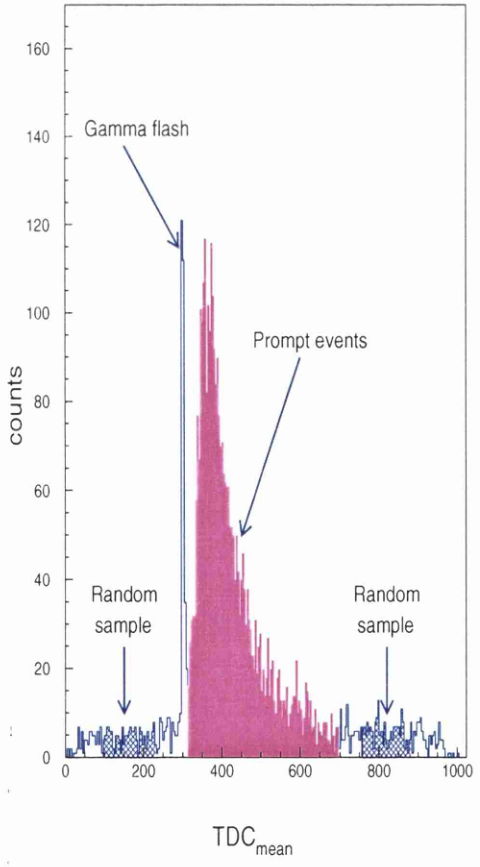


Figure 4.3: *TOF Time-of-Flight Spectra*

atomic scattering near the target can be seen as a sharp peak. Some electrons also contribute to the gamma flash peak because they produce low pulse heights in the G and H-layer detectors and do not register a signal in the QDC's. These events are then rejected by making cuts on individual TOF bar spectra. The minimum time-of-flight limit is kept quite tight so as to include high energy neutrons and the maximum time-of-flight limit is set at the point where the number of events does not exceed the random background. The accepted events are shown by the prompt event region in figure (4.3). Any random events getting through will be subtracted at a later stage.

Although the delta detectors are segmented in nature there is not necessarily a direct correlation between events in a G or H-layer element and a signal in a TOF bar directly behind as some scattering of particles may take place in the delta detectors. The TOF bars covered by the G and-H layer elements were determined by selecting individual TOF stands and examining spectra of G and H-layer hit patterns.

As previously discussed the TOF stands were arranged two deep in order to increase detection efficiency. Neutrons are detected via secondary reactions such as proton knockout and a Monte Carlo simulation [55] showed that a significant number of neutron events producing a proton which causes a signal in the front stand, then travel on to produce a signal in the stand behind. These events can be identified by tracking each uncharged event through TOF. If a hit in a bar in a front stand results in a hit in a bar either directly behind, or behind and one bar displaced to the left or right, then the hit in the rear bar is assumed to have come from a scattered particle. The timing information from such a hit is ignored but the pulse height information is kept in order to improve resolution and particle selection.

## 4.3 Detector Efficiencies

### 4.3.1 Tagging Efficiency

Tagging efficiency gives a measure of the number of photons which have been removed by the collimators. The method of measuring this efficiency was previously discussed in section 2.2.5. Separate tagging efficiency runs were made for the three photon energies at which this experiment was conducted. Figure (4.4) shows plots of tagging efficiency for those three energies (220, 270 & 280 MeV) together with a plot of an unpolarised run made using the nickel radiator which produces incoherent radiation. From the plots made using the diamond radiator one can clearly see the coherent peaks and edges corresponding to polarised photons produced by the various reciprocal lattice vectors in the diamond crystal. The main feature in each plot is due to the [0 2 $\bar{2}$] reciprocal lattice vector. Coherent bremsstrahlung has a narrower angular distribution than incoherent bremsstrahlung resulting in a higher tagging efficiency in the polarised region. Outside the polarised region the slight rise in tagging efficiency with photon energy is due to the decreasing divergence of the incoherent photons. This results in less photons being removed by the collimators. These data sets were later used in the calculations of cross sections. For most of the tagging efficiency runs the data were collected whilst switching the polarisation direction between parallel and perpendicular. However some runs were made with this direction fixed in order to compare the tagging efficiency at these two orientations. Figure (4.5) shows a plot made from two such runs at 350 MeV. As can be seen there was no significant difference seen between the two orientations and so the same value of tagging efficiency was applied for both the parallel and perpendicular orientations and in the final analysis these values are applied on an event by event basis.

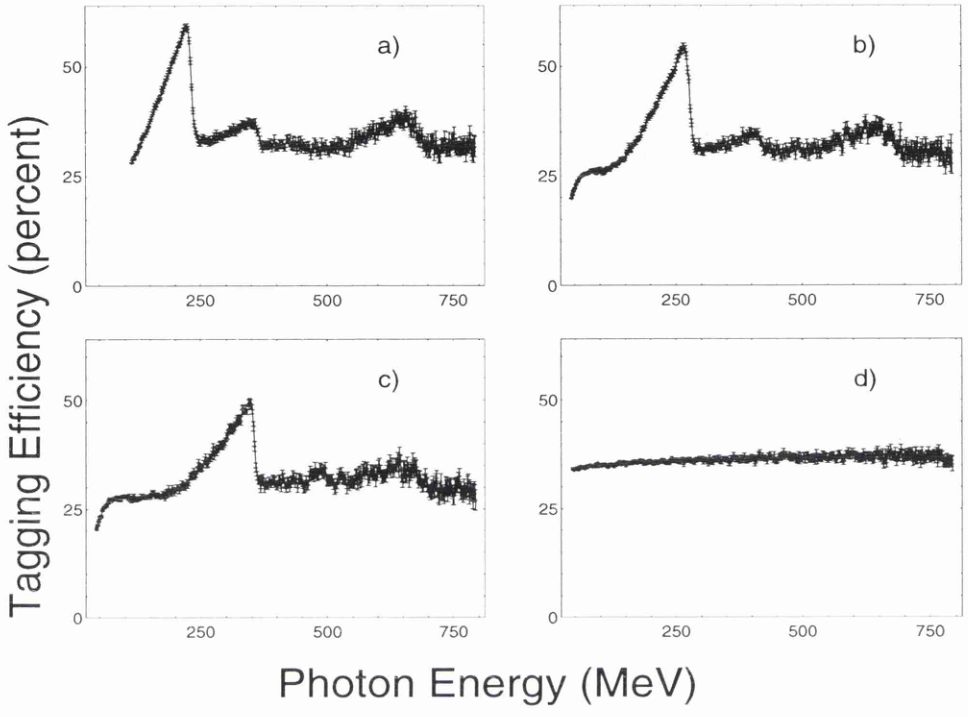


Figure 4.4: *Tagging Efficiency Runs. a)$E_\gamma$=220 MeV b)$E_\gamma$=270MeV c)$E_\gamma$=350 MeV d)Unpolarised*

### 4.3.2 Neutron Efficiency

Neutrons are detected in TOF via secondary processes such as proton knockout and other scattering reactions. A threshold of 9 MeV is applied and events producing a pulse height above that level are accepted and analysed. The efficiency of the TOF detectors was determined using the Monte Carlo code STANTON [53] which models the interaction probabilities of incident and scattered neutrons. Figure (4.6) shows a plot of predicted neutron efficiency for neutrons incident on a single TOF bar. However as stated this code calculates efficiencies for a single TOF bar but in this present experiment the TOF bars were arranged on stands

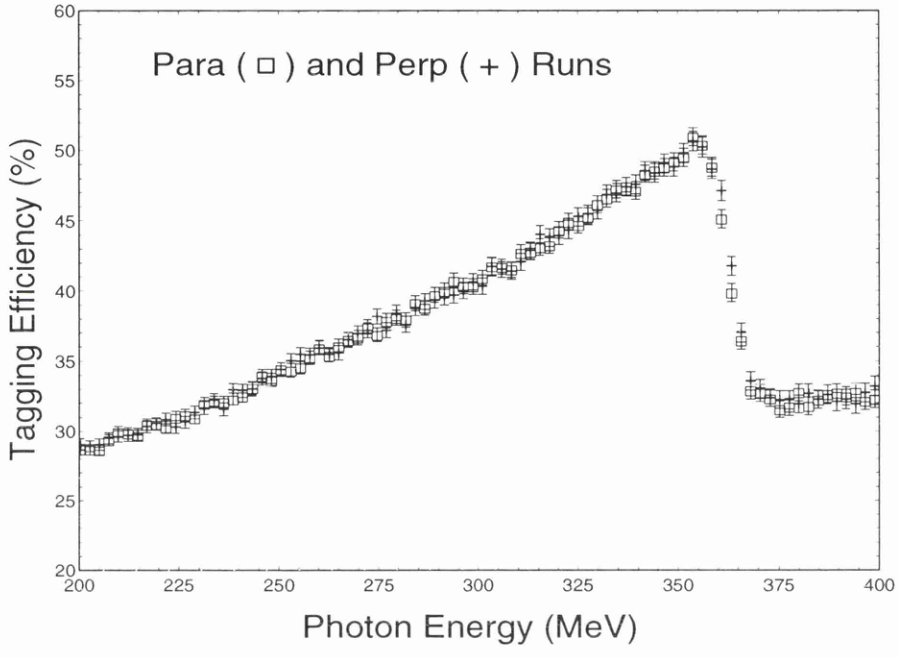


Figure 4.5: *Tagging Efficiency for Para and Perp Orientations, $E_\gamma$ = 350 MeV*

two deep. Therefore the following corrections must be taken into account. Firstly a corrected efficiency, $\epsilon_{NeutCorr}$, for the second layer is obtained from the efficiency of a single bar, $\epsilon_{Bar}$, by the following relationship:-

$$\epsilon_{NeutCorr} = \epsilon_{Bar} + \epsilon_{Bar}(1 - \epsilon_{Bar}) \tag{4.3}$$

Secondly the code assumes that neutrons are incident perpendicular onto the TOF bars and so a correction of $\frac{1}{sin\theta}$ must be made for the angle of incidence, where $\theta$ is the angle of incidence to the normal. Finally the fact that one stand is behind another means that the solid angle subtended by that detector is slightly less than the one in front. This is taken into account in the calculation of the

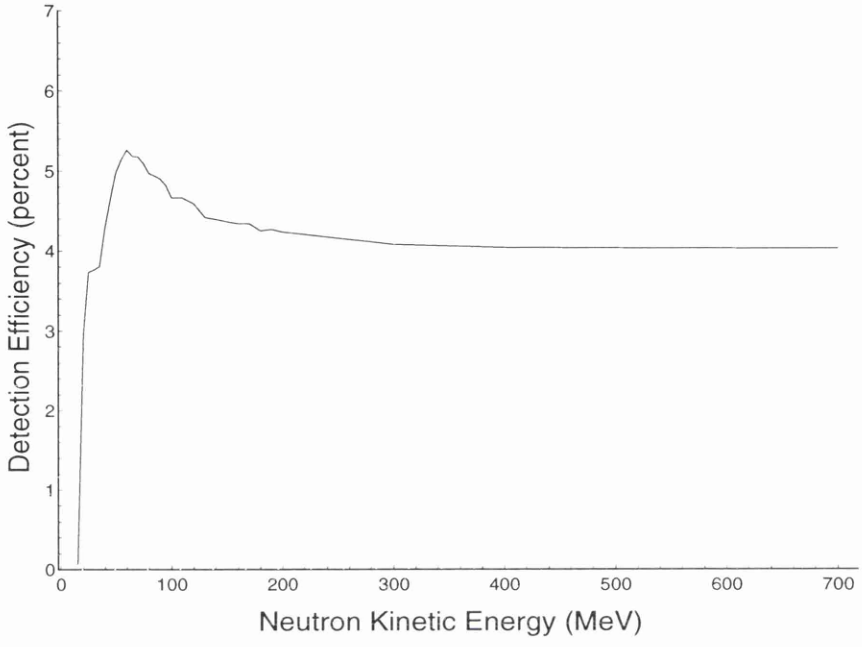


Figure 4.6: *Neutron Efficiency as modelled by STANTON*

cross sections.

## 4.4 Dead Bar Corrections

In the present experiment it was found that there were 4 bars in TOF which were faulty. Corrections were made to the yields from these bars in the calculations of cross sections. These corrections were made by making careful estimates of the missing yields, taking into consideration the yields found in adjacent bars.

## 4.5 Random Subtraction

Random events are defined as events in any of the detector systems which are caused by particles entering the detectors that are not correlated with other detected particles, and therefore are distinguished as a flat background on TDC spectra. The majority of data from this present experiment required coincidences between the tagger, PiP and TOF and this has the effect of reducing the background to a manageable rate. However random particles are detected and therefore these events must be be accounted for and subtracted from the final data. The method used to deal with these randoms was to assign a statistical weight to each event. These weights can be either positive or negative depending on whether they are located in the prompt or the random region of time spectra and in the final analysis the weight of each event is included, resulting in spectra which have a subtracted random background.

### 4.5.1 Tagger Randoms

Figure (4.7) shows a tagger timing spectrum containing the prompt and three random regions. The prompt region corresponds to events correlated with a photoreaction and this peak sits on top of a background of random events. These random events are subtracted by means of statistical weights. Events occurring in the prompt region are assigned a weighted value of 1 while events occurring in the random regions are assigned a negative weight, $W^{tagger}_{random}$, determined by the total width of the random regions:-

$$W^{tagger}_{random} = \frac{-1.0 \times \Delta T_{prompt}}{\Delta T_{region1} + \Delta T_{region2} + \Delta T_{region3}} \tag{4.4}$$

This weighting ensures that a correction is made for the random events.

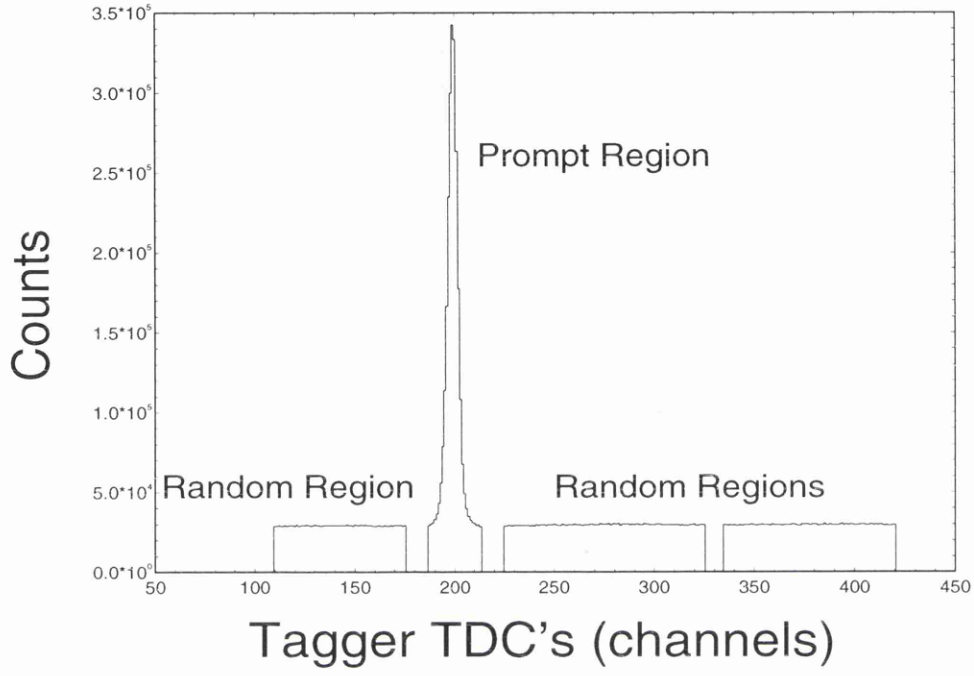


Figure 4.7: *Tagger Prompt and Random Regions*

### 4.5.2 TOF Randoms

Random events are also present in TOF spectra and again prompt and random regions are defined and these can be seen in Figure (4.3). In the TOF case the reverse of the tagger case is true and the random regions are smaller than the prompt region. The method of using weights corrects for this effect, but care has to be taken to map the energy range covered by the random region onto the energy range covered by the prompt region [56].

## 4.6 Background Subtraction

A small fraction of events detected will not come from photoreactions within the target but from reactions taking place in nuclei in the air around the target traversed by the photon beam. In order to correct for this separate runs were made with the target taken out. These data were analysed in exactly the same way as the 'target in' data and spectra can be made. Figure (4.8) shows a missing energy plot from a $^{12}C$ target which includes a contribution from background, overlayed with a missing energy spectrum from a target out run which has been normalised in order to account for the different number of tagged photons. In this way the background can be subtracted in order to obtain corrected missing energy spectra. On average it was found that the contribution from the background amounted to $\sim$3% of the yield although this did change slightly with proton polar angle.

## 4.7 Kinematical Selection

In order to compare data from the present experiment with data from previous experiments and also with theory for direct 2N emission it was necessary to select quasideuteron kinematics (QD kinematics). This is achieved by making selections in both the azimuthal and polar planes. In the azimuthal plane, or the $\phi$ case, the restriction was made on the difference between the angle of the proton and the neutron, while in the polar plane, or the $\theta$ case, the restriction was made on the difference between the angles of the *pn* pair and the $\theta$ angle of a quasideuteron pair. For the present experiment an angle of $\pm 20^{o}$ was chosen. Figure (4.9) shows the effect on missing energy spectra of making these selections. The choice of angle is a compromise between selecting the required kinematics and not reducing the experimental yield so far as to adversely effect the statistical

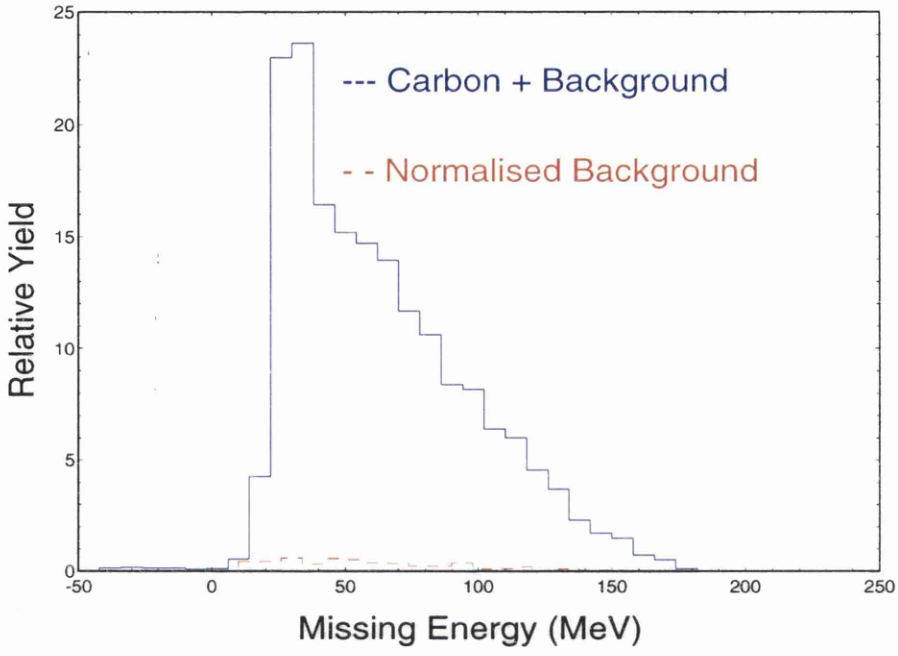


Figure 4.8: *Background Subtraction from Missing Energy Spectra*

accuracy. The angle chosen reduced the yield by $\sim 40\%$.

As well as selecting QD kinematics it was decided to restrict the azimuthal angular range of the *pn* pair. Events in which the *p*-*n* plane makes a non-zero angle with the photon polarisation plane will reduce the measured asymmetry. It was decided to restrict the angular range to such that the effect on the value of asymmetry would be small. The effect of non-zero azimuthal angles is shown in Appendix A. The restriction was achieved by defining an effective azimuthal plane which is an average of the proton and neutron azimuthal angle. The range of this effective plane was restricted to $\pm 13.5^{o}$. This range has the effect of further reducing the experimental yield by $\sim 7\%$.

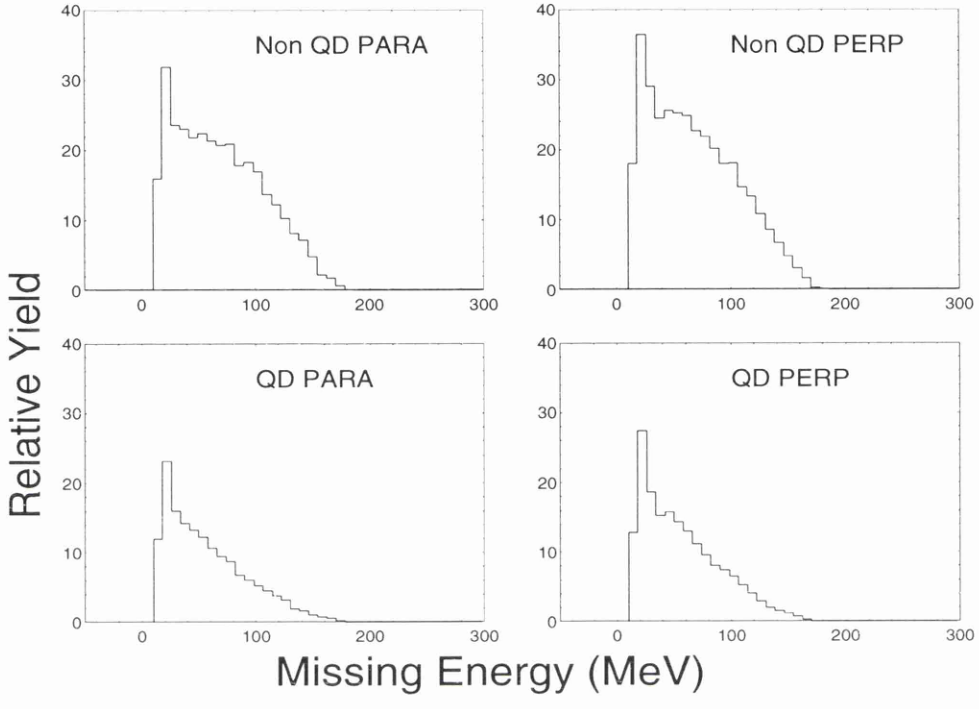


Figure 4.9: *Selection of QD Kinematics*

## 4.8 Selection of Photon Energy Regions

The data for this experiment were taken with the maximum beam polarisation at three separate photon energies; 220, 270 & 350 MeV. However within each measured energy region there is a significant range in which linearly polarised photons are produced by the primary reciprocal lattice vector. Figure (4.10) shows a plot of polarisation vs photon energy. As can be seen from the plot, for each separate energy setup four photon energy regions of width 20 MeV were selected where the average polarisation was ~25% or more. Outside these regions the polarisation was judged too small to obtain accurate results.

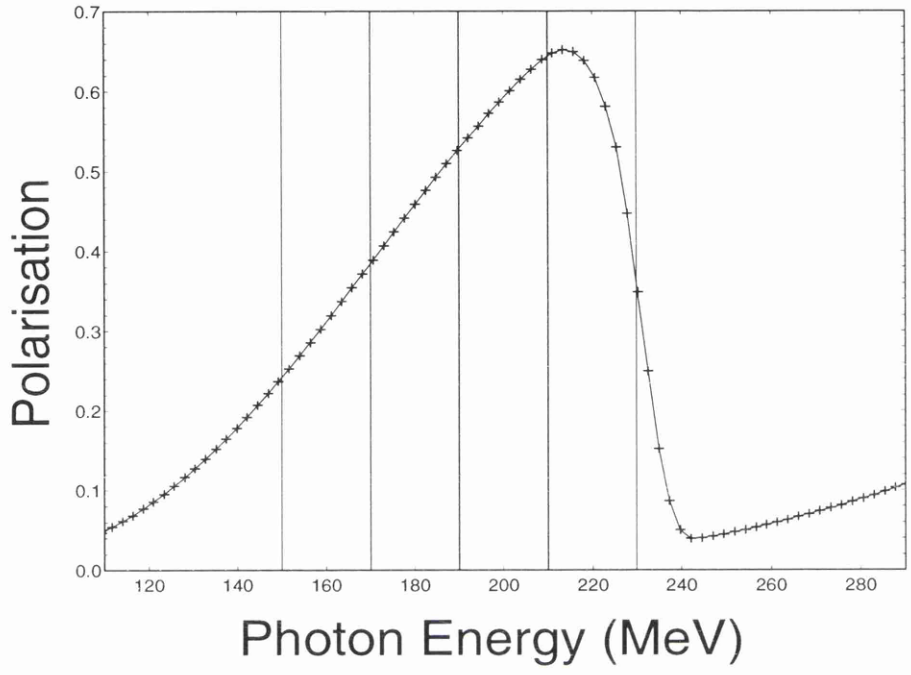


Figure 4.10: *Selection of Photon Energy Regions*

## 4.9 Determination of Polarisation

In order to make a calculation of the degree of linear polarisation obtained during the experiment a theoretical code, developed in Göttingen [39], was used. This code calculates the absolute and relative intensities of both incoherent and coherent bremsstrahlung produced by crystal lattices. This is done via an analytical calculation which takes into account the distributions of the angle and position of the incident electrons. The code then generates bremsstrahlung scattering, taking into account multiple scattering within the lattice. It then generates photons and, having calculated the intensity of those photons, calculates the polarisation.

The spectrum is a coherent sum of contributions from many reciprocal lattice vectors. All that is required to run the programme are the crystal angles $\alpha$ and $\theta$ and these are the angles which were set on the goniometer during the experiment; along with details such as beam energy, divergence, temperature and diamond thickness. Figure (4.11) shows the calculated polarisation for one such setting. Having calculated the degree of polarisation one can see how it compares with

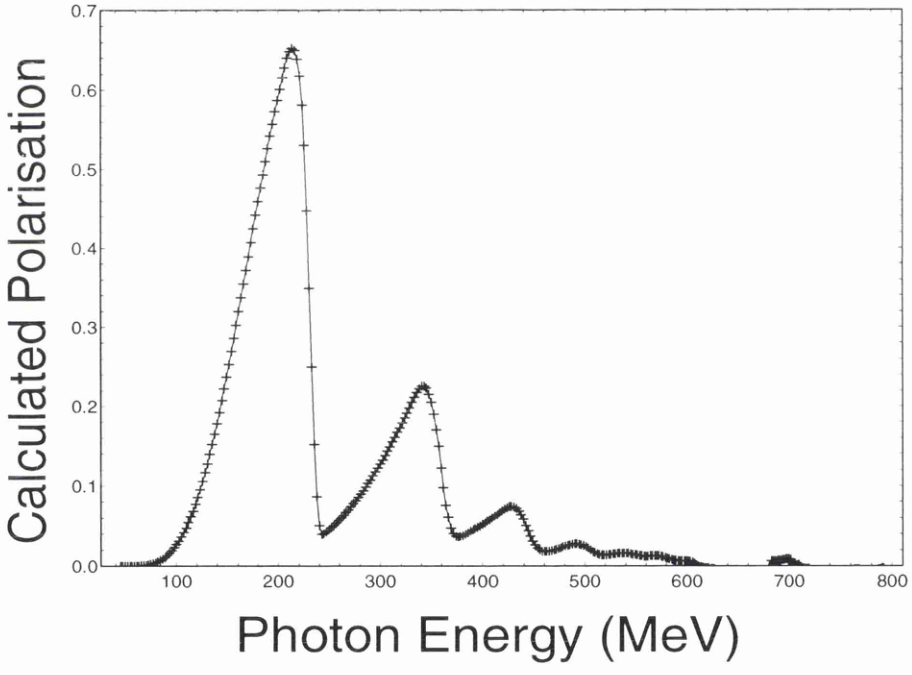


Figure 4.11: *Calculated Polarisation*

the polarisation achieved during the experiment. This can be calculated by using bremsstrahlung spectra obtained during tagging efficiency runs. Here both diamond and nickel radiators were used generating a coherent + incoherent and incoherent spectra respectively. Relative intensities can be obtained by dividing

one by the other and the result can be used to obtain a polarisation spectrum [28]. Figure (4.12) shows a plot of polarisations calculated by both the Göttingen code and the experimental data. The agreement is generally quite good. The

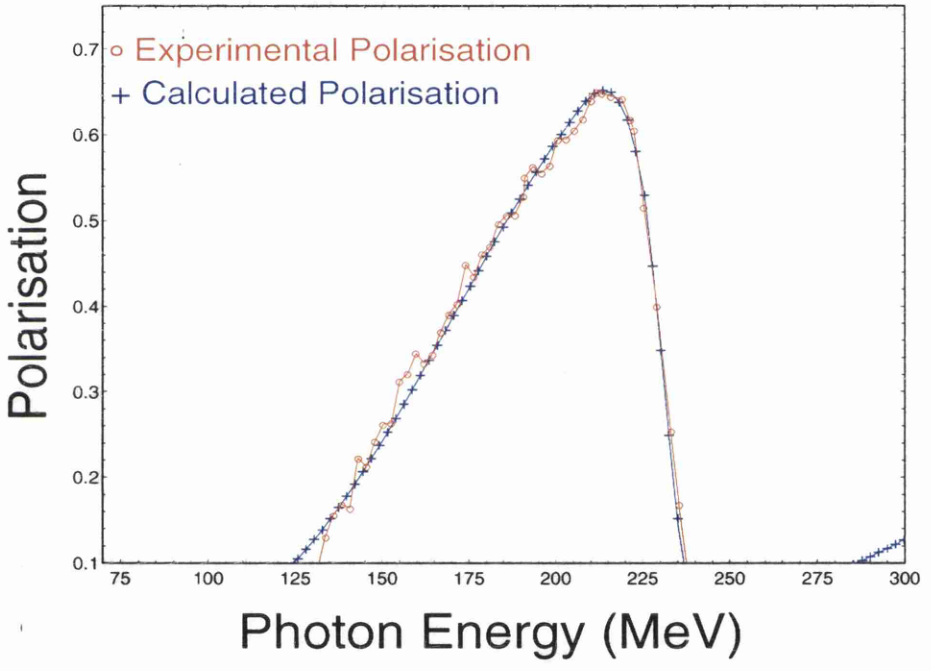


Figure 4.12: *Measured vs Calculated Polarisation*

experimental data has an uncertainty of ~1.5%. The code may be improved by a better knowledge of such factors as the electron beam emittance, collimation and multiple scattering and indeed such a code is being developed at this time [57]. Overall, taking into account the width of photon energy bins used (20 MeV) and the changing value of the polarisation within that bin it was decided that the calculation using the Göttingen code would be satisfactory.

## 4.10 Calculation of Asymmetries

As we have seen in Section 1.3.1, Asymmetry is defined thus:-

$$\Sigma = \frac{1}{P}\frac{d\sigma_{\parallel} - d\sigma_{\perp}}{d\sigma_{\parallel} + d\sigma_{\perp}} \tag{4.5}$$

Therefore in order to calculate the asymmetry one first needs to calculate both the reaction cross sections, d$\sigma$, for both the Para and Perp cases. These cross sections are proportional to the measured yield $Y$ per photon per unit solid angle corrected for random events and detector efficiencies. The yield is then related to cross section d$\sigma$, by the following equation:-

$$Y = n_{target}\, d\sigma \tag{4.6}$$

Where $n_{target}$ is the number of nuclei per unit area in the target intercepted by the beam, and is given by:-

$$n_{target} = \frac{N_A\, \rho_{eff}}{A} \tag{4.7}$$

With $N_A$ being Avagadro's number, $\rho_{eff}$ the target mass per unit area with the target perpendicular to the photon beam and $A$ the atomic mass of the target. As previously discussed the target was positioned at an angle to the beam and therefore the target has an effective density given by:-

$$\rho_{eff} = \frac{\rho}{sin\theta} \tag{4.8}$$

where $\theta$ is the target angle and $\rho$ is the measured density. Table (4.1) gives the relevant parameters for the targets used. This information now allows one to calculate an average double differential cross section. One last correction now has to be made for detector solid angles since the detectors used have only a finite coverage of both the polar and azimuthal angles. Once the solid angles have been calculated for both PiP and TOF the average double differential cross sections

| target | $A$ | $\rho(mg/cm^2)$ | No of $^{12}Cnuclei(cm^{-2})$ | target angle |
|---|---|---|---|---|
| $^{12}C$ | 12 | 664.8 | $3.336\times10^{22}$ | $30^o$ |
| $CD_2$ | 16 | 432.0 | $1.623\times10^{22}$ | $30^o$ |

Table 4.1: *Target Parameters*

for the two directions of polarisation, Para ($\|$) and Perp ($\perp$), are defined thus:-

$$\frac{d^2\sigma_{\|}}{d\Omega_p d\Omega_n} = \frac{Y_{\|}}{\Delta\Omega_p\ \Delta\Omega_n}\ (cm^2/sr^2) \tag{4.9}$$

and

$$\frac{d^2\sigma_{\perp}}{d\Omega_p d\Omega_n} = \frac{Y_{\perp}}{\Delta\Omega_p\ \Delta\Omega_n}\ (cm^2/sr^2) \tag{4.10}$$

This measurement of cross section now allows one to calculate the asymmetry $\Sigma$. These cross sections were evaluated for both Para and Perp, for each of the four photon energy bins within the three setups, giving a total of 24 data sets. For each data set further cuts were made for three missing energy regions. These were made for the 20-40 MeV region, in which the nucleons are emitted from the $(1p)^2$ shells, the 40-70 MeV region in which the nucleons come from a mixture of (1p1s) shells and also for the missing energy region above 70 MeV. Altogether this gave 72 data points.

## 4.11 Experimental Uncertainties

This section outlines the statistical and systematic uncertainties in the experiment. It will outline their measurement and/or estimation and their treatment.

The most basic form of statistical uncertainties arises from the fact that all the data analysed for this present experiment is done so by way of histograming spectra. In the simple case of $N$ counts in a spectrum bin the statistical error in that count is just $\sqrt{N}$. However the matter is complicated by the fact that

weights are used to correct for random events and also detector efficiencies are taken into account. For histograms containing weights, the total content of a spectrum is not just the total number of events, but the total sum of all the weights. These uncertainties are taken care of by dividing events into what is known as sub-events. This is done because random events result in multiple hits being made in the detector systems. All multiple hits in the detector systems can be separated into sub-events. The number of sub-events is simply the sum of the multiplicities of the PiP-TOF-Tagger detector system and for each sub-event a weight is calculated. The result is that for each bin in a histogram the sum of the weights in that bin is actually the sum of the weights of all the sub-events. The uncertainty on that weight is the simply the square root of the sum of all the weights squared.

Systematic uncertainties arise mostly from uncertainties in the physical positions of the detector systems, uncertainties in the calibration procedures, uncertainties in detector efficiencies and uncertainties in the calculation of the photon polarisation. These are outlined below.

**Detector Positions.** Uncertainties in the physical positions of the detectors effect the calculation of solid angles and result in an estimated uncertainty of $\sim$1%.

**Proton Efficiency.** The uncertainties here arise in the rejection of inelastic events and are estimated to be $\sim$2.5%.

**Neutron Efficiency.** The authors of the STANTON code, used to calculate neutron efficiency, estimate an uncertainty of $\sim$5%.

**Tagging Efficiency.** Uncertainties here arise from errors in the value of the efficiency for each tagger channel and are estimated to be $\sim$1.5% per channel.

**Target Density.** The Target was carefully weighed and measured and the angle made to the beam was accurately measured. Overall an uncertainty of ~1% is estimated.

**Polarisation.** The calculation of the polarisation, $P$, itself leads to a small error however the finite size of the photon energy bins used, 20 MeV, results in an uncertainty in the value of the $P$ over the whole bin. The median value of $P$ was calculated and the uncertainty over that bin is estimated to be ~10%.

As this experiment is concerned with asymmetries, and these are derived by taking the ratios of cross sections, many of the above systematic uncertainties will cancel. The efficiencies mentioned above all cancel, leaving only the polarisation as a systematic uncertainty in the asymmetries. This leads to an overall systematic uncertainty in this $^{12}C(\vec{\gamma},pn)$ measurement of ~6% for the measured cross sections and an overall systematic uncertainty of ~10% in the calculation of asymmetries.

# Chapter 5

# Results and Discussion

# Introduction

This chapter presents the results of the present $^{12}C(\vec{\gamma},pn)$ experiment. Firstly the photon energy binning will be explained, then the theoretical simulations used in comparison with the measured asymmetries will be outlined. The next section will present missing energy plots from these photon energy bins for both polarisation directions. From these, asymmetries for various missing energy cuts will be shown and compared to the theory. Next recoil momentum distributions, for the low and medium missing energy regions will be presented and compared to the theory, again asymmetries will be shown for these distributions. The next data to be presented is in the form of angular distributions and this is again compared to the theory. Differential cross sections will then be shown in the next section. The final section will compare the results from the experiment with previous work followed by a short summary.

## 5.1 Photon Energy Bins

As previously discussed the three experimental setups each provided 4 photon energy bins of width 20 MeV, in which the average polarisation was ~25% or more. Table (5.1) lists these bins, along with the average polarisation as calculated by the Göttingen code. Within each of these bins asymmetries have been calculated for 3 missing energy regions. As previously discussed these are 20-40 MeV, 40-70 MeV and the region above 70 MeV.

## 5.2 Theoretical Simulations of Asymmetry

The experimental asymmetries presented in the present work are compared to theoretical calculations using a code developed by the Gent group [41]. As dis-

| *Setup No.* | *Photon Energy Bin* | *Average Polarisation* |
|---|---|---|
| 1 | 150-170 MeV | 0.31 |
| | 170-190 MeV | 0.46 |
| | 190-210 MeV | 0.59 |
| | 210-230 MeV | 0.62 |
| 2 | 200-220 MeV | 0.29 |
| | 220-240 MeV | 0.40 |
| | 240-260 MeV | 0.51 |
| | 260-280 MeV | 0.57 |
| 3 | 280-300 MeV | 0.25 |
| | 300-320 MeV | 0.33 |
| | 320-340 MeV | 0.40 |
| | 340-360 MeV | 0.47 |

Table 5.1: Photon Energy Binning

cussed in Chapter 1 this code represents the most complete theory currently available. This is a fully unfactorized distorted wave calculation which imposes specific kinematical conditions. Firstly quasi-deuteron (QD) kinematics are imposed and secondly, in-plane kinematics are selected. As discussed in the last chapter, QD kinematics were selected for the data. Also restrictions and corrections were made so that only events within $\sim 13.5^{o}$ of the horizontal plane were selected. The resulting measurements of asymmetry were all corrected by the method described in Appendix A in order to correct for variations within this azimuthal range. For low missing energies (20-40 MeV) the theoretical calculations were made for the $(1p_{3/2})^{-2}$ case and for medium missing energies (40-70 MeV) the calculations were made for the combination of (1p and $1s_{1/2})^{-2}$.

## 5.3 Missing Energies and Asymmetries

Missing energy plots provide information on the excitation energies of the residual A-2 system. A comparison of spectra obtained with the photon polarisation parallel and perpendicular to the reaction plane allows the reaction asymmetry to be determined within each photon energy region. Figures (5.1)-(5.12) show missing energy plots for the 12 photon energy bins, along with their associated statistical errors.

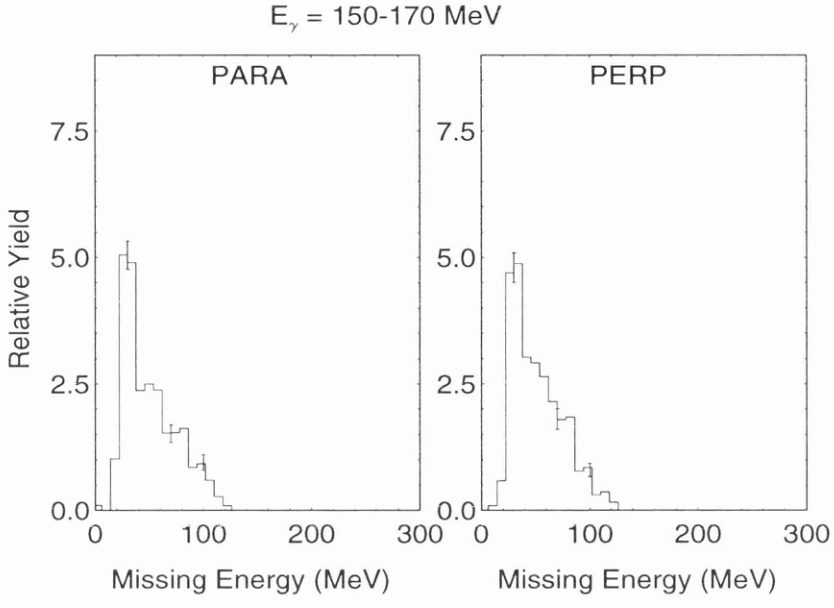


Figure 5.1: *Missing Energies for 150-170 MeV Photon Energy Region.*

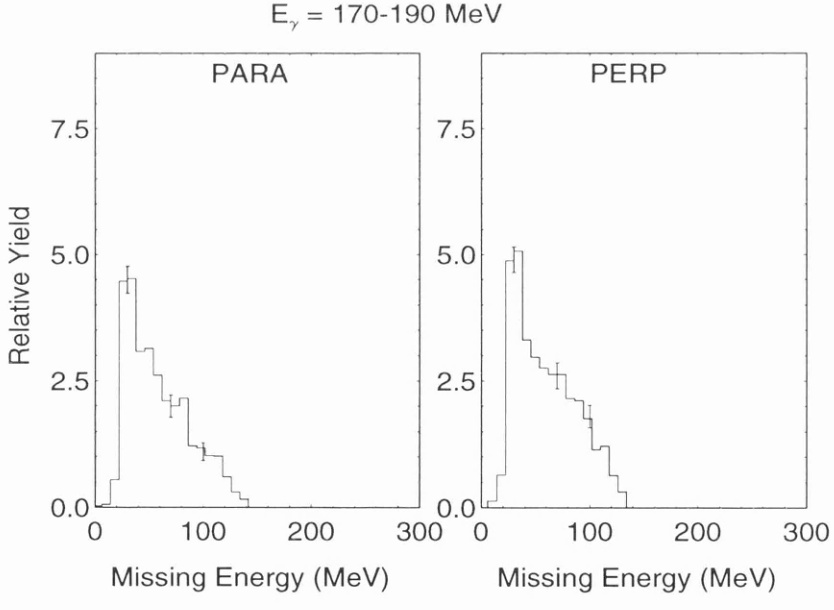


Figure 5.2: *Missing Energies for 170-190 MeV Photon Energy Region.*

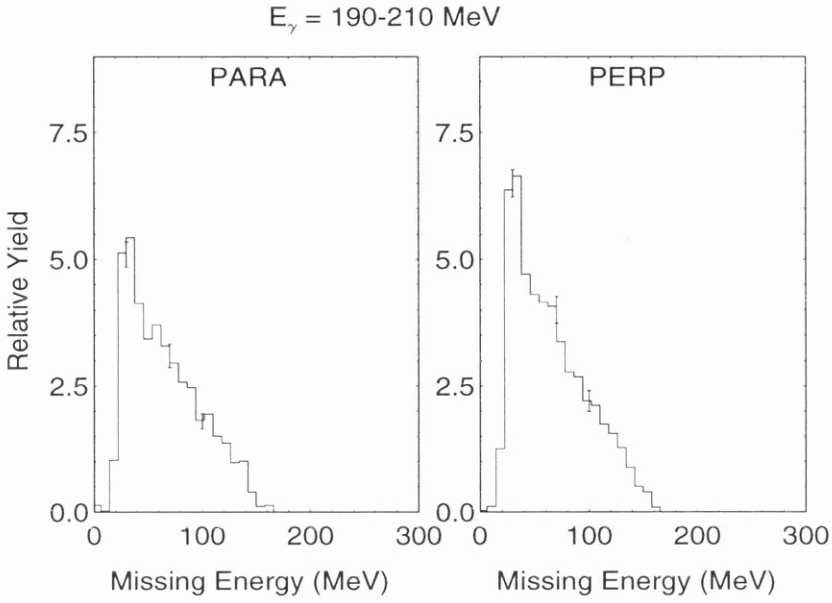


Figure 5.3: *Missing Energies for 190-210 MeV Photon Energy Region.*

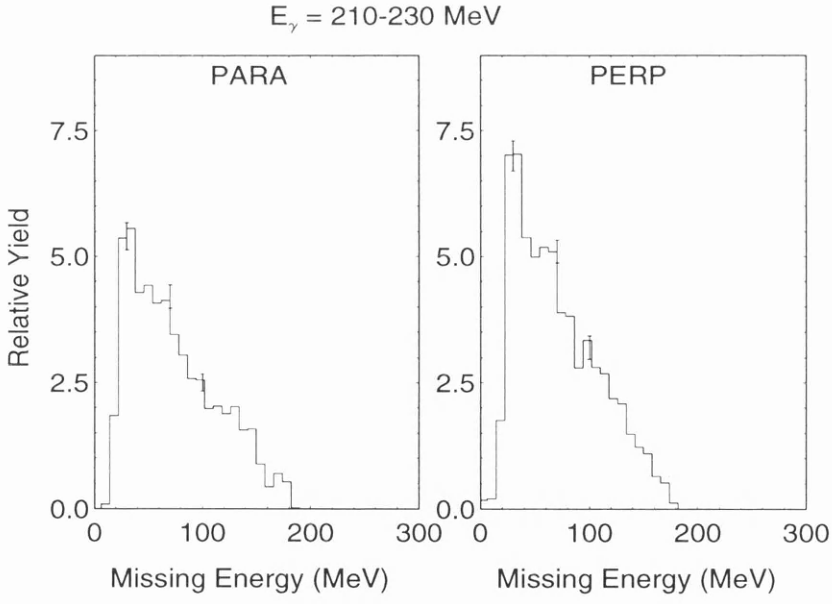


Figure 5.4: *Missing Energies for 210-230 MeV Photon Energy Region.*

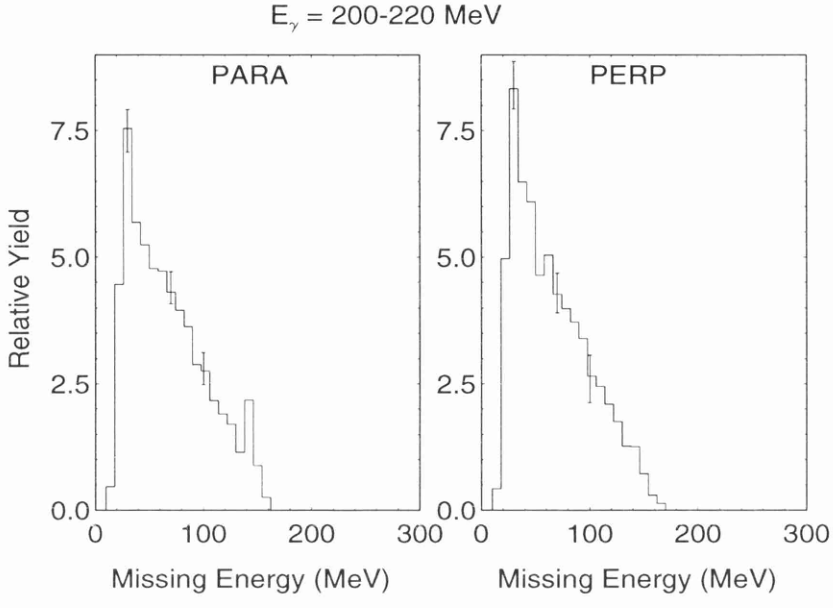


Figure 5.5: *Missing Energies for 200-220 MeV Photon Energy Region.*

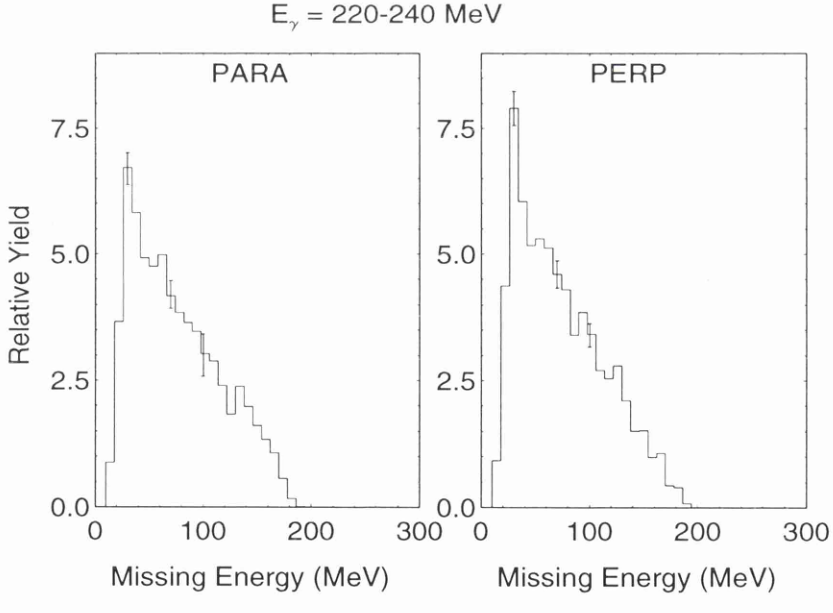


Figure 5.6: *Missing Energies for 220-240 MeV Photon Energy Region.*

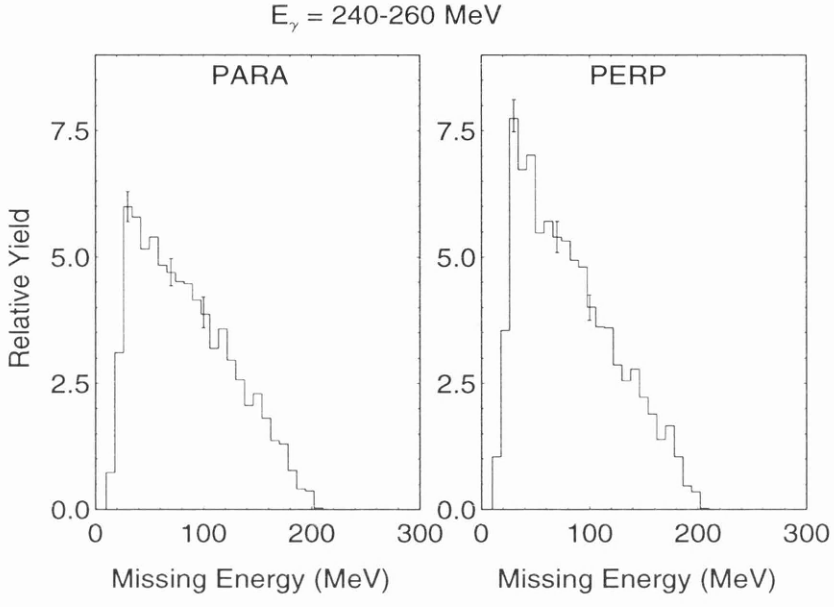


Figure 5.7: *Missing Energies for 240-260 MeV Photon Energy Region.*

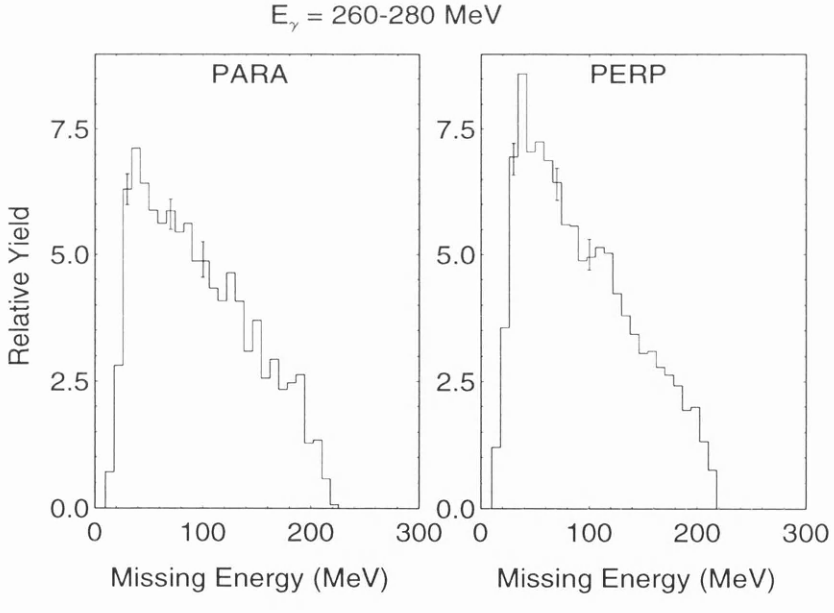


Figure 5.8: *Missing Energies for 260-280 MeV Photon Energy Region.*

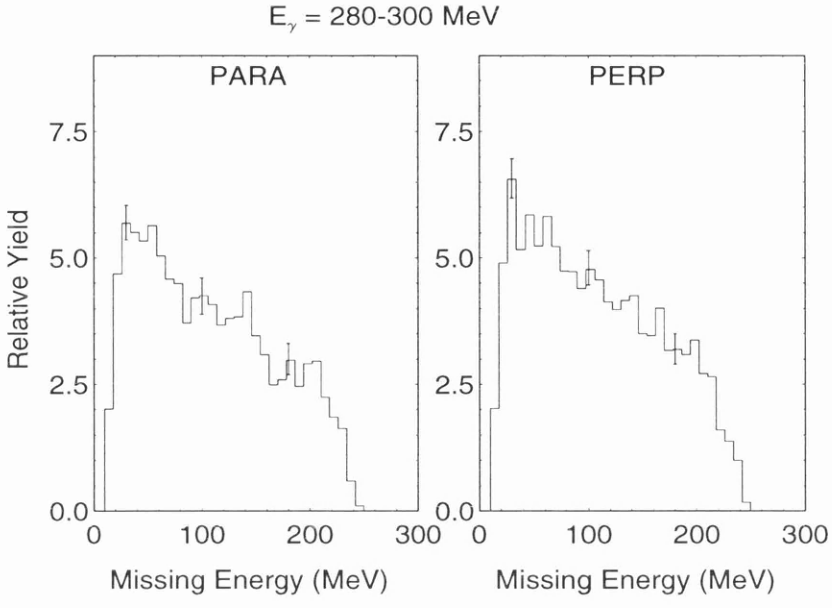


Figure 5.9: *Missing Energies for 280-300 MeV Photon Energy Region.*

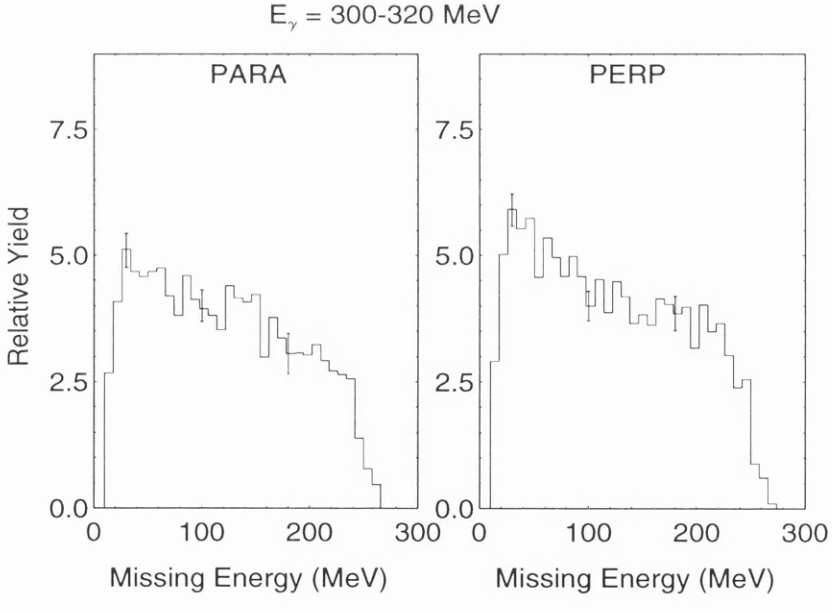


Figure 5.10: *Missing Energies for 300-320 MeV Photon Energy Region.*

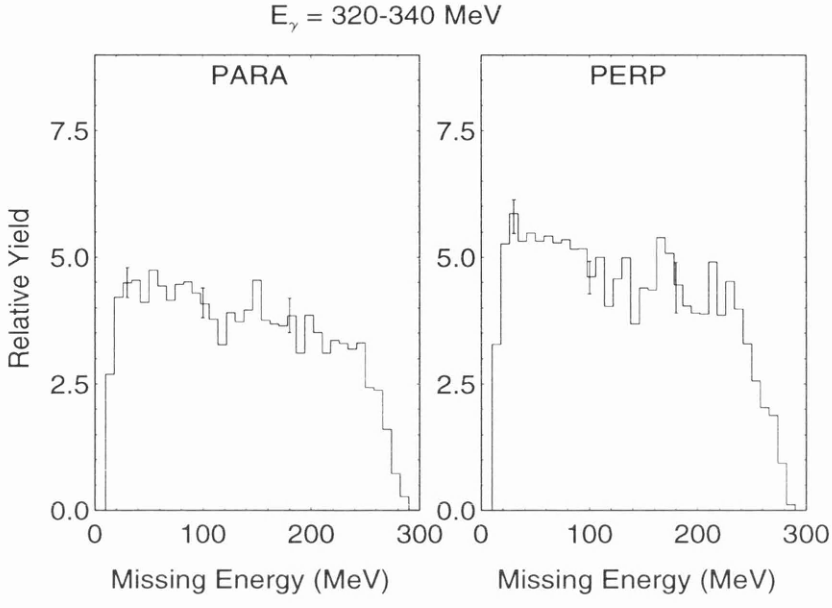


Figure 5.11: *Missing Energies for 320-340 MeV Photon Energy Region.*

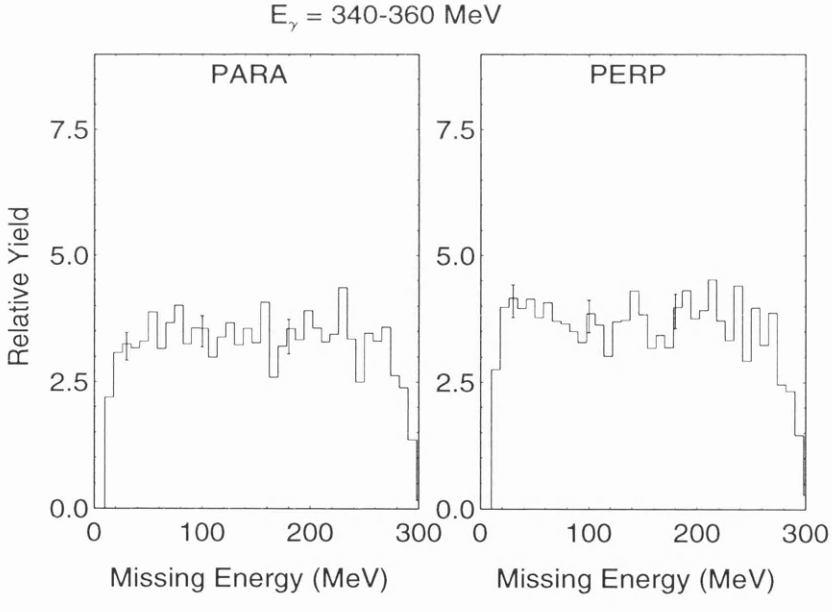


Figure 5.12: *Missing Energies for 340-360 MeV Photon Energy Region.*

The features of these plots correspond to those seen in previous studies of the $^{12}C(\gamma,pn)$ reaction [5]. In the first photon energy region one can clearly see a peak at $E_{miss}$ ~28 MeV corresponding to the population of states around the ground state in the residual $^{10}B$ nucleus. As one goes up in photon energy this peak becomes noticeably less pronounced, and is not evident above ~300 MeV From the plots for both polarisation directions it is possible to observe the effects of the reaction asymmetry. Below 200 MeV one can see that the yield for the perpendicular direction is comparable to that for the parallel one. Above 200 MeV photon energy, the perpendicular yield starts to get larger relative to the yield in the parallel direction. Making cuts on various photon energy regions one can plot these asymmetries as a function of photon energy, figures (5.13-5.16).

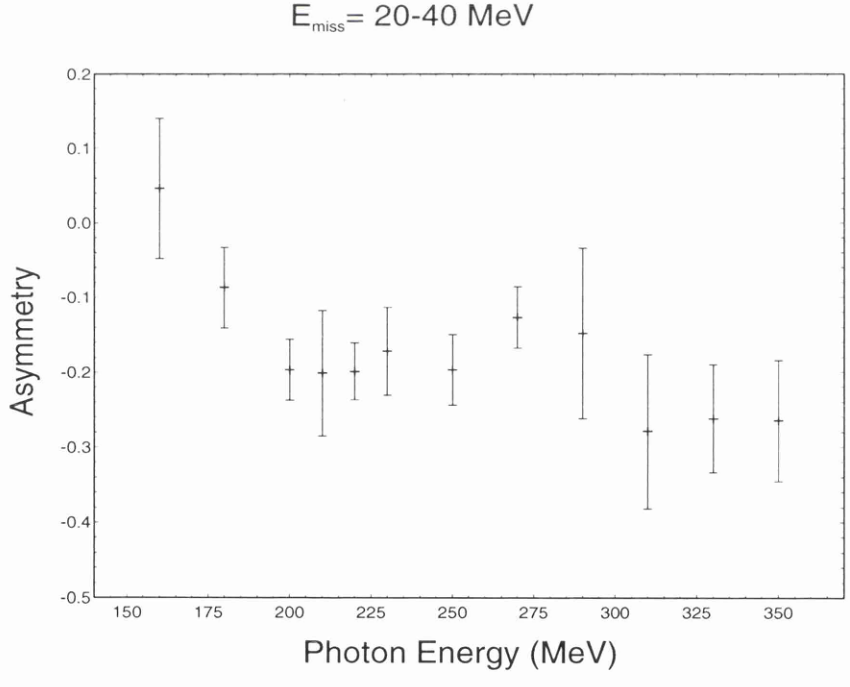


Figure 5.13: *Asymmetries for the 20-40 MeV Missing Energy Region.*

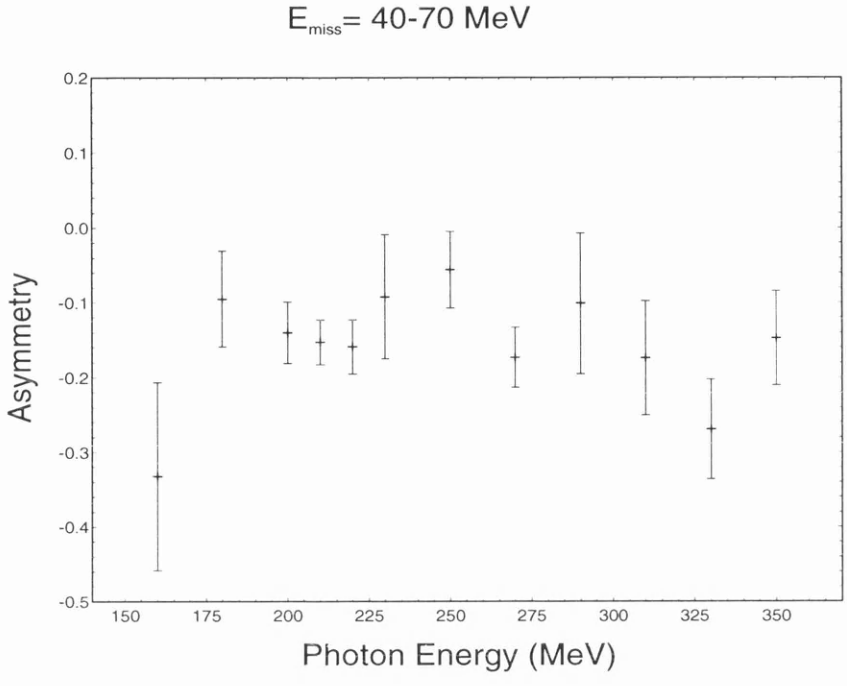


Figure 5.14: *Asymmetries for the 40-70 MeV Missing Energy Region.*

In the low missing energy region, figure (5.13), one can clearly see a distinct trend in the reaction asymmetry. Starting from the lowest photon energy bin, the asymmetry is observed to be almost zero, if not slightly positive. It then appears to fall rapidly to a value ~-0.20 around 200 MeV. It is then observed to stay fairly constant with a slight rise at ~270 MeV. After this it appears to fall slightly and then stays fairly constant again. This observed behaviour will later be compared to previous results obtained from other studies. Previous studies, [5, 3] have shown that in this region *pn* emission is due to direct gamma absorption on *pn* pairs emitted from $(1p)^2$ orbitals. This variation in the reaction asymmetry can therefore be attributed to the changes in the microscopic mechanisms contributing to direct two nucleon emission, as the incident photon energy is varied.

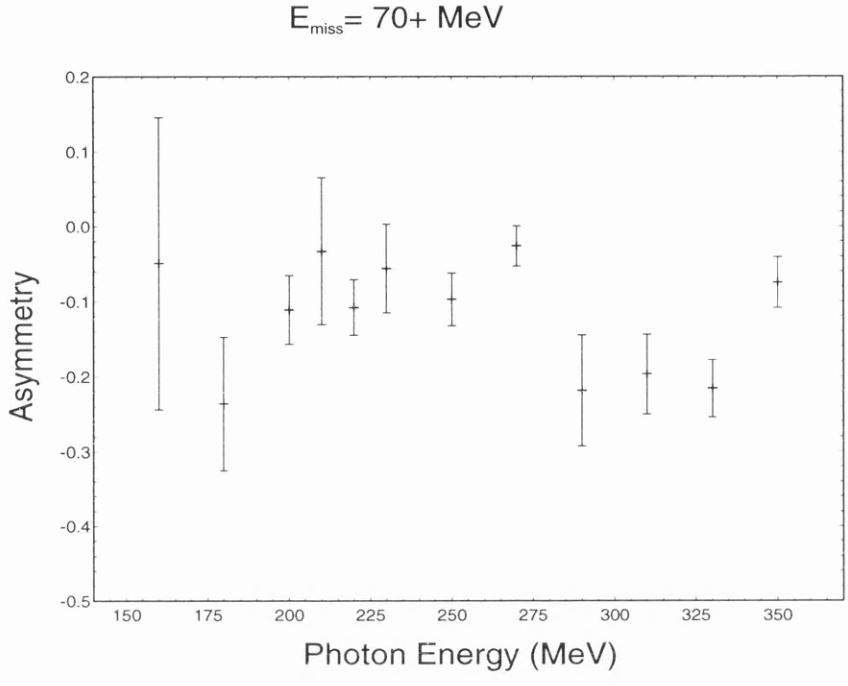


Figure 5.15: *Asymmetries for the 70+ MeV Missing Energy Region.*

Figure (5.14) shows the asymmetry for the 40-70 MeV missing energy region. Here the magnitude of the asymmetry is reduced and does not appear to show the same rapid changes observed in the low missing energy region. However, there does appear to be a gradual fall in the asymmetry as the photon energy is increased. In this region the *pn* pair are assumed to have been emitted from a mixture of (1p) and (1s) shells. Previous studies, [3] have shown that absorption on a $(1s)^2$ pair is weak and its strength is widely spread. It is not possible to easily separate this absorption from the 1s1p strength and therefore no attempt was made to do so. Again in this region emission is mainly due to direct gamma absorption on a *pn* pair, although some FSI contribute.

The data in figure (5.14) suggest that at low $E_\gamma$ a different process is respon-

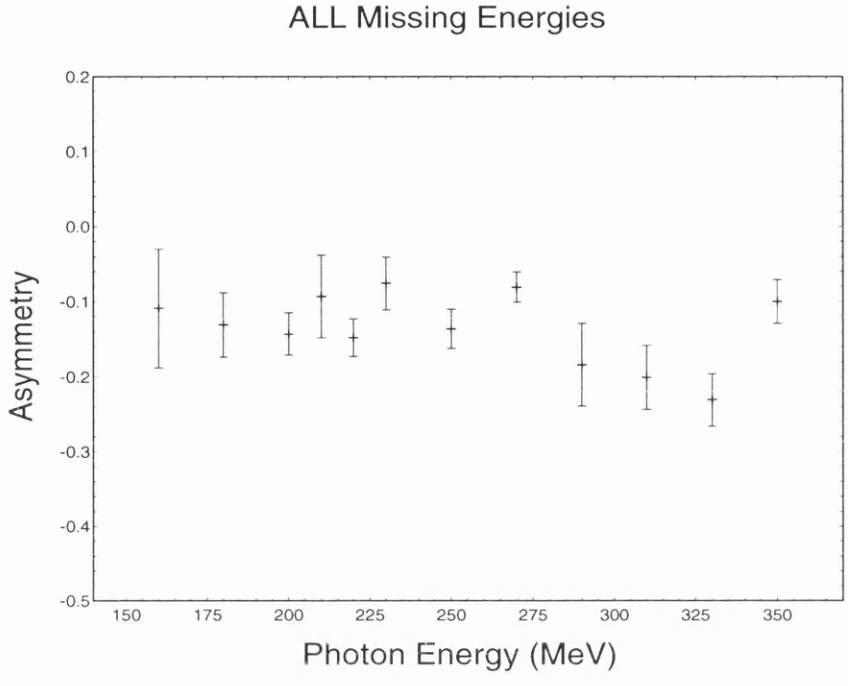


Figure 5.16: *Asymmetries for all Missing Energy Regions.*

sible for the different behaviour of the photon asymmetry in this missing energy region. The only difference in this region is due to the contribution from nucleons in 1s shells, together with a slight contribution from non-direct gamma absorption. One must conclude that these contributing processes are responsible for this difference.

Figure (5.15) shows the reaction asymmetry for the missing energy region above 70 MeV, the so-called high missing energy region. Here the picture is not so clear. There is indeed a measurable asymmetry and it can be seen to vary with photon energy. Above 175 MeV the measured value of the asymmetry seems to increase and then decrease. The 2N model cannot produce any strength in this missing energy region and *pn* emission is assumed to come from a combination

of two and three-nucleon absorption processes, together with a large contribution from an initial QF$\pi$ process, [20]. An interesting observation to note is that at photon energies below the $\Delta$ resonance region the values of photon asymmetry are all closer to zero than in lower missing energy regions. However, around the $\Delta$ resonance region, the value of photon asymmetry begins to become much more negative.

Figure (5.16) shows the reaction asymmetry for all missing energy regions. This includes missing energy data from 10 MeV upwards and, as the highest value of missing energy changes with photon energy, has no set upper limit. Here, as in the medium missing energy case, no gross trend is apparent. However, despite contributions from many processes a distinct asymmetry is observed. Again one could argue that within the limits of the data, there is a gradual fall in the value of the reaction asymmetry with increasing photon energy. The contributing reaction mechanisms here are complicated and, as previously discussed, involve an initial QF$\pi$ process.

An interesting point to note in these plots is that the data have an overlap of photon energies between setup 1 and 2. This can be seen in figure (5.13-5.16). The data points are well matched over this overlap, and this gives confidence in the calculation of $P$.

One can now compare the results obtained for the 20-40 MeV and the 40-70 MeV missing energy regions with the theoretical predictions from the Gent code. Figure (5.17) shows such a comparison. In the top frame the results from the low missing energy region (20-40 MeV) are compared with the theory for a full distorted wave calculation for the $(1p_{3/2})^{-2}$ case. The code predicts the behavior of the data at photon energies above 200 MeV quite well. It models the absolute magnitude of the measured asymmetry, within the error bars. However it fails to predict the sharp fall in the data between 150 and 200 MeV. Indeed, the

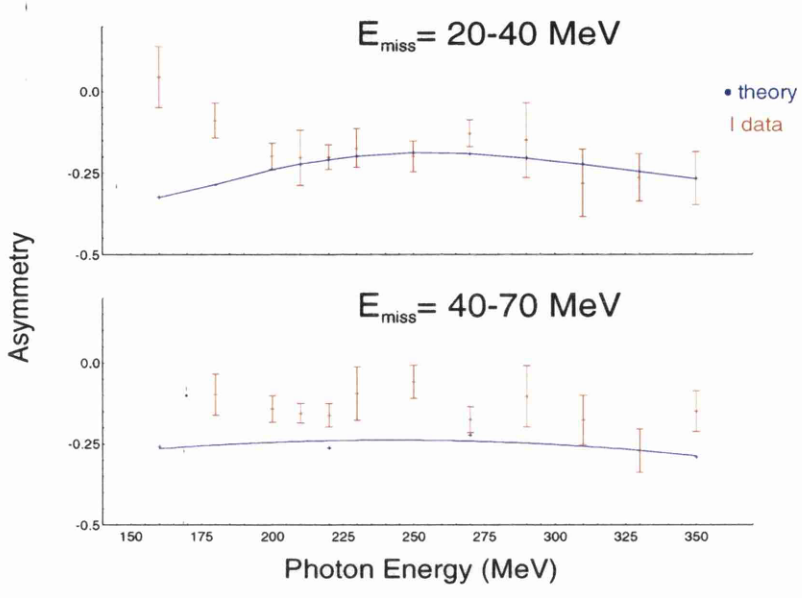


Figure 5.17: *Data vs Theory for Low and Med* $E_m$

values from the code rise slightly over this region. The second frame shows the experimental and theoretical values for the 40-70 MeV region. The calculation is for the 1s1p + $1s^2$ case. Here the calculations have a similar magnitude to the lower missing energy region, but a flatter photon energy dependence. The data generally lie above the prediction. Hard scattering FSI are likely to slightly reduce the magnitude of the photon asymmetry, and the difference between the data and the prediction may be an indication of some FSI contributions in this missing energy region. This has been suggested by recent work [56, 58]. However, it is unlikely that FSI are responsible for more than a small reduction in photon asymmetry and this is therefore an indication that the theory is incomplete. These measured asymmetries are tabulated in tables (B.3-B.6).

## 5.4 Recoil Momentum and Asymmetries

Recoil momentum distributions allow us to examine the momentum distribution of the recoiling system. This shows us if the recoiling system is a spectator and also if the same absorption process is present throughout all values of recoil momentum. For 2N photon absorption, with no final state interactions, this recoil momentum has a magnitude equal to the momentum of the initial pair. Recoil momentum distributions were made using a well proven 2N photon absorption model [15]. This provides a check that the process is indeed 2N absorption. This model enables the effect of detector acceptances on the distribution of 2N momenta seen by the detectors to be obtained. The model assumes photon absorption takes place on a 2N pair, while the rest of the nucleus acts as a spectator. Harmonic oscillator wave functions are used to calculate the initial momentum of the 2N pair. In this model final state interactions are ignored, but as we have seen in Section 1.3.4 the Gent code predicts that distortion of the outgoing nucleon waves has little or no effect upon the reaction asymmetry. The 2N model was compared to data from the 3 setups and is shown in figures (5.18-5.20). The model has been scaled in order to test the shape of the distributions, and show that the 2N model is valid. For each setup the calculation was performed for a photon energy range covering all the photon energy bins. This was then compared with data for a combined polarisation, (Para + Perp), and then for each polarisation direction separately.

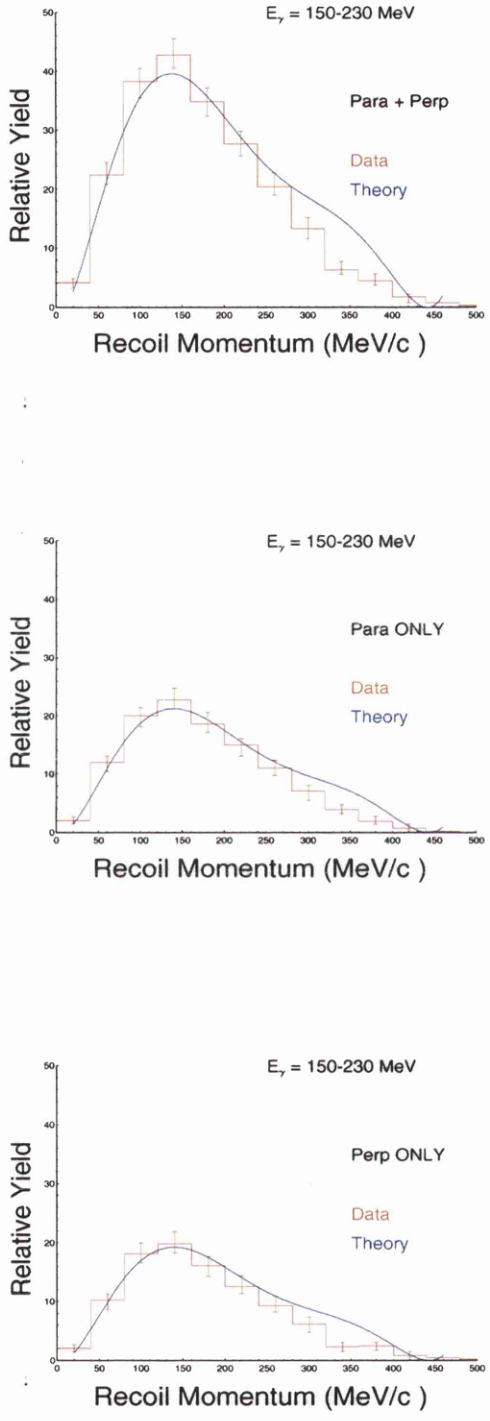


Figure 5.18: *Recoil Momentum in 2N Model, $E_m$ = 20-40 MeV, Setup No 1.*

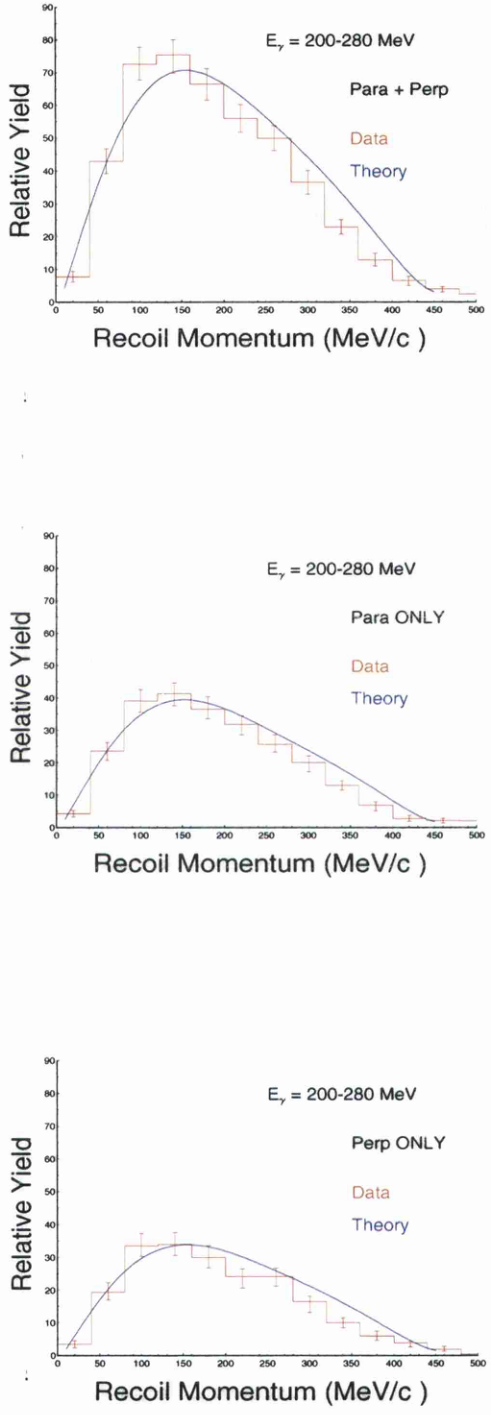


Figure 5.19: *Recoil Momentum in 2N Model, $E_m$ = 20-40 MeV, Setup No 2.*

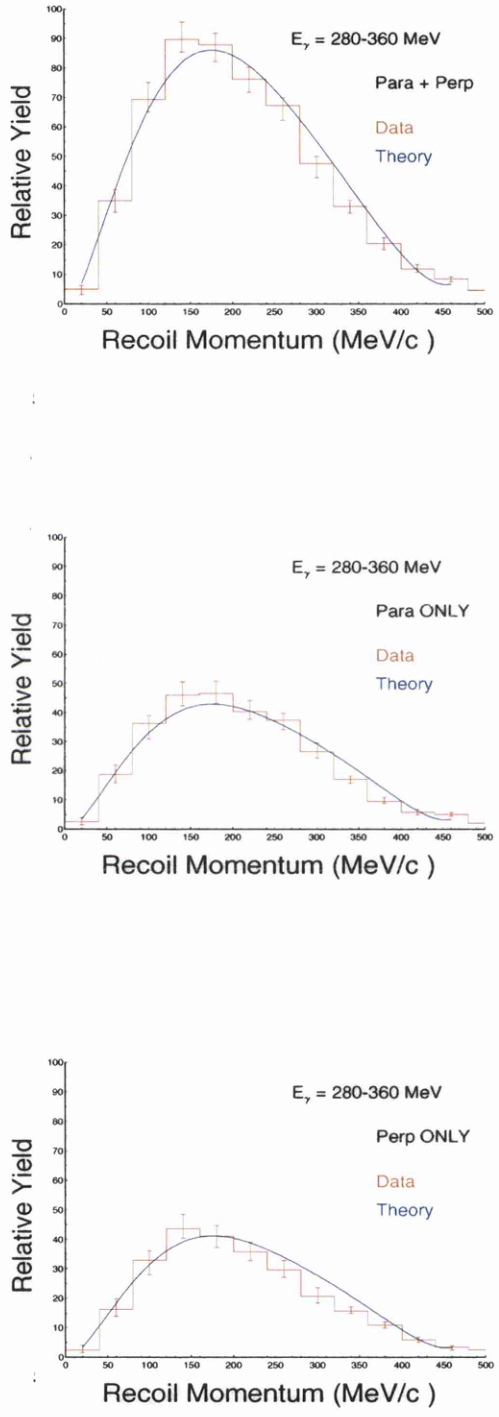


Figure 5.20: *Recoil Momentum in 2N Model, $E_m$ = 20-40 MeV, Setup No 3.*

As can be seen the model gives a reasonably good fit to the data, and there is no difference in the shape of the distribution for parallel and perpendicular kinematics. We might expect that the sum (Para + Perp) would agree with the theory but it could be that the 2 separate directions do not. However in the present data we see no such disagreement. This comparison with the parallel, perpendicular and combined cases leads to the conclusion that photon absorption is indeed taking place on a correlated 2N pair, with final state effects having no appreciable effect for this low missing energy region. An analysis is also made of the asymmetries as a function of recoil momentum. This could provide an indication as to whether there is any dependence of $\Sigma$ on $P$. It is at present uncertain from the theory whether there is any such dependence. It could also be the case that if 2N absorption is indeed the dominant process, with final state interactions having little or no effect, then one could expect that the reaction asymmetry would have a constant value over the whole momentum range. This analysis was done by taking the low missing energy region, (20-40 MeV) and measuring the asymmetries of the recoil momentum distributions. These are shown in figures (5.21-5.23).

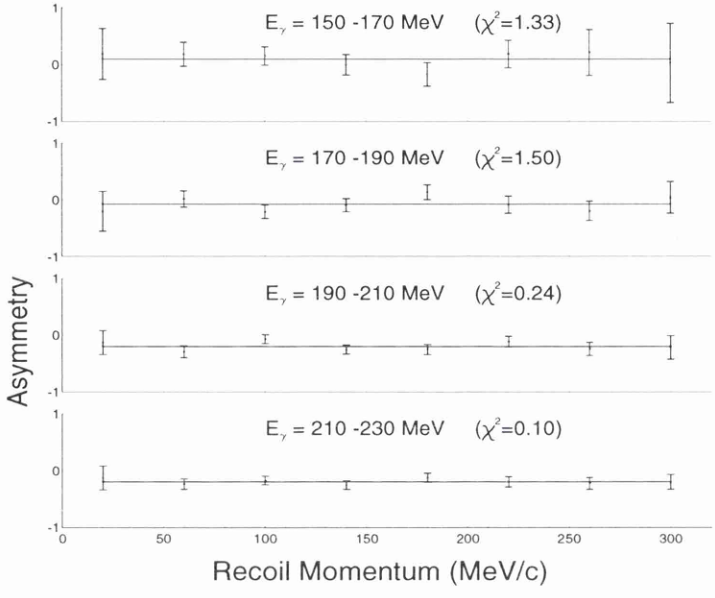


Figure 5.21: *Recoil Momenta Asymmetries, $E_m$ = 20-40 MeV, Setup No 1.*

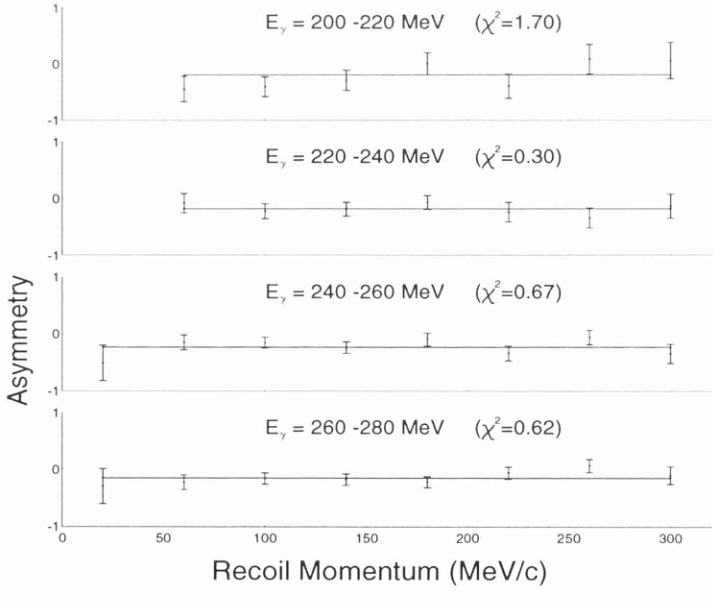


Figure 5.22: *Recoil Momenta Asymmetries, $E_m$ = 20-40 MeV, Setup No 2.*

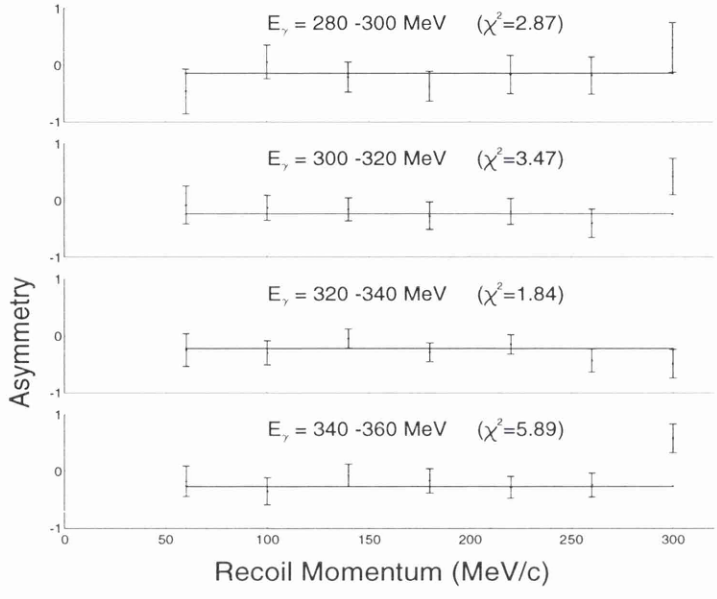


Figure 5.23: *Recoil Momenta Asymmetries, $E_m$ = 20-40 MeV, Setup No 3.*

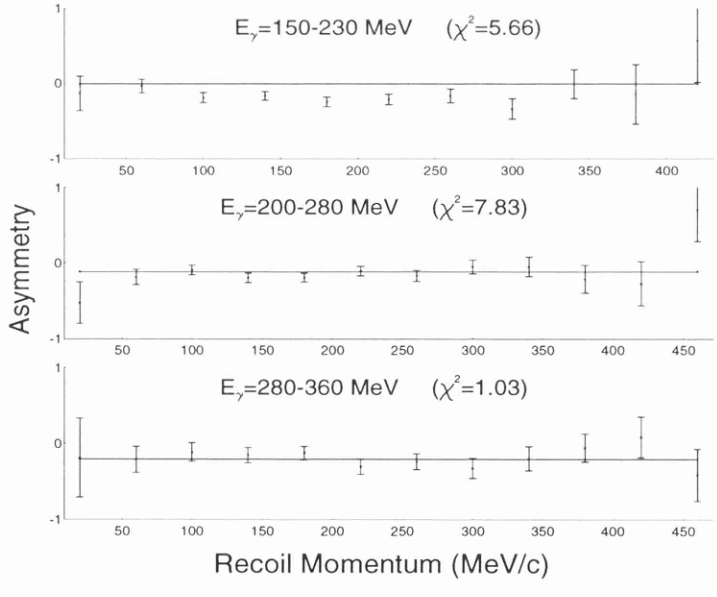


Figure 5.24: *Recoil Momenta Asymmetries, $E_m$ = 40-70 MeV.*

As can be seen these plots show that within the statistical errors the asymmetries have a constant value for all but the the highest 4 photon energy regions. In all the figures an average straight line has been fitted to the data and it's associated chi squared value is shown. In these highest 4 photon energy regions the asymmetries are constant up to the highest values of recoil momentum, where the asymmetry has a lower magnitude. These variations are only evident at the tails of the recoil momentum distributions where the yields are low, hence the larger error bars. Hard FSI might produce events with large recoil momenta and lower asymmetries. However in the present data all directions for a given $P$ are averaged over and therefore if there were a small dependence of $\Sigma$ on $P$ it could well be averaged out. The conclusion is that for low missing energies, the same reaction mechanism could indeed be taking place for all but the highest recoil momenta at the highest photon energies. No significant dependence of $\Sigma$ on $P$ is seen, although a small dependence could be smeared out. For medium missing energies (40-70 MeV), the recoil momentum asymmetries are shown in figure (5.24). Note that the data points extend to higher values of recoil momentum. Here distributions are plotted for 3 photon energy regions, corresponding to the 3 setups. As can be seen these distributions are again essentially flat except at very low and high values of recoil momentum, where the yields are again low. Again it seems that the same reaction mechanism is taking place up to the highest values of recoil momenta, producing these flat distributions. Again any small dependence of $\Sigma$ on $P$ could be averaged out.

## 5.5 Angular Distributions and Asymmetries

With the data is was possible to make angular sub-divisions. This was done by making cuts on the proton polar angle in PiP, $\Theta_{proton}$, which covers an angular

| *Angular Bin No.* | *Angular Range (Lab Frame)* |
|---|---|
| 1 | $52^o$-$71^o$ |
| 2 | $72^o$-$91^o$ |
| 3 | $92^o$-$111^o$ |
| 4 | $112^o$-$130^o$ |

Table 5.2: *Proton Angular Binning*

range of $52^o$ - $130^o$. Table (5.2) lists the four separate angular bins selected. These correspond to the polar angle coverage of the PiP B-layer elements.

The results from the Gent code give an asymmetry as a function of proton angle, in the centre of mass frame. The data in the lab frame were therefore converted to the centre of mass frame for comparison with the Gent predictions. This was done, using a well proven method [59], taking into account the fact that the size of this change increases with photon energy. For example, between the lowest photon energy bin and the highest, the CM angle changes by just over 5 degrees. Once the data are in the centre of mass frame it is possible to compare them with the predictions of the Gent code. Calculations are available for the $1p_{(3/2)}^{-2}$ case and figures (5.25-5.27) show the comparison between theory and data. As can be seen, above photon energies of about 200 MeV the data fit the theory quite well. Both the magnitude and the shape of the angular distributions are well matched. However, below 200 MeV the theory begins to deviate in magnitude and shape from the data. As seen previously in figure (5.17) the Gent code predicts a lower magnitude for the asymmetry, below 200 MeV, than is seen in the data. Overall, the theory gives good predictions in the $\Delta$-resonance region, but fails at lower photon energies. This lower $E_\gamma$ region is precisely where angular distribution studies [10] have shown that $\rho$ meson exchange may have a

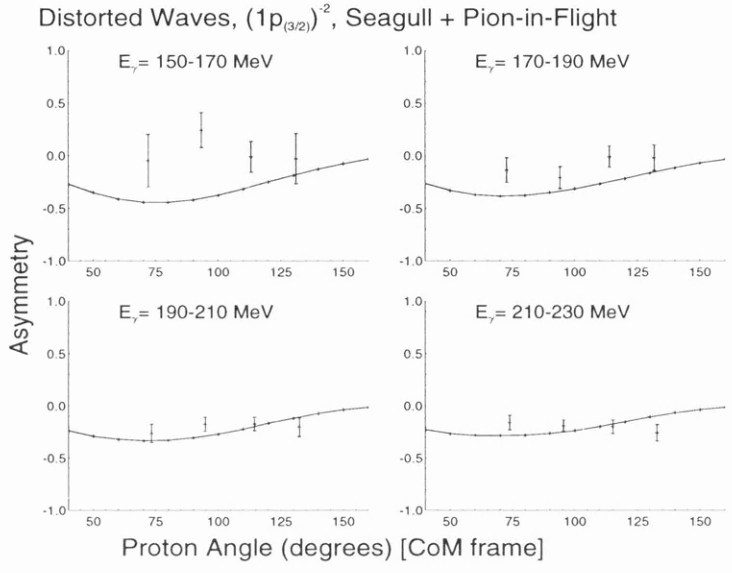


Figure 5.25: *Angular Data vs Theory for Setup 1*

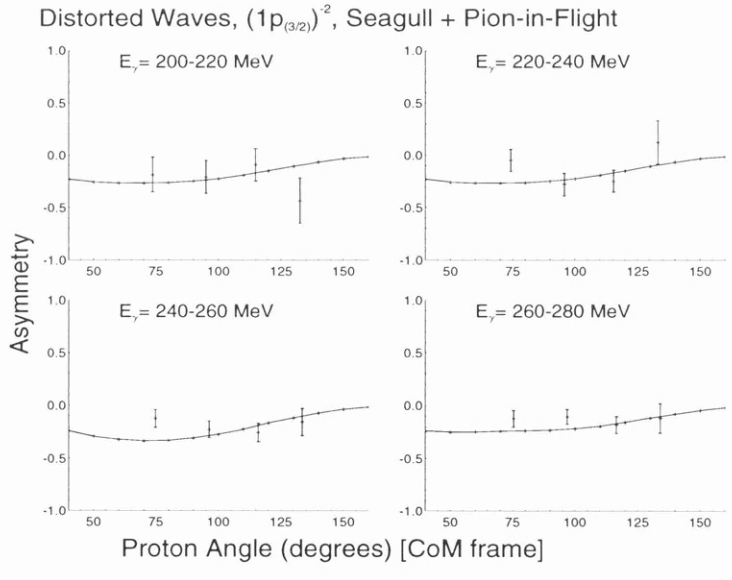


Figure 5.26: *Angular Data vs Theory for Setup 2*

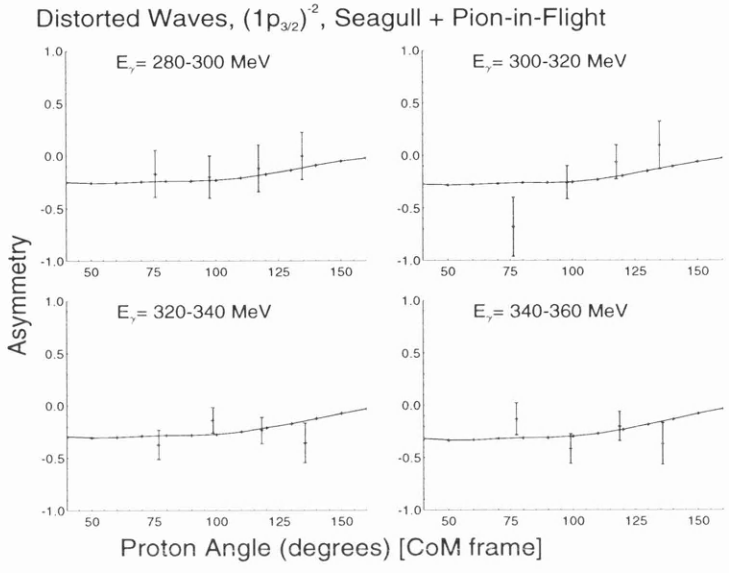


Figure 5.27: *Angular Data vs Theory for Setup 3*

significant influence. The present calculations do not include such terms. The measured values of these asymmetries are tabulated in tables (B.7-B.9).

## 5.6 Differential Cross Sections

As part of the study of photon asymmetry the reaction cross sections for the 12 photon energy regions have been measured for the low missing energy region (20-40 MeV), for both the Para and Perp directions and these are shown in figures (5.28-5.30). These cross sections are double differential and are subject to the various cuts in the data analysis as previously described in section 4.10.

Starting at the lowest photon energy region one can see that the cross section for Para is slightly bigger than the cross section for Perp and therefore this leads to a positive asymmetry. As we goes up in photon energy the Perp cross section gets larger than the Para one and so one can see the asymmetry goes through zero and decreases, until around 200 MeV, above which it stays fairly constant.

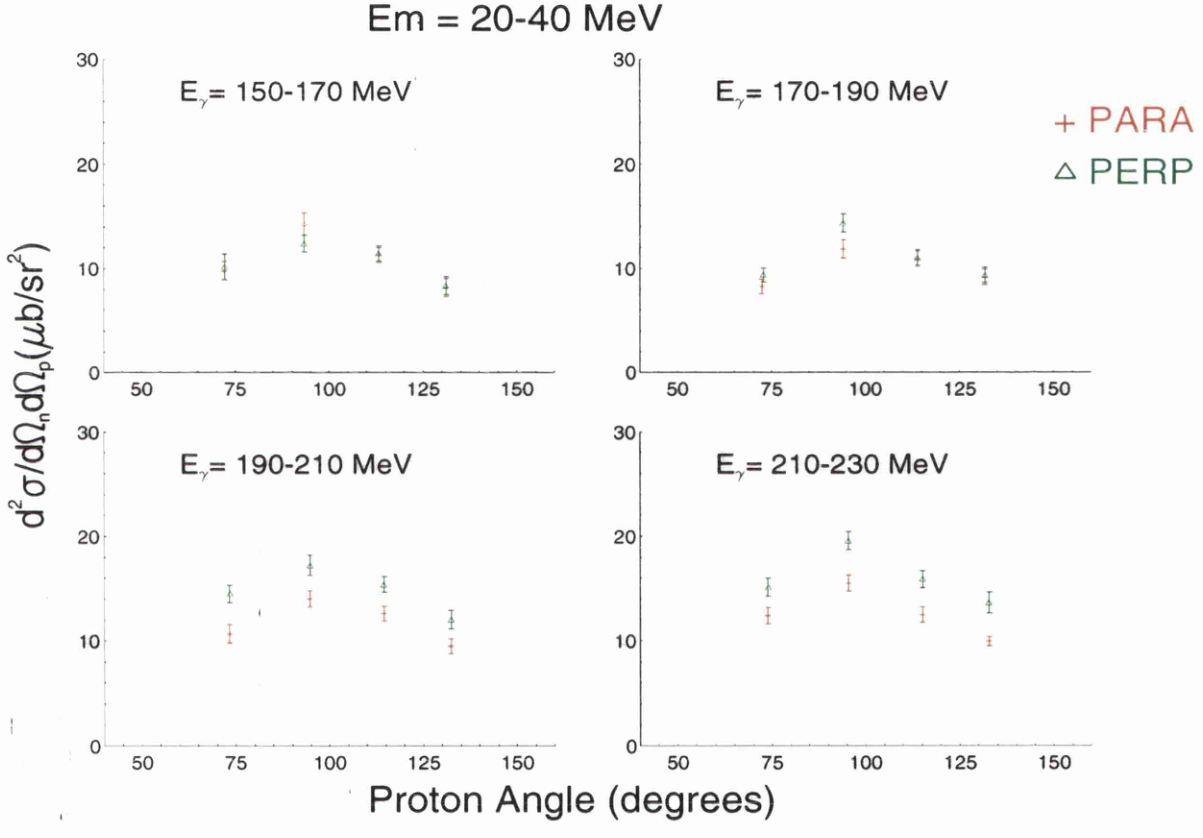


Figure 5.28: *Measured Cross Sections for Setup 1*

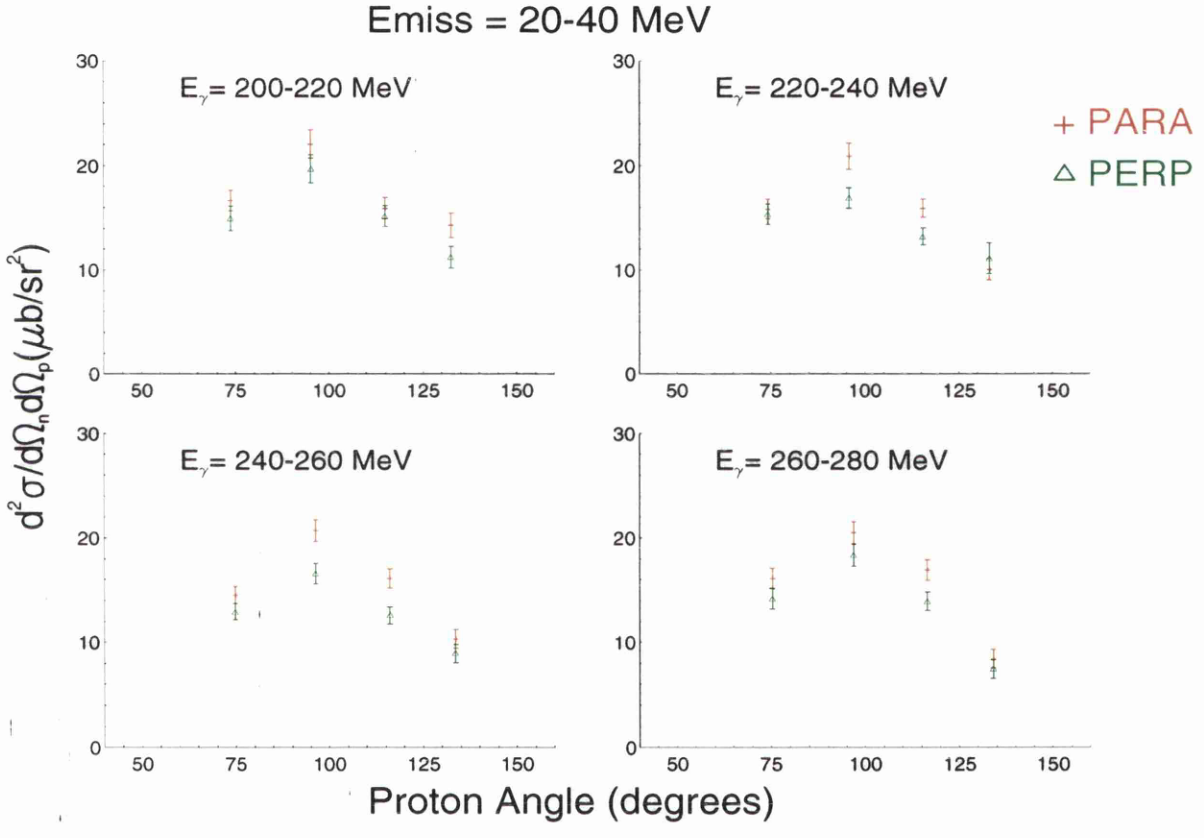


Figure 5.29: *Measured Cross Sections for Setup 2*

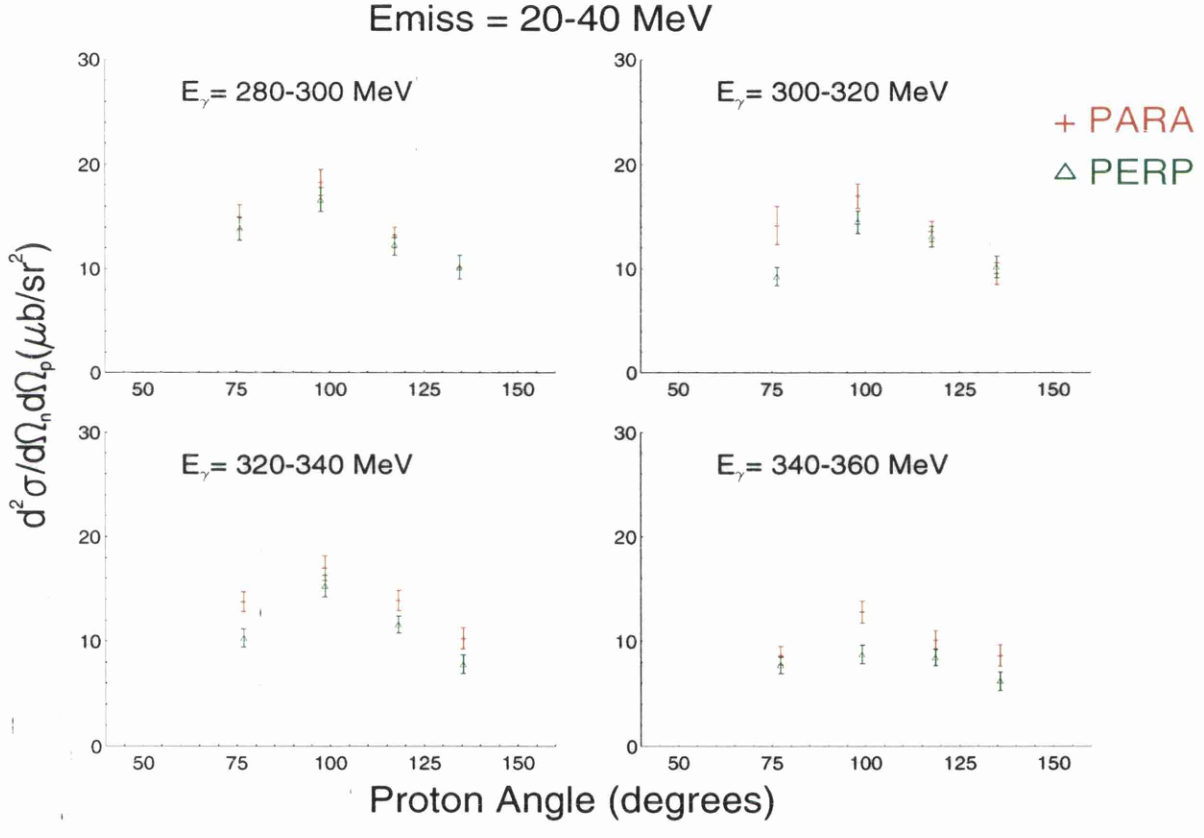


Figure 5.30: *Measured Cross Sections for Setup 3*

This behavior is consistent with that already seen for the measured reaction asymmetry. These cross section values for both the Para and Perp directions of polarisation are tabulated in tables (B.10-B.12).

These measured cross sections can be compared to a previous study of the angular distribution of the $^{12}C(\gamma,pn)$ reaction, [10]. This is done by calculating the average polarisation independent cross section. The data from the previous study agrees within errors with the present data.

## 5.7 Comparison With Previous Experiments

It is informative to compare the asymmetries measured in the present experiment with results from previous work. As discussed in Chapter 1, all of the previous work has been done on nuclei other than carbon, but the results reveal clear trends when comparisons are made. The first comparison made is with the deuterium calibration data. The deuterium data from this present experiment cover a proton angular range of 70-110 degrees and covers all missing energies. As can be clearly seen in figure (5.31) the deuterium data fits well when compared to the deuterium data measured by the Daphne collaboration [60] and at Yerevan [25], which were both measured at 90 degrees in the centre of mass frame and averaged over all missing energies. The comparison gives confidence in the accuracy of the calibrations and the data analysis method. Figures (5.32 and 5.33) show low missing energy data from this work compared to previous data. The data from Yerevan [25] was measured in QD kinematics at a proton angle of 90 degrees in the centre of mass frame. The present carbon data were also measured under QD kinematics but with a range of proton polar angle of 50-130 degrees. However the proton polar angle distribution is peaked at 90 degrees and, as can be seen in figures (5.25-5.27), the asymmetries are not strongly angle dependent. Both

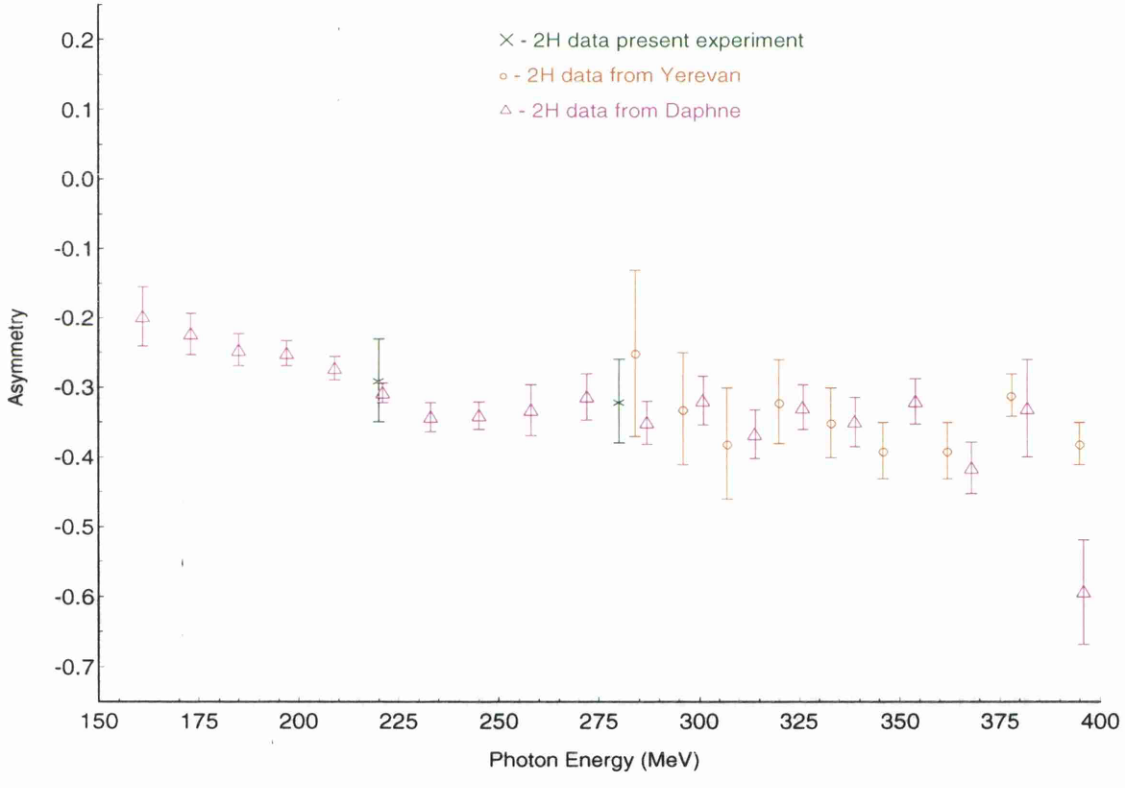


Figure 5.31: *Comparison of Deuterium Asymmetry with previous experiments*

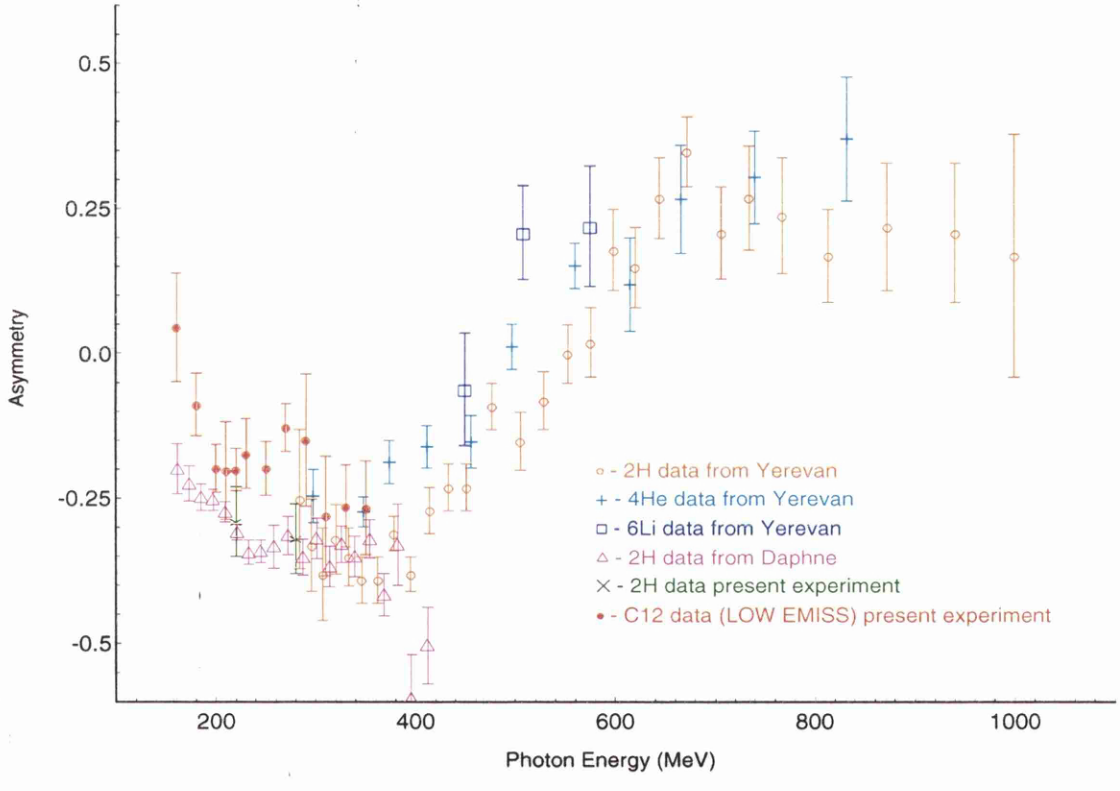


Figure 5.32: *Comparison of Low $E_m$ Asymmetry for 2H and 12C with previous experiments*

the carbon data and the deuterium data used for the calibrations are shown on the plot. The carbon asymmetry follows the same general trend in shape but has a smaller amplitude than the data from lighter nuclei. If one looks at the lithium data from Yerevan, although only 3 data points were measured, one sees that this also has a smaller amplitude than the lighter $^{2}$H and $^{4}$He nuclei. One could conclude that even relatively heavy nuclei such as carbon have photon asymmetries which seem to follow the general trend of other nuclei. However the absolute magnitude of these asymmetries seems to be reduced in heavier nuclei. The data can be made clearer by rescaling this plot and this is done in figure (5.33). We can also compare data from medium missing energies with this previous data. This is done in figure (5.34) and again rescaled in figure (5.35). Again the carbon data appears to be following the general trend although, as we have seen, the magnitude of the measured asymmetries is reduced further in this missing energy region, compared to deuterium.

## 5.8 Summary of Experimental Results

The present experiment measured asymmetries in a total of 12 photon energy bins. The missing energy distributions measured compared well to previous studies using unpolarised photons. At low missing energies (20-40 MeV), the measured asymmetries showed a rapid reduction from $\sim$0 to $\sim$–0.2 from 150 to 200 MeV, followed by a slower fall to $\sim$–0.25 at $E_\gamma = 350$ MeV. This is similar to the behaviour of lighter nuclei found in previous studies, but smaller in magnitude than the predictions of the Gent code. At medium missing energies (40-70 MeV) the rate of change of asymmetry with photon energies was less marked but still compared favorably with other data and theory. Data from higher missing energies also show a distinct asymmetry.

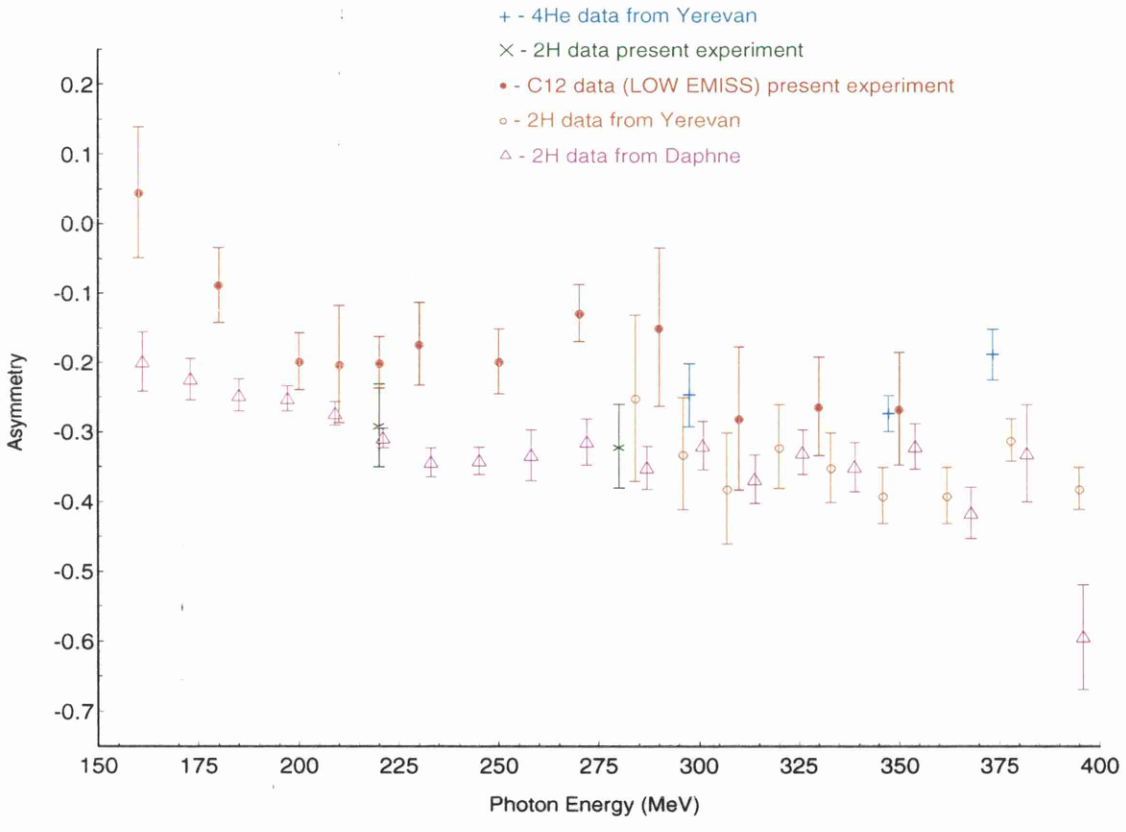


Figure 5.33: *Further Comparison of Low $E_m$ Asymmetry*

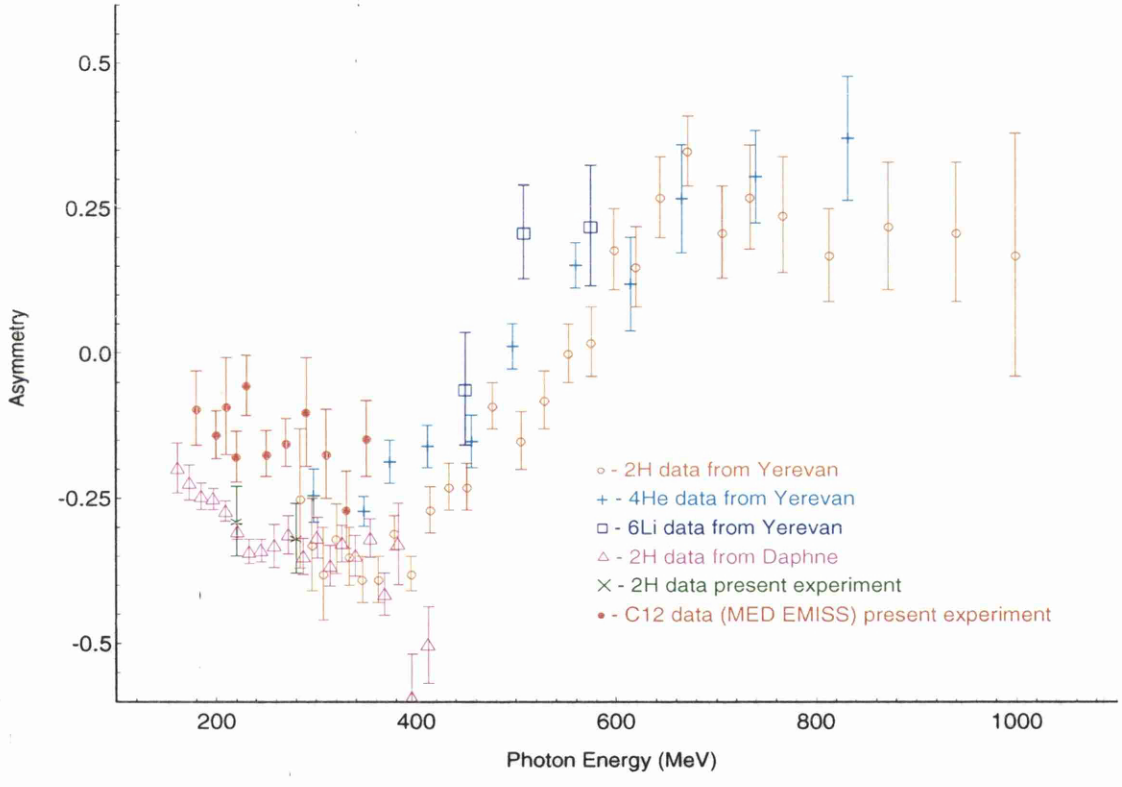


Figure 5.34: *Comparison of Med $E_m$ Asymmetry for 2H and 12C with previous experiments*

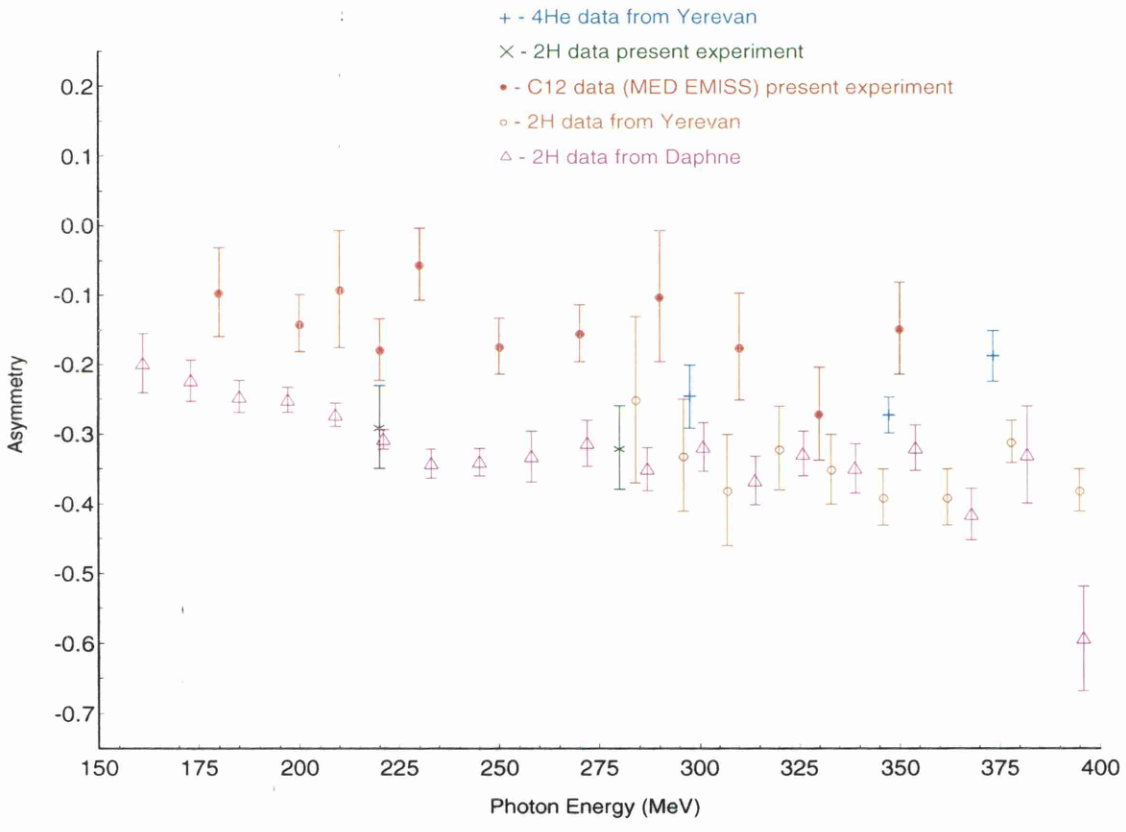


Figure 5.35: *Further Comparison of Med $E_m$ Asymmetry*

Recoil momentum distributions showed the 2N knockout process to be the dominant reaction mechanism, for all but the highest values of recoil momenta. Final state interactions have little or no effect on the shape of these distributions except at these high values of recoil momenta, where hard FSI may be responsible for lower asymmetries. Separate data for the two directions of polarisation show no noticeable difference in shape.

Angular distributions of asymmetries show good agreement with the theoretical predictions above $\sim$200 MeV. Below this photon energy heavy meson exchange, in particular $\rho$-meson exchange may well have a significant influence, but these terms were not included in the present calculations. The calculations also show that the reaction asymmetry is not strongly affected by the distortion of the outgoing particle wave.

Differential cross sections have been presented as angular distributions for the 20-40 MeV missing energy region, These distributions reflect the reaction asymmetries and are comparable to angular distributions measured in previous unpolarised experiments on $^{12}$C [10].

Comparisons have been made with data from previous experiments, and these show a very similar shape to asymmetries in lighter nuclei, but with a reduced magnitude. Data from a range of light nuclei display values of asymmetry which are consistently lower in magnitude than those of deuterium.

# Chapter 6

# Conclusions and Outlook

## 6.1 Conclusions

The work presented in this thesis is the first measurement of the asymmetry of the $^{12}C(\vec{\gamma},pn)$ reaction. The experiment was carried out at the Institut für Kernphysik, in the Johannes-Gutenberg Universität in Mainz, Germany. The experimental apparatus has an overall missing energy resolution of 7.5 MeV. The experiment was conducted at photon energies between 150-360 MeV, and involved measuring the photon asymmetry in 3 different missing energy regions for 12 different photon energy bins. Photon asymmetries were also measured as a function of recoil momentum for the low (20-40 MeV) and medium (40-70 MeV) missing energy regions. At low missing energies, asymmetries were measured as a function of proton polar angle. The data were compared to theoretical predictions.

Systematic checks were made of the photon asymmetry of the Deuteron, and these confirmed the accuracy of the present analysis. The $^{12}C(\vec{\gamma},pn)$ data showed that at low missing energies, the magnitude of the photon asymmetry is negative, and decreases rapidly for photon energies up to 200 MeV. It then stays fairly constant before rising slightly at 270 MeV, and falling again. This behaviour is similar to that seen previously in other light nuclei, [25]. It suggests that the microscopic mechanisms contributing to 2N emission are similar in all other light nuclei, but change with photon energy. At medium missing energies a similar trend is apparent, although the magnitudes are reduced particularly for photon energies below 200 MeV. This would suggest that the contributing mechanisms do not change as dramatically as those at lower missing energies. At higher missing energies measurable asymmetries were observed. The theory developed by the Gent group describes the behaviour as a function of both $E_\gamma$ and $\Theta_p$ in the low missing energy region, both in shape and magnitude, for photon energies above

200 MeV. Below this heavy meson exchange, not included in the theory, may be responsible for the difference between theory and experiment. Very recent theoretical calculations may also suggest that the role of the seagull term is enhanced in this photon energy region, leading to this discrepancy. For medium missing energies the Gent model overestimates the magnitude of the measured asymmetries, which may be due to hard scattering FSI which could reduce the magnitude of the photon asymmetry in this region.

An analysis of the photon asymmetry as a function of recoil momentum showed that for all but the highest values of recoil momenta at the highest photon energies, 2N absorption on a correlated *pn* pair is likely to be the dominant process at low missing energies. In the medium missing energy region the data support the conclusion that 2N absorption is again dominant, except at the highest values of recoil momenta. In this case, deviations are seen in all photon energy regions. The data also showed no significant P dependence on $\Sigma$.

Photon asymmetries for low missing energy regions were measured as a function of proton polar angle, and compared to the predictions of the Gent code. For photon energies above 200 MeV the theory fits the data well, but below 200 MeV the theory begins to overestimate the measured photon asymmetry. This again may suggest that $\rho$-meson exchange or an enhancement of the $\Delta$ term may have an influence.

Comparisons with previous measurements on the deuteron and some other light nuclei show a similarity between quasideuteron and real deuteron photodisintegration. However, although the shapes are similar, the magnitudes are different.

## 6.2 Outlook

In order to extend our understanding and develop this field further, a number of investigations may be carried out. Firstly the photon energy range could be widened. A study could be made at photon energies from as low as 30 MeV, in the giant resonance region, well below the $\Delta$ resonance region, where photons are mainly absorbed by electric dipole transitions. The study could be conducted at photon energies up to the ones examined here, in order to study the behaviour of the photon asymmetry in a region where the contributing microscopic processes appear to be changing. Any further work could also be conducted at photon energies above those examined here. Measuring the photon asymmetry at energies up to 1 GeV would allow a comparison with data previously obtained on lighter nuclei, in which the asymmetry was seen to change sign between 500-600 MeV, [25].

Any future experiment would also benefit from having a larger polar angle coverage. As seen, the asymmetry is predicted to be zero at proton polar angles of $0^o$ and $180^o$, [41]. An experimental measurement would be an interesting test of this prediction.

The theoretical predictions could be improved by the inclusion of $\rho$-meson exchange which may give better predictions of asymmetry at photon energies below 200 MeV. Improvements may also come from an better theoretical understanding of the role of the seagull term in this region. The comparison between experiment and theory would also be improved by including the detector acceptances into the theoretical code. This would allow a direct comparison to be made for out of plane azimuthal angles.

In any further experiment the quality of the data could be enhanced by improving its statistical accuracy. This could be achieved simply by increasing the

amount of data taken, although this is an inefficient method. The detectors could be improved, although this is expensive financially.

In the general field itself, further investigations could also be carried out into similar reaction channels. Indeed, a study is now proceeding of the $^{12}C(\vec{\gamma},pp)$ reaction, [48]. Other possible reaction channels, such as those including pions, and the 3N channels are also likely to provide interesting results, and are being investigated [61].

A further study could also be conducted using other targets. Measurements of photon asymmetry made on a succession of heavier nuclei would show whether the similarities seen in this work, between different nuclei, are repeated for other nuclei.

# Appendix A

# Non-Zero Azimuthal Angles

As discussed in section 4.7, non-zero azimuthal angles affect the value of measured asymmetries. In order to correct for this, the azimuthal angular range accepted by the detectors was restricted, and a correction was made for the finite value of that range. To see how this arises we start from a definition of cross-section:-

$$d\sigma = d\sigma_o(1 + P\Sigma cos2\phi) \tag{A.1}$$

where $\sigma_o$ is the unpolarised cross-section, P is the fractional polarisation and $\phi$ is the azimuthal angle. Now, if $\phi_{||}$ is the azimuthal angle in the parallel plane of polarisation and $\phi_{\perp}$ is the azimuthal angle in the perpendicular plane of polarisation, we assume that they are zero degrees and $\pi/2$ degrees respectively. Also, we assume the value of polarisation in each direction is the same. i.e. $P_{||} = P_{\perp}$. This has been shown in section 4.3.1. Then we get:-

$$d\sigma_{||} = d\sigma_o(1 + P\ \Sigma) \tag{A.2}$$

and

$$d\sigma_{\perp} = d\sigma_o(1 + P\ \Sigma) \tag{A.3}$$

where $\sigma_{||}$ and $\sigma_{\perp}$ are the parallel and perpendicular cross-sections respectively. From equations A.2 and A.3 we therefore deduce that:-

$$\Sigma = \frac{1}{P}\frac{d\sigma_{||} - d\sigma_{\perp}}{d\sigma_{||} + d\sigma_{\perp}} \tag{A.4}$$

where $d\sigma_{||}$ and $d\sigma_{\perp}$ are the parallel and perpendicular cross-sections respectively. Now, if we allow for a finite range in the azimuthal angles for both para and perp cross-sections, i.e. $d\sigma_{||}$ goes from - $\phi_1$ to + $\phi_2$ and $d\sigma_{||}$ goes from $\frac{\pi}{2}$ - $\phi_1$ to $\frac{\pi}{2}$ + $\phi_2$. This gives us an average cross section, $d\bar{\sigma}$, for each direction of polarisation:-

$$d\bar{\sigma}_{||} = \frac{\int_{-\phi_1}^{\phi_2} d\sigma_o(1 + P\,\Sigma cos2\phi)d\phi}{\int_{-\phi_1}^{\phi_2} d\phi} \tag{A.5}$$

on integrating this becomes:-

$$d\bar{\sigma}_{||} = d\sigma_o(1 + P\Sigma\frac{1}{2}\frac{(sin2\phi_2 + sin2\phi_1)}{(\phi_2 + \phi_1)}) \tag{A.6}$$

and similarily

$$d\bar{\sigma}_{\perp} = d\sigma_o(1 - P\Sigma\frac{1}{2}\frac{(sin2\phi_2 + sin2\phi_1)}{(\phi_2 + \phi_1)}) \tag{A.7}$$

this then gives us an expression for the asymmetry:-

$$\Sigma = \frac{2(\phi_1 + \phi_2)}{sin2\phi_1 + sin2\phi_2}\frac{1}{P}\frac{d\sigma_{||} - d\sigma_{\perp}}{d\sigma_{||} + d\sigma_{\perp}} \tag{A.8}$$

This in effect gives us a correction factor, $\frac{2(\phi_1 + \phi_2)}{sin2\phi_1 + sin2\phi_2}$, by which the measured value of $\Sigma$ must be corrected by.

For example, if the full $\phi$ range of PiP, at 46$^o$ was used, this would give us a correction factor of $\sim$5%. For this present work, a $\phi$ range of 29$^o$ was used leading to a correction of $\sim$4%. All the measured asymmetries in this work have been corrected by this factor.

# Appendix B

# Tables of Experimental Results

| *Setup No.* | *Photon Energy Bin* | *Asymmetry* |
|---|---|---|
| 1 | 150-170 MeV | 0.046 ± 0.094 |
| | 170-190 MeV | -0.087 ± 0.054 |
| | 190-210 MeV | -0.197 ± 0.041 |
| | 210-230 MeV | -0.199 ± 0.037 |
| 2 | 200-220 MeV | -0.201 ± 0.084 |
| | 220-240 MeV | -0.172 ± 0.059 |
| | 240-260 MeV | -0.197 ± 0.047 |
| | 260-280 MeV | -0.127 ± 0.041 |
| 3 | 280-300 MeV | -0.148 ± 0.114 |
| | 300-320 MeV | -0.279 ± 0.103 |
| | 320-340 MeV | -0.262 ± 0.072 |
| | 340-360 MeV | -0.265 ± 0.081 |

Table B.1: *Asymmetries for $E_m$ = 20-40 MeV*

| *Setup No.* | *Photon Energy Bin* | *Asymmetry* |
|---|---|---|
| 1 | 150-170 MeV | -0.332 ± 0.126 |
| | 170-190 MeV | -0.095 ± 0.064 |
| | 190-210 MeV | -0.140 ± 0.041 |
| | 210-230 MeV | -0.159 ± 0.036 |
| 2 | 200-220 MeV | -0.153 ± 0.030 |
| | 220-240 MeV | -0.092 ± 0.083 |
| | 240-260 MeV | -0.056 ± 0.051 |
| | 260-280 MeV | -0.173 ± 0.040 |
| 3 | 280-300 MeV | -0.101 ± 0.094 |
| | 300-320 MeV | -0.174 ± 0.076 |
| | 320-340 MeV | -0.269 ± 0.067 |
| | 340-360 MeV | -0.147 ± 0.063 |

Table B.2: *Asymmetries for $E_m$ = 40-70 MeV*

| *Setup No.* | *Photon Energy Bin* | *Asymmetry* |
|---|---|---|
| 1 | 150-170 MeV | -0.049 ± 0.195 |
| | 170-190 MeV | -0.236 ± 0.089 |
| | 190-210 MeV | -0.111 ± 0.046 |
| | 210-230 MeV | -0.108 ± 0.037 |
| 2 | 200-220 MeV | -0.033 ± 0.098 |
| | 220-240 MeV | -0.056 ± 0.059 |
| | 240-260 MeV | -0.097 ± 0.035 |
| | 260-280 MeV | -0.026 ± 0.027 |
| 3 | 280-300 MeV | -0.219 ± 0.074 |
| | 300-320 MeV | -0.197 ± 0.053 |
| | 320-340 MeV | -0.216 ± 0.038 |
| | 340-360 MeV | -0.075 ± 0.034 |

Table B.3: *Asymmetries for $E_m$ = 70+ MeV*

| *Setup No.* | *Photon Energy Bin* | *Asymmetry* |
|---|---|---|
| 1 | 150-170 MeV | -0.109 ± 0.079 |
| | 170-190 MeV | -0.131 ± 0.043 |
| | 190-210 MeV | -0.143 ± 0.028 |
| | 210-230 MeV | -0.148 ± 0.025 |
| 2 | 200-220 MeV | -0.093 ± 0.055 |
| | 220-240 MeV | -0.076 ± 0.035 |
| | 240-260 MeV | -0.136 ± 0.026 |
| | 260-280 MeV | -0.081 ± 0.020 |
| 3 | 280-300 MeV | -0.184 ± 0.055 |
| | 300-320 MeV | -0.201 ± 0.043 |
| | 320-340 MeV | -0.231 ± 0.035 |
| | 340-360 MeV | -0.100 ± 0.029 |

Table B.4: *Asymmetries for ALL* $E_m$

| *Photon Energy Bin* | $\Theta_{prot}^{lab}$ | *Asymmetry* |
|---|---|---|
| 150-170 MeV | 52°-71° | -0.049 ± 0.249 |
| | 72°-91° | 0.242 ± 0.167 |
| | 92°-111° | -0.013 ± 0.146 |
| | 112°-130° | -0.029 ± 0.238 |
| 170-190 MeV | 52°-71° | -0.136 ± 0.118 |
| | 72°-91° | -0.209 ± 0.104 |
| | 92°-111° | -0.009 ± 0.101 |
| | 112°-130° | -0.018 ± 0.121 |
| 190-210 MeV | 52°-71° | -0.264 ± 0.087 |
| | 72°-91° | -0.175 ± 0.069 |
| | 92°-111° | -0.172 ± 0.065 |
| | 112°-130° | -0.201 ± 0.091 |
| 210-230 MeV | 52°-71° | -0.160 ± 0.070 |
| | 72°-91° | -0.192 ± 0.057 |
| | 92°-111° | -0.198 ± 0.065 |
| | 112°-130° | -0.259 ± 0.080 |

Table B.5: *Angular Asymmetries for setup 1*

| *Photon Energy Bin* | $\Theta_{prot}^{lab}$ | *Asymmetry* |
|---|---|---|
| 200-220 MeV | $52^o$-$71^o$ | -0.185 ± 0.165 |
| | $72^o$-$91^o$ | -0.207 ± 0.159 |
| | $92^o$-$111^o$ | -0.093 ± 0.154 |
| | $112^o$-$130^o$ | -0.433 ± 0.216 |
| 220-240 MeV | $52^o$-$71^o$ | -0.048 ± 0.104 |
| | $72^o$-$91^o$ | -0.278 ± 0.108 |
| | $92^o$-$111^o$ | -0.247 ± 0.106 |
| | $112^o$-$130^o$ | 0.124 ± 0.209 |
| 240-260 MeV | $52^o$-$71^o$ | -0.123 ± 0.084 |
| | $72^o$-$91^o$ | -0.228 ± 0.079 |
| | $92^o$-$111^o$ | -0.255 ± 0.086 |
| | $112^o$-$130^o$ | -0.155 ± 0.127 |
| 260-280 MeV | $52^o$-$71^o$ | -0.123 ± 0.080 |
| | $72^o$-$91^o$ | -0.105 ± 0.069 |
| | $92^o$-$111^o$ | -0.181 ± 0.078 |
| | $112^o$-$130^o$ | -0.117 ± 0.137 |

Table B.6: *Angular Asymmetries for setup 2*

| *Photon Energy Bin* | $\Theta_{prot}^{lab}$ | *Asymmetry* |
|---|---|---|
| 280-300 MeV | 52°-71° | -0.171 ± 0.223 |
| | 72°-91° | -0.199 ± 0.200 |
| | 92°-111° | -0.119 ± 0.224 |
| | 112°-130° | 0.0 ± 0.225 |
| 300-320 MeV | 52°-71° | -0.678 ± 0.282 |
| | 72°-91° | -0.257 ± 0.157 |
| | 92°-111° | -0.064 ± 0.161 |
| | 112°-130° | 0.096 ± 0.227 |
| 320-340 MeV | 52°-71° | -0.374 ± 0.140 |
| | 72°-91° | -0.139 ± 0.122 |
| | 92°-111° | -0.236 ± 0.126 |
| | 112°-130° | -0.356 ± 0.190 |
| 340-360 MeV | 52°-71° | -0.131 ± 0.152 |
| | 72°-91° | -0.416 ± 0.143 |
| | 92°-111° | -0.202 ± 0.139 |
| | 112°-130° | -0.369 ± 0.198 |

Table B.7: *Angular Asymmetries for setup 3*

| *Photon Energy Bin* | $\Theta_{prot}^{lab}$ | $d^2\sigma_{\|\|}/d\Omega_n\Omega_p(\mu b/sr^2)$ | $d^2\sigma_{\perp}/d\Omega_n\Omega_p(\mu b/sr^2)$ |
|---|---|---|---|
| 150-170 MeV | 52°-71° | 10.156 ± 1.269 | 9.867 ± 0.879 |
| | 72°-91° | 12.432 ± 0.809 | 14.325 ± 1.058 |
| | 92°-111° | 11.460 ± 0.752 | 11.377 ± 0.734 |
| | 112°-130° | 8.375 ± 0.866 | 8.242 ± 0.867 |
| 170-190 MeV | 52°-71° | 9.418 ± 0.679 | 8.342 ± 0.679 |
| | 72°-91° | 14.394 ± 0.875 | 11.939 ± 0.874 |
| | 92°-111° | 11.079 ± 0.726 | 10.996 ± 0.727 |
| | 112°-130° | 9.398 ± 0.734 | 9.249 ± 0.734 |
| 190-210 MeV | 52°-71° | 14.501 ± 0.870 | 10.734 ± 0.870 |
| | 72°-91° | 17.244 ± 0.974 | 14.118 ± 0.779 |
| | 92°-111° | 15.419 ± 0.729 | 12.684 ± 0.730 |
| | 112°-130° | 12.051 ± 0.871 | 9.590 ± 0.727 |
| 210-230 MeV | 52°-71° | 15.119 ± 0.872 | 12.498 ± 0.775 |
| | 72°-91° | 19.609 ± 0.878 | 15.597 ± 0.779 |
| | 92°-111° | 15.911 ± 0.814 | 12.563 ± 0.723 |
| | 112°-130° | 13.652 ± 1.017 | 10.035 ± 0.463 |

Table B.8: *Angular cross sections for setup 1*

| *Photon Energy Bin* | $\Theta_{prot}^{lab}$ | $d^2\sigma_{\|\|}/d\Omega_n\Omega_p(\mu b/sr^2)$ | $d^2\sigma_{\perp}/d\Omega_n\Omega_p(\mu b/sr^2)$ |
|---|---|---|---|
| 200-220 MeV | 52°-71° | 16.714 ± 0.972 | 14.959 ± 1.158 |
| | 72°-91° | 22.144 ± 1.359 | 19.718 ± 1.359 |
| | 92°-111° | 16.012 ± 0.989 | 15.197 ± 0.989 |
| | 112°-130° | 14.363 ± 1.185 | 11.251 ± 1.036 |
| 220-240 MeV | 52°-71° | 15.937 ± 0.972 | 15.348 ± 0.874 |
| | 72°-91° | 20.980 ± 1.263 | 16.898 ± 0.971 |
| | 92°-111° | 16.013 ± 0.899 | 13.222 ± 0.809 |
| | 112°-130° | 10.124 ± 1.027 | 11.147 ± 1.467 |
| 240-260 MeV | 52°-71° | 14.571 ± 0.874 | 12.927 ± 0.778 |
| | 72°-91° | 20.783 ± 1.068 | 16.602 ± 0.971 |
| | 92°-111° | 16.189 ± 0.899 | 12.591 ± 0.809 |
| | 112°-130° | 10.421 ± 0.881 | 8.953 ± 0.881 |
| 260-280 MeV | 52°-71° | 16.226 ± 0.972 | 14.183 ± 0.971 |
| | 72°-91° | 20.589 ± 1.068 | 18.358 ± 1.068 |
| | 92°-111° | 16.995 ± 0.989 | 13.935 ± 0.899 |
| | 112°-130° | 8.508 ± 0.880 | 7.471 ± 0.879 |

Table B.9: *Angular cross sections for setup 2*

| *Photon Energy Bin* | $\Theta_{prot}^{lab}$ | $d^2\sigma_{\|\|}/d\Omega_n\Omega_p(\mu b/sr^2)$ | $d^2\sigma_{\perp}/d\Omega_n\Omega_p(\mu b/sr^2)$ |
|---|---|---|---|
| 280-300 MeV | $52^o$-$71^o$ | 14.959 ± 1.166 | 13.794 ± 1.107 |
| | $72^o$-$91^o$ | 18.259 ± 1.262 | 16.603 ± 1.165 |
| | $92^o$-$111^o$ | 12.999 ± 0.986 | 12.285 ± 0.986 |
| | $112^o$-$130^o$ | 10.139 ± 1.176 | 10.139 ± 1.176 |
| 300-320 MeV | $52^o$-$71^o$ | 14.183 ± 1.846 | 9.229 ± 0.874 |
| | $72^o$-$91^o$ | 16.997 ± 1.166 | 14.473 ± 1.068 |
| | $92^o$-$111^o$ | 13.629 ± 0.986 | 13.092 ± 0.986 |
| | $112^o$-$130^o$ | 9.561 ± 1.029 | 10.154 ± 1.030 |
| 320-340 MeV | $52^o$-$71^o$ | 13.794 ± 0.971 | 10.296 ± 0.874 |
| | $72^o$-$91^o$ | 16.997 ± 1.166 | 15.242 ± 1.067 |
| | $92^o$-$111^o$ | 13.899 ± 0.986 | 11.562 ± 0.807 |
| | $112^o$-$130^o$ | 10.287 ± 1.029 | 7.797 ± 0.883 |
| 340-360 MeV | $52^o$-$71^o$ | 8.651 ± 0.874 | 7.674 ± 0.777 |
| | $72^o$-$91^o$ | 12.817 ± 1.068 | 8.735 ± 0.874 |
| | $92^o$-$111^o$ | 10.134 ± 0.896 | 8.428 ± 0.807 |
| | $112^o$-$130^o$ | 8.671 ± 1.029 | 6.181 ± 0.883 |

Table B.10: *Angular cross sections for setup 3*

# Bibliography


[1] J. Ahrens, Nucl.Phys. A446 (1985) 229c.

[2] J.S. Levinger, Phys. Rev. 84 (1951) 43.

[3] J.C. McGeorge *et al.*, Physics Rev C51 (1995) 1967.

[4] P. Grabmayr *et al.*, Phys. Lett. B370 (1996) 17.

[5] P.D. Harty *et al.*, Physics Letters B B380 (1996) 247.

[6] J.S. Levinger, Phys. Lett. B82 (1979) 181.

[7] K. Gottfried, Nuc. Phys. 5 (1958) 557.

[8] J. Ryckebusch *et al.*, Phys. Lett. B 291 (1992) 213.

[9] M. Vanderhaeghen, L. Machenil, J. Ryckebusch and M. Waroquier, Nucl. Phys.A580 (1994) 551

[10] T.T-H. Yau, University of Glasgow, PhD Thesis (1996).

[11] M.Q. Barton and J.H. Smith, Phys. Rev. 110 (1958) 1143.

[12] J. Garvey *et al.*, Nucl. Phys. 70 (1965) 241.

[13] I.L. Smith, J. Garvey, J.G. Rutherglen and G.R. Brookes, Nucl. Phys. B1 (1967) 483.

[14] P.C. Stein *et al.*, Phys. Rev. 119 (1960) 348.

[15] S.N. Dancer *et al.*, Phys. Rev. Lett. 61 (1988) 1170.

[16] S.M. Doran *et al.*, Nucl. Phys. A559 (1993) 347.

[17] I.J.D. MacGregor *et al.*, Nucl. Phys. A533 (1991) 269.

[18] H. Herminghaus *et al.*, NIM 138 (1976) 1.

[19] P.D. Harty *et al.*, Phys. Rev. C 47 (1993) 2185.

[20] T. Lamparter *et al.*, Z. Phys. A355 (1996) 1.

[21] G.S. Blanpied *et al.*, Physics Rev. Lett. 67 (1991) 1206.

[22] M.P. de Pascale *et al.*, Phys. Rev. C 32 (1985) 1830.

[23] F.V. Adamian *et al.*, J. Phys. G. 17 (1991) 1189.

[24] D.J. Tedeschi *et al.*, Phys. Rev. Lett. 73 (1994) 408.

[25] F.V. Adamian *et al.*, J. Phys. G. 17 (1991) 1657.

[26] P. Wilhelm and H. Arenhöven, Phys. Lett. B 318 (1993) 410.

[27] C. Giusti *et al.*, Nuc. Phys. A546 (1992) 607.

[28] D. Lohmann *et al.*, NIM A343 (1994) 494.

[29] E.J. Williams, Phys. Rev. 45 (1934) 729.

[30] B. Feretti, Nouvo Cimento 7 (1950) 118.

[31] F.H. Dyson and H. Überall, Phys. Rev. 99 (1955) 604.

[32] H. Überall, Phys. Rev. 107 (1957) 223.

[33] H. Überall, Z. Naturforsch. 17a (1962) 332.

[34] G. Bologna *et al.*, Phys. Rev. Lett. 4 (1969) 134.

[35] R.F. Mozley and J. deWire, Nouvo Cimento 27 (1963) 1281.

[36] S. Kato *et al.*, J. Phys. Soc. Jap. 20 (1965) 303.

[37] G. Bologna *et al.*, Nouvo Cimento 42 (1966) 844.

[38] U. Timm, Fortschr. Phys. 17 (1969) 765.

[39] F. Rambo, Diploma Thesis, Physikalisches Institut, Georg-August Universität, Göttingen. (1995).

[40] S. Boffi *et al.*, Nuc. Phys. A564 (1993) 473.

[41] J. Ryckebusch, Max-Lab Workshop Report SSF97-04-01.

[42] I. Anthony *et al.*, NIM A301 (1991) 230.

[43] S.J. Hall, G.J. Miller, R. Beck and P. Jennewein, NIM A368 (1996) 698.

[44] G.E. Cross, University of Glasgow, PhD Thesis (1994).

[45] P. Grabmayr *et al.*, Proc. Workshop on Future Detectors for Photonuclear-Experiments,May 1991, Ed. D.Branford, P.225

[46] I.J.D. MacGregor *et al.*, NIM A382 (1996) 479.

[47] J.R.M. Annand and B. Oussena, NIM A330 (1993) 220.

[48] C.J.Y. Powrie, University of Glasgow, PhD Thesis (to be submitted).

[49] W. Braunschweig *et al.*, NIM 134 (1976) 261.

[50] T. Hehl *et al.*, NIM A354 (1995) 505.

[51] T. Hehl, private communication.

[52] T. Hehl, PiP/TOF collaboration Internal report 6/96.

[53] R.A. Cecil *et al.*, NIM 161 (1979) 439.

[54] T. Lamparter, PiP/TOF collaboration Internal report 4/94.

[55] C.J.Y. Powrie, private communication.

[56] D.P. Watts, University of Glasgow, PhD Thesis, 1997.

[57] S. Wunderlich & F.A. Natter, PiP/TOF collaboration Internal report 1/97.

[58] P.D. Harty *et al.*, Phys. Rev. C. Submitted for publication.

[59] P.D. Harty, private communication.

[60] S. Wartenberg *et al.*, to be published.

[61] J. Arneil, University of Edinburgh, PhD Thesis (to be submitted).